Ludwig-Maximilians-Universität

Sigillum Universitatis Ludovici Maximiliani

CRASHα: coupling continuum and line radiative transfer

Dissertation der Fakultät für Physik

Dissertation of the Faculty of Physics

der Ludwig-Maximilians-Universität München

at the Ludwig Maximilian University of Munich

für den Grad des

for the degree of

Doctor rerum naturalium

vorgelegt von Marco Pierleoni

presented by

Sigillum Universitatis Ludovici Maximiliani

Prof. Dr. Simon D. M. White

(1^{st} REFEREE)

Prof. Dr. Hans Böhringer

(2^{nd} REFEREE)

Prof. Dr. Jochen Weller

(HEAD OF THE COMMITTEE)

Date of the oral exam: 17 September 2010

Contents

Die Beobachtung von nahen und entfernten Objekten erzeugten Lyα Linien ist schon seit jeher von grösser astrophysikalischer Bedeutung. Diese Beobachtungen werden als Nachweiss für die Rotverschiebung, als ein Ma "ss für die Sternentstehungsrate in Galaxien und als Mittel um den inneren Aufbau von Galaxien zu erkunden verwendet. In den letzten Jahren wurde vermehrt ein Schwerpunkt auf die Suche von Lyα Strahlungsquellen (Lyα emitters, LAEs) bei hohen Rotverschiebungen gesetzt, welche sich durch eine hohe Lyα Emission auszeichnen die jedoch durch Staubabsorption verdeckt wird. Eine Emission von Lyα Photonen bei hohen Rotverschiebungen hat auch einen Einfluss auf die Beobachtbarkeit der 21 cm Linie des neutralen Wasserstoffs im Intergalakatischenmedium.

Die vorliegende Arbeit hat als Ziel ein neuartigen Strahlungstransportverfahren (CRASHα) zu entwickeln, mit welchem man in selbstkonsistener Weise die gleichzeitige Propagation von Lyα und ionisierender Strahlung verfolgen kann. Mit diesem Verfahren ist man in der Lage die Auswirkung von Konfigurationen mit sich verändernder Ionisierung auf die Propagation von Lyα Strahlung und die Veränderung der Linien die von einem einzelnen Objekt emitiert werden zu untersuchen. Die Implementierung dieses neuen Verfahrens berücksichtigt die zeitliche Entwicklung der Lyα Photonen (was üblicherweise in Linien-Strahlungstransportcodes vernachlässigt wird) und verwendet unter Rückgriff auf vor-kompilierte Tabellen einen statistischen Ansatz für die Behandlung der Lyα Strahlung, welcher den Rechenzeitaufwand reduziert, da nicht jede einzelne Streuung der Photonen verfolgt werden muss. Mit dieser Arbeit konnte ich zeigen, dass die resultierenden Spektren eine Erinnerung an die verschiedenen Ionistationszustände haben, und damit dieser Effekt vernüftig Rechnung getragen werden konnte war eine selbstkonsistente Implementierung zur gemeinsamen Behandlung von Linien Strahlung und ionisierender Strahlung in CRASHα notwendig. In einem weiteren Schritt habe ich ein weitere physikalische Pprozesse in CRASHα eingebaut: ein neues Emissionssystem, diffuse Lyα Rekombinations-Photonen und eine Beschreibbung von Staub. Mit einer Simulation einer Galaxie bei einer Rotverschiebung von $z \sim 10$ zeige ich, dass der neue Code in der Lage ist die Veränderungen des Lyα Strahlungsfeldes bei gleichzeitiger Beeinflussung des Hintergrundgases durch ionisierende Strahlung zu verfolgen. In einem weiteren Schritt untersuche ich den Einfluss der Lyα Photonenstreuung auf die Temperatur des Intergalaktischenmediums und ob Lyα Photonen zu einer Erhöhung zu Werten über der Temperatur der Kosmischenhintergrundsstrahlung führen und zu einer sichtbaren Emission der 21 cm Linie führen. Im letzten Kapitel dieser Arbeit, diskutiere ich die Implementeirung des Lyα Heizens in CRASHα und ich untersuche wie sich durch Veränderung der physikalischen Parameter in der Simulation die Temperatur ändert.

Abstract

The detection of Lyα lines from local and distant objects has always been of great importance in astrophysics. It has been extensively used as indicator of redshift, as a measurement of the star formation activity of galaxies and as a probe of their internal structure. In the last few years an increasing interest has been devoted to the search of Lyα emitters (LAEs) at high redshift, which are expected to be characterized by a strong Lyα emission, but significantly attenuated by dust absorption. Emission of Lyα photons from high redshift sources has also an impact on the detectability of 21 cm line from neutral hydrogen in the Intergalactic Medium (IGM).

This work is focused on the study, analysis and implementation of a new radiative transfer scheme (CRASHα) which, for the first time in the literature, follows simultaneously the propagation of Lyα and ionizing radiation self-consistently. This allows to investigate the effects of evolving ionization configurations on the propagation of Lyα radiation and on the shaping of the line emerging from single objects. The implementation introduces the time evolution for Lyα photons (a feature commonly neglected in line radiative transfer codes) and, to reduce the computational time needed to follow each scattering, adopts a statistical approach to the Lyα treatment by making extensive use of pre-compiled tables. I find that the emerging spectra keep memory of the ionization history which generates a given ionization configuration of the gas and, to properly account for this effect, a self-consistent joint evolution of line and ionizing continuum radiation as implemented in CRASHα is necessary.

As next step, I implemented new features in CRASHα : a new emission system, diffuse Lyα photons from recombination and treatment of dust. With a new test performed on a simulated galaxy at redshift $z \sim 10$, I show the ability of the code to determine the variations of the Lyα radiation field while the gas in which it propagates is affected by the ionizing radiation emitted by the stars within the galaxy. In this test, the Lyα radiation is generated by both stars and recombining ionized gas.

Finally I tackle the impact of Lyα photon scattering on the IGM temperature. This is an important issue since Lyα photons could be able to heat the IGM temperature above the CMB temperature and render the 21 cm line visible in emission. In the last Chapter, I discuss the implementation of the Lyα heating in CRASHα and I analyze how the temperature is modified by changing the most relevant physical parameters in the simulation.

Chapter 1

Introduction

In the last years an increasing interest has been devoted in the use of the Lyα line in astrophysical and cosmological contest.
Lyα belongs to the Lyman series which is the series of transitions created when an electron falls from any higher energy level, back to the ground state of the H atom. In particular the Lyα line is emitted when an electron falls from the $n = 2$ orbital to the $n = 1$ orbital, where n is the principal quantum number. The energy levels are given by $E_n = -13.6\ eV/n^2$ and the energy difference between the lowest i (n=1) and second lowest (n=2) levels corresponds to a photon with wavelength 1215.67 $\mathring{A}$, see Fig.1.1.

In the universe there are a multitude of objects emitting the Lyα , since once the H atom is ionized a Lyα photon is likely to be emitted from its recombination. The sources

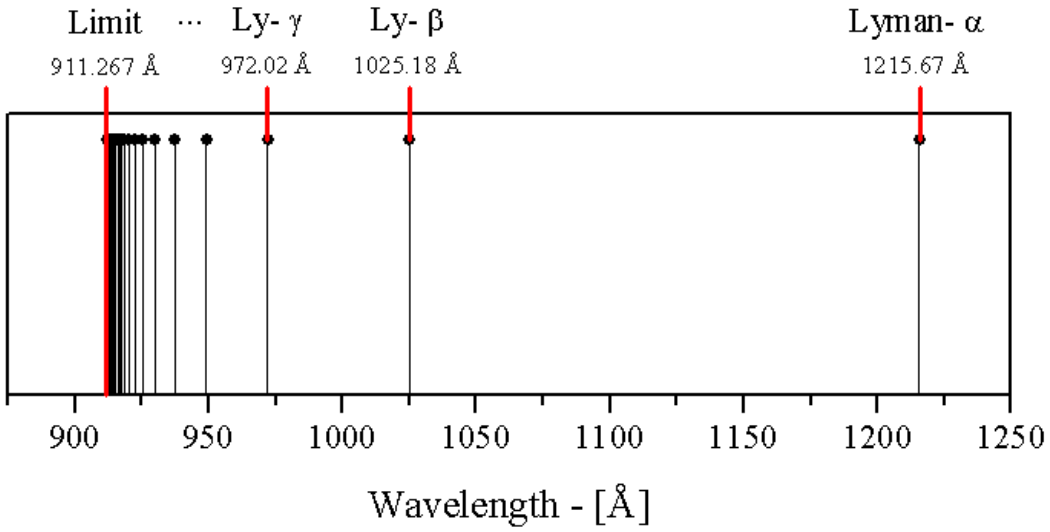

Figure 1.1: Illustration of the Lyman series of hydrogen emission lines

that emit ionizing radiation are very common, they could be very massive stars, QSO or AGN. The first are young, massive and short-lived stars of type O and B very luminous and they emit most of their luminosity in the UV range of the spectrum. Furthermore part of the their ionizing luminosity turns into Lyα through the gas recombination. Hence the star forming galaxy are often intense source of Lyα .

Lyα radiation could also be produced by quasars and active galactic nuclei (AGN, Schmidt 1965; McCarthy 1993; Villar-Martín et al. 2005), which are believed to be massive black holes accreting material from accretion disks. The simplest explanation for the Lyα -emitting gas seen around these systems is that it is due to ionization of the gas in nearby, possibly interacting, galaxies or gas clouds by the quasar (Hu & Cowie 1987, Hu et al. 1991). Even very small column densities of gas or dust (e.g., as little as $10^{18} cm^{-2}$ in neutral hydrogen) can result in significant scattering or reprocessing. They could have a consistent emission in UV and X rays providing an ionization of the surrounding hydrogen, which will emit Lyα from recombination.

1.1 Lyman alpha objects

Star formation in galaxies typically occurs either quiescently at low, sustainable rates or in rapid, unsustainable, and therefore short-lived bursts ('starbursts'). In the second mode, Lyα may be expected to be so bright that it could be seen from the farthest reaches of the observable universe. Indeed this does seem to be the case although, considering the distances involved, even Lyα may appear very faint. Stellar continua are fainter still, often undetected, and Lyα may be the only radiation seen from some galaxies at the highest redshifts, at least with current technology.

The detection of Lyα lines has been extensively used as indicator of redshift, as a measurement of the star formation activity of galaxies and as probe of their internal structure. Many galaxies have been found by means of their strong Lyα emission (Huege et al. 2004), the so-called "LAEs" (Lyman Alpha Emitters). Alternatively, many galaxies were detected on the basis of their UV colours, the so-called "LBG" (Lyα -break galaxies), which are selected using continuum breaks between 912 and 1216 Å(see Sec. 1.1).

Information about the formation and nature of the Lyα emission in high redshift galaxies can be derived from the analysis of the UV-restframe continuum. Using average

spectra of UV-continuum selected high redshift galaxies, Shapley et al. (2003) show that the strength of the Lyα emission is well correlated with other galaxy properties, such as the slope of continuum or the strength of interstellar absorption lines. These correlations may be explained by varying amounts of dust and by the kinematics of the host galaxies. Another method for deriving informations about the nature of the Lyα emission is to analyse the Lyα profile. The profile of the Lyα emission can be used to derive properties of the emitting galaxy (see e.g. Dawson et al. 2002). The detailed comparison of Lyα profiles with dedicated radiative transfer models can constrain the kinematics of the emitting and neutral interstellar medium (ISM). In the following I describe in more details the astrophysical objects which are studied using the Lyα .

Lyman Break Galaxies

An abrupt drop at wavelengths shorter than 912 Å is present if a continuous spectrum is located behind a cloud of neutral hydrogen, since photons with these wavelengths are absorbed during gas ionization. This drop is used in a selection method based on photometric redshifts obtained from observations of the "Lyman Break" in galaxies. As the galaxy radiation is absorbed by the neutral gas, an intensity drop is clearly visible in and in the spectrum. The LBG selection method was pioneered by Steidel et al. (1996; 1999; 2000; 2003), but has also been used by many other groups (e.g. Madau et al. 1996; Pettini et al. 2001; Bunker et al. 2004; Stanway et al. 2004; Ouchi et al. 2004a,b; Wadadekar et al. 2006). An illustration of the method is found in Fig. 1.2. As can be seen, a galaxy will appear to "drop out" in the bluest filter, hence the method is sometimes also referred to as the drop-out technique. Spectroscopic follow-up is necessary to confirm the high redshift nature of the galaxy. The Lyman Break technique can be applied in a wide range of redshifts, when different filters are used for the selection. The technique is typically spectroscopically complete to an R band magnitude of $R \sim 25.5$ for U-band drop-outs but the rate of confirmation falls for higher redshift LBG candidates (Giavalisco 2002).

The spectroscopic confirmation of a large population of UV-selected star-forming galaxies at $z \sim 3$ represented an important step forward in the study of galaxy formation (Steidel et al. 1996b). Essential early observations of color-selected LBGs included the determinations of their redshifts, large-scale clustering, rest-frame UV colors and

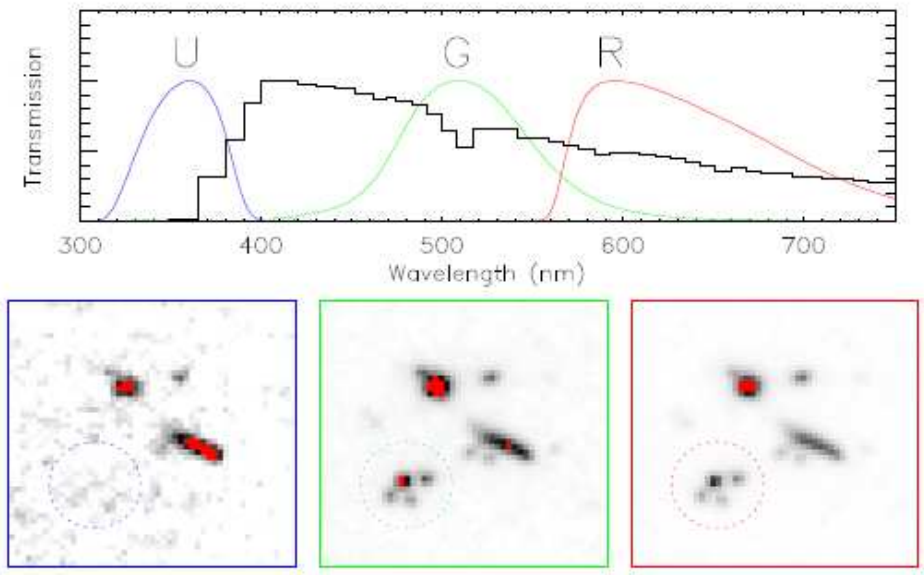

Figure 1.2: Illustration of the LBG selection method. The top panel shows the typical shape of a galaxy spectrum, redshifted to $z \sim 3$. The Lyman Break can be seen at approximately 400 nm. The bottom panels show how such a galaxy would be seen as observed through the three broad-band filters U, G and R that are located on the blue and the red side of the break respectively. The galaxy will not be observed in the filter blueward of the break, but is clearly seen in the red filters. Image credit: Johan Fynbo.

luminosities, and contribution to the universal star-formation rate density at $z = 3$. These discoveries characterized the overall properties of the LBG sample, providing valuable information about their bias with respect to the underlying matter distribution, model-dependent dark-matter halo masses, and their input into the global energy budget at high redshift.

A few studies of the properties of LBGs, such as masses, dust content, ages, have been made so far. These studies are well summarised in Giavalisco (2002). LBGs appear to have ages ranging from a few to several hundred Myrs or even up to 1 Gyr. Stellar masses lie in the range $10^9 < \mathrm{M}_\star/\mathrm{M}_\odot < 10^{11}$. Papovich, Dickinson & Ferguson (2001) find very high extinction in their sample of LBGs, with $A_V \approx 1 - 2$, while Shapley et al. (2001) and Verma et al. (2007) find more modest values of $A_V \approx 0.3 - 0.5$ in their samples. Thus, it appears that LBGs are medium mass and medium dusty galaxies, with high star formation rates of several hundred solar masses per year (Shapley et al. 2001). Several groups have also detected clustering in LBGs, similar to that of Lyα emitters (Steidel et al. 1998; Giavalisco et al. 1998; Ouchi et al. 2004b; see also Sec. 1.1).

Damped Lyα Absorption

Damped Lyα Absorbers (DLAs) are high hydrogen column density gaseous systems ($N(HI) > 2 \times 10^{20} cm^{-2}$)) detected through their absorption lines in the optical spectra of quasars (QSO-DLAs), up to relatively high redshift ($z \sim 5$). This definition is artificial since damped wings appear for lower column densities. It has been introduced assuming that these lines should be characteristic of galactic disks at high redshift (Wolfe et al. 1986).
These gaseous systems have now been studied for more than two decades and are considered to be the progenitors of the present-day galaxies. Studying their physical properties it is possible to assess the chemical abundances of some elements in young galactic systems. They are also useful to trace the bulk of the observed neutral gas in the universe, and therefore, have been used as powerful probes of galaxy formation and evolution back to the redshift of the most distant quasars (Hou et al. 2001). The goal now is to extend the analysis to more and diverse systems. A compilation of several elemental abundances in more types of DLAs is made from the most recent literature. Sub-DLAs and GRB-DLAs enlarge the sample. Sub-DLAs are absorption line systems with HI column density between 10^{19} and $2 \times 10^{20} cm^{-2}$ (Peŕoux et al. 2003). GRB-DLAs are the Damped Lyman alpha absorption systems towards long duration Gamma-Ray Burst afterglows which are associated with the death of metal poor massive stars and mergers of compact objects. Those systems normally have much higher HI column density.
By assessing observed relations regarding their elemental column densities or abundances, one expects to sort out a general understanding of the physical properties in galaxies.

The DLA technique is based on finding high column density galaxies by searching for absorption lines in the spectra of quasars. The identification of DLAs in quasar spectra allows the study of the galaxies and their environments, the gas metallicities, kinematics, temperatures and ionization condition. The use of SPH codes has been extended to study Damped Lyα systems (Katz et al. 1996). Damped Lyα systems serve as important neutral gas reservoirs for star formation at high redshifts (e.g. Nagamine, Springel, & Hernquist 2004). Moreover, as repositories of significant amounts of metals the **Damped Lyα systems** have been used to trace the age-metallicity relationship and other aspects of galactic chemical evolution (Pettini et al. 1994; Pei, Fall, & Hauser

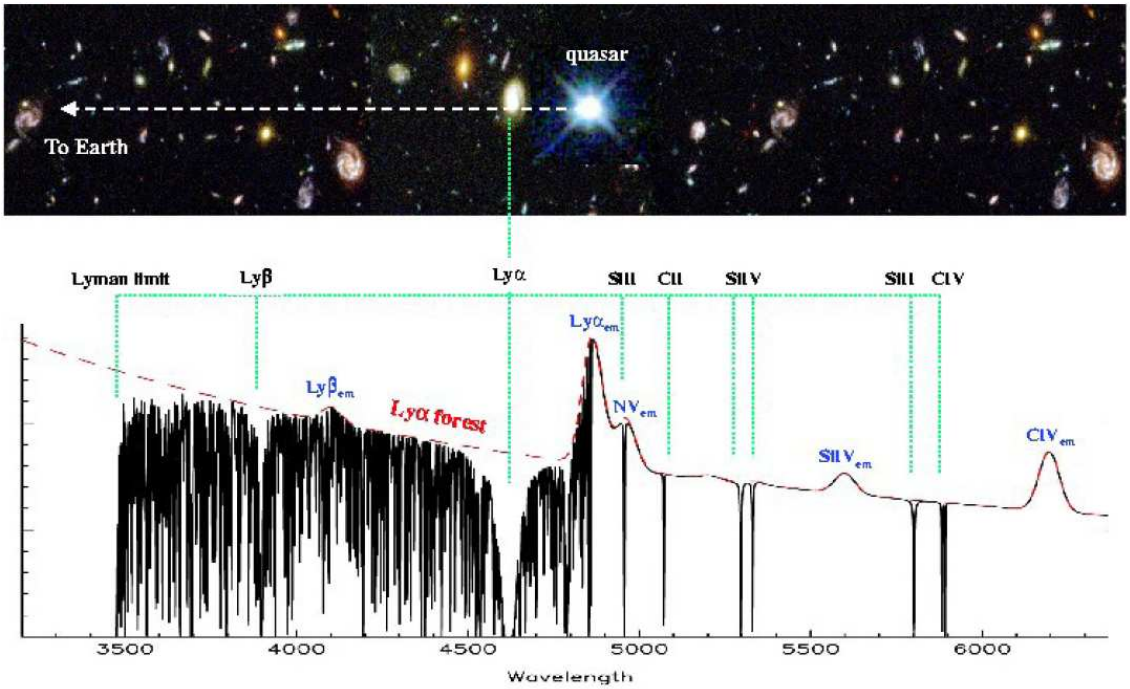

Figure 1.3: quasar spectrum whose sight line intercepted a Damped Lyman Alpha system.

1999; Pettini 2004; Prochaska et al. 2003). Damped Lyα systems provide an important window on the interplay between neutral gas and newly formed stars, i.e., the Damped Lyα systems are the best, perhaps the only, examples we have of an interstellar medium in the high-redshift Universe. Most of the neutral gas in the Universe in the redshift interval z=[0,5] is in Damped Lyα systems. The cosmology and mean intensity of extragalactic Damped Lyα systems radiation are sufficiently well known to justify the assumption of gas neutrality for $N(HI) > 2 \times 10^{20} cm^{-2}$. The close agreement between the mass per unit comoving volume of neutral gas in Damped Lyα systems and visible matter in current galaxies indicates that Damped Lyα systems comprise a significant neutral-gas reservoir for star formation at high redshift. Damped Lyα systems are metal-poor at all redshifts, but exhibit a metallicity 'floor', indicating a different enrichment history than that of the Lyα forest. Damped Lyα systems exhibit evidence for depletion by dust and that the dust content is far lower than in the Galaxy. They are not transient objects but instead probably have ages comparable to the Hubble time at the absorption epoch.

Observations of Damped Lyα systems provide an amazingly rich data set that gives information about galaxy formation unavailable by other means. Specifically, observations of Damped Lyα systems are the only way to study in detail the neutral gas that gave rise

to galaxies at high redshifts.

Lyα emitters

In the last few years an increasing interest has been devoted to the search of Lyα emitters (LAEs) at high redshift, which are expected to be characterized by a strong Lyα emission, but significantly attenuated by dust absorption.
Partridge & Peebles (1967) proposed the use of both the Lyman continuum break and Lya emission line as observational signatures of primeval galaxies and to make observational predictions. These predictions were based upon the most basic stellar population model: that the spectrum of the primeval starburst could be approximated by that of a single blackbody with effective temperature midway between that of an average O and B star ($T_{eff} = 30000K$). Computing the fraction of ionizing photons ($h\nu > 13.6eV$), and assuming that they were all absorbed by neutral hydrogen, Partridge & Peebles were able to estimate the strength of the nebular hydrogen spectrum from recombination theory. For the estimated galaxy masses, the expected Lyα equivalent width, $W_{Ly\alpha}$, corresponded to Lyα fluxes so great that objects could potentially be observed at cosmological distances. This represented the birth of cosmological Lyα studies, at least conceptually. A more advanced approach was adopted by Meier (1976) who modified the single blackbody spectrum of Partridge & Peebles (1967) using more developed population synthesis models (Tinsley 1972). Until the late 1990s, only a few Lyα emitters had been found (Djorgovski & Thompson 1992). This lack of Lyα emission detection triggered a variety of studies discussing the possible physical effects (mostly metallicity, dust, neutral gas kinematics and geometry) which may significantly affect and suppress the Lyα emission and the resonance line radiation transfer, thereby reducing the observed Lyα intensity and destroying simple expected correlations, e.g. between Lyα intensity and metallicity, Lyα intensity and UV continuum flux and others (Meier & Terlevich 1981, Hartmann et al. 1988, Neufeld 1990, Charlot & Fall 1993, Valls-Gabaud 1993, Kunth et al. 1998, Tenorio-Tagle et al. 1999, Mas-Hesse et al. 2003).

It has been necessary to wait for dedicated large programs of deep narrow band searches like the Large Area Lyman Alpha (LALA) and the Subaru Deep Field survey to detect a significant number of emission galaxies at high redshift (e.g. Stern et al. 2005; Iye et al. 2006) and to get complete spectroscopic samples of LAEs at redshift $z = 4.5$, $z = 5.7$

and $z = 6.5$ (e.g. Hu et al. 1998, 2004; Rhoads & Malhotra 2001; Kodaira et al. 2003; Taniguchi et al. 2005; Kashikawa et al. 2006; Murayama et al. 2007; Dawson et al. 2007). Strong lensing magnification has been necessary to move the detection frontiers even further, with several candidates currently observed up to $z \simeq 10$ (e.g. Pelló et al. 2007; Stark et al. 2007). The intense activity reported above is explained by the great interest in using LAEs as cosmological probes: LAEs are in fact the objects with the highest known z and can be used to study large scale structures and galaxy formation in the high redshift universe. Number counts, together with the statistics of line shapes, are extremely powerful observables from which inferring important information about e.g. the properties of the intergalactic medium (IGM) and the reionization era (e.g. Hu 2002; Rhoads 2003; Stern 2005), the photoionization processes and UV photon production (e.g. Stark 2007), the tomography of neutral gas, gas velocity field and star formation activity (e.g. Kodaira et al. 2003). This predicting power relies on the fact that the Lyα line is shaped inside the galaxy interstellar medium and at high redshift is also affected by the IGM opacity, which becomes non negligible to Lyα photons at $z \gtrsim 6$ (Fan et al. 2006).

Emission of Lyα photons from high redshift sources has also an impact on the detectability of 21 cm line from neutral hydrogen in the IGM. At high redshift, the Wouthuysen-Field effect (Wouthuysen 1952; Field 1958, 1959) is in fact extremely efficient in decoupling the spin temperature of the gas, T_s, from the cosmic microwave background (CMB) temperature, $T_{\rm CMB}$, allowing the 21 cm signal to be visible either in absorption or in emission. Fluctuations in the Lyα flux, due both to inhomogeneous distribution of the Lyα radiation sources and to the scattering in the wings, can modify the expected signal (e.g. Barkana & Loeb 2005; Chen & Miralda-Escudé 2006; Chuzhoy & Zheng 2007; Semelin, Combes & Baek 2007), at least as long as a strong Lyα background is not established and the radiation intensity reaches a saturation level (e.g. Ciardi & Madau 2003; Ciardi & Salvaterra 2007).

There are several common features, in a lot of recent papers, which constrain the nature of LAEs. They are young objects, with age of $\sim 10^7$ years, (Pirzkal et al. 2007; Finkelstein et al. 2008; Venemans et al. 2005) and they are not very massive, with a stellar mass between $10^7 M_\odot$ and $10^9 M_\odot$ (Pirzkal et al. 2007; Finkelstein et al. 2008; Gawiser 2006; Gawiser et al. 2008; Venemans et al. 2008; Reddy et al. 2008; Lai et al. 2008). The star formation rates is $\sim 10 M_\odot/yr$ as shown in Gronwall et al. (2007)

and Ouchi et al. (2008). They are believed to have a modest amount of dust in their environments and to reside in haloes with mass of $\sim 10^{11} M_{\odot}$ (Kovac et al. 2007; Gawiser et al. 2007; Ouchi et al. 2007). The luminosity function (LF) of the LAE is still an open question in cosmology. The redshift evolution in the LF is very little if compared to LBGs (Dawson et al. 2007, Ouchi et al. 2008, Bouwens et al. 2007).

Populations of Lyα-selected galaxies at $z \sim 3.1$ have been studied by both Gawiser et al. (2006) and Nilsson et al. (2007) by stacking optical and NIR data-points for 40 objects, and optical, NIR and Spitzer data-points for 23 objects, respectively. Results of these two studies are largely in agreement, with best fit ages of 500 Myr, and stellar masses of $5 \times 10^8 M_{\odot}$. Finkelstein et al. (2007) have applied SED fitting methods to objects found in the z=4.5 LALA field, stacking 21 objects for which continuum detections were made in subgroups based upon $W_{Ly\alpha}$. They found that both age and mass increased with decreasing $W_{Ly\alpha}$, with ages ranging between 4 and 200 Myr and masses between 2×10^7 and $2 \times 10^9 M_{\odot}$. This result is entirely consistent with the current understanding since $W_{Ly\alpha}$ is a rapidly decreasing function of stellar age, and older stars reduce $W_{Ly\alpha}$ while increasing the mass. Pirzkal et al. (2006) combine Spitzer mid-IR data-points with HUDF data from a sample of nine LAEs between $z = 4$ and 5.5, fitting models to individual sources. The addition of restframe R-band data-points proves crucial in the stellar mass estimates, which they conclude to be lower than previous studies, in the range $10^6 - 10^8 M_{\odot}$. All ages were determined to be less than 20 Myr at best fit. Similarly, Lai et al. (2007) have presented SED-fitting studies of three LAEs at z 5.7, also combining HST/ACS with Spitzer datapoints. These authors find significantly higher masses ($10^9 - 10^{10} M_{\odot}$) and ages in the range from 5 to 100 Myr for instantaneous burst models, with ages pushed as high as 700 Myr when continuous star formation is allowed. It should be noted that some of these ages are significantly greater than the limits at which an emission line spectrum could be expected. Clearly very young stellar populations must be present in these objects. Details of the star formation history are very hard to constrain and what is really being determined is a luminosity-weighted average age. The effect of dust at high-z has also been examined by some of these authors with signs of modest extinction being the norm, rather than the exception, despite the sensitivity of the Lyα line to the presence of dust. Typical V-band extinction (AV_v) has been found to be 0.1 (Gawiser et al. 2006), 0.26 (Nilsson et al. 2007). Curiously, the highest-redshift

object studied in this way is a z=6.96 lensed object of Hu et al. (2002), which shows AV_v higher than those quoted above, with a value between 0.5 and 1.8 at the 1s level (Schaerer & Pello' 2005; Chary et al. 2005). The examples outlined above give the best insights available into the properties of the LAEs, but are difficult to understand in a coherent manner. Differing redshifts have been targeted and differences in halo-mass and other evolutionary effects may well enter. The relative selection functions, depths of the observations, and stacking may introduce further biases. Equally detrimental is the approach to SED fitting with many parameters, often with degenerate effects, being fit to few data-points that may be contaminated with previous generations of stars and strong emission lines. If population III objects (metal-free or very metal poor) were to enter the samples, then a revision of the methodology would be required: models would be largely inequipped, with stellar libraries not suited to the very massive stars, nebular gas continuum may be greatly enhanced, emission lines may dominate certain bandpasses, and the Initial Mass Function (IMF) is so uncertain it would most likely need to be a free parameter.

Chapter 2

CRASHα

Due to the resonant nature of the Lyα line propagation, a self-consistent and detailed treatment of the line radiation transfer is required in order to model properly how Lyα radiation affects the IGM, as well as to understand how different physical processes shape the spectral features of LAEs. As a consequence of the great interest in this field, several semi-analytic and numerical studies of the Lyα radiative transfer have followed the first pioneering papers on the subject (Osterbrock 1962; Avery & House 1968; Adams 1972; Harrington 1973; Neufeld 1990). Analytic solutions have been derived only for few simple geometrical gas configurations: static plane parallel slabs including dust (Neufeld 1990), static uniform sphere (Dijkstra, Haiman & Spaans 2006) and uniform gas with pure Hubble flow around a steady Lyα source (Loeb & Rybicki 1999). Given the difficulties in the treatment of radiative transfer though, also the numerical approaches developed so far, mostly based on Monte Carlo techniques, have been in most cases specifically designed for particular physical configurations and problems: 1D dusty and optically thick media (Ahn, Lee & Lee 2000, 2001); 3D arbitrary distribution of dustless gas with arbitrary bulk velocity field (Zheng & Miralda-Escudé 2002); spherically symmetric collapsing gas clouds (Dijkstra, Haiman & Spaans 2006); Lyα scattering off opaque, dusty and moving clouds (Hansen & Oh 2006); Hubble like expansion flows of neutral gas (Loeb & Rybichi 1999; Kobayashi & Kamara 2004). Other codes have been specifically designed for studying LAEs and Lyα pumping in a cosmological context (Gould & Weinberg 1996; Cantalupo et al. 2005; Tasitsiomi 2006; Semelin, Combes & Baek 2007). Verhamme, Schaerer & Maselli (2006, VSM06) have developed a general-purpose 3D Lyα radiation transfer code applicable to dusty media with arbitrary geometries and velocity fields.

So far analytical, semi-analytical as well as numerical studies perform the Lyα radiative

transfer as a post-process calculation by assuming a fixed ionization structure of the gas through which it propagates, while none of them has tackled the Lyα radiative transfer problem by taking into account the effect of an evolving ionization configuration. Nevertheless, as I show in the following of this thesis, this approximation results to be a poor one for some applications of interest, in particular for cosmological studies at high redshift, but also when modeling the Lyα emission from young galaxies.

In this thesis I present CRASHα , a new radiative transfer scheme which, for the first time in the literature, follows simultaneously the propagation of Lyα and ionizing radiation self-consistently. This allows to investigate the effects of evolving ionization configurations on the propagation of Lyα radiation and on the shaping of the line emerging from single objects. The impact of an evolving ionization structure can in fact be significant and needs to be taken into account: the large cross-section of Lyα photons makes propagation dominated by resonant scattering with HI atoms and the random-walk-like nature of the process makes the characteristic time for Lyα photon propagation much larger than the one for ionizing radiation. If an ionizing continuum changes the ionization of the gas through which the Lyα photon is propagating, the amount of scattering suffered by the line photons before escaping will depend on the ionization history of the system. In this case, a joint treatment of both line and continuum transfer is needed to study the alterations in the Lyα spectrum occurring during the evolutionary stages of the ionized regions.

The code presented in this thesis is the first step in this direction. CRASHα has been implemented as an extension of the 3D ray-tracing radiative transfer code for ionizing radiation CRASH (Ciardi et al. 2001; Maselli, Ferrara & Ciardi 2003; Maselli & Ferrara 2005; Maselli, Ciardi & Kanekar 2009), by developing a new independent algorithm which follows the path of line photons in time and space. As described in details in the following, this new algorithm makes extensive use of pre-compiled tables which have been derived by using the line transfer code MCLyα (VSM06) and allows to compute in an extremely efficient way the path of line photons in arbitrary 3D gas distributions.

In this chapter I give a brief description of the codes CRASH and MCLyα for the sake of providing a proper background for the description of CRASHα given in the section at the end of this chapter.

2.1 CRASH: continuum radiative transfer

CRASH is a 3D ray-tracing radiative transfer code based on Monte Carlo (MC) techniques that are used to sample the probability distribution functions (PDFs) of several quantities involved in the calculation, e.g. spectrum of the sources, emission direction, optical depth. The MC approach and the code architecture assure a great flexibility in the application to a wide range of astrophysical problems and allow additional physics to be easily added with a minimum effort.

The algorithm follows the propagation of the ionizing radiation through an arbitrary H/He static density field and at the same time computes the variations in temperature and ionization state of the gas. In the current version of the code, the density field remains constant during the simulation, i.e. no back-reaction of gas-dynamics due to the effects of radiative transfer is considered. Both multiple point sources, located arbitrarily in the box, and diffuse radiation (e.g. the ultraviolet background or the radiation produced by H/He recombinations) can be accounted for. The quantities required as initial condition for the radiation field are the number, location and emission properties (e.g. the intensity of the emitted radiation and its spectral energy distribution) of point sources in the simulated volume, and the intensity and spectral energy distribution of the background radiation, if present. As CRASH has been specifically designed to follow the propagation of ionizing photons, the above spectral parameters are required only for energies $\geqslant 1$ Ryd (1 Ryd $= 2.18 \cdot 10^{-18} J$).

The energy emitted by point sources in ionizing radiation is discretized into photon packets, beams of ionizing photons, emitted at regularly spaced time intervals. More specifically, the total energy radiated by a single source of luminosity L_s, during the total simulation time, t_{sim}, is

$$E_s = \int_0^{t_{sim}} L_s(t_s) dt_s. \tag{2.1}$$

For each source, E_s is distributed in N_p photon packets, emitted at the source location at regularly spaced time intervals, $dt = t_{sim}/N_p$. The time resolution of a given run is thus fixed by N_p and the time evolution is marked by the packets emission: the j-th packet is emitted at time $t^j_{em,c} = j \times dt$, with $j = 0, ..., (N_p - 1)$., and it contains $N_{\gamma,j} = \Delta E_j / h\nu$

photons, where ΔE_j is the energy of the j-th packet given by:

$$\Delta E_j = \int_{t_{j-1}}^{t_j} L_s(t)dt. \tag{2.2}$$

Thus, the total number of emissions of continuum photon packets is $N_{em,c} = N_p$. In its latest version (Maselli, Ciardi & Kanekar 2009), the code allows for polychromatic packets whose content consists of photons distributed in various frequency bins which are populated according to the spectral shape assigned to the source.

The emission direction of each photon packet is assigned by MC sampling the angular PDF characteristic of the source. The propagation of the packet through the given density field is then followed and the impact of radiation-matter interaction on the gas properties is computed on the fly. Each time the packet pierces a cell i, the cell optical depth for ionizing continuum radiation, τ_c^i, is estimated summing up the contribution of the different absorbers (HI, HeI, HeII). The probability for a single photon to be absorbed in such a cell is:

$$P(\tau_c^i) = 1 - e^{-\tau_c^i}. \tag{2.3}$$

As the packet propagates through the above cell sequence, it will deposit in the i-th cell a fraction of its initial photon content $\propto P(\tau_c^i)$. For each cell crossed, the code computes the optical depth as follows:

$$\tau_c^i = \tau_{c;H^0}^i + \tau_{c;He^0}^i + \tau_{c;He^+}^i = \left[\sigma_{H^0}(\nu) n_{H^0}^i + \sigma_{He^0}(\nu) n_{He^0}^i + \sigma_{He^+}(\nu) n_{He^+}^i\right] f(l)\Delta x,$$

where σ_A is the photoionization cross-section for absorber $A \in \{H^0,\ He^0,\ He^+\}$, n_A^l its numerical density in i-th cell and $f(l)\Delta x$ the path length through the i-th cell of linear size Δx. Depending on the trajectory of the packets in the cell, $f(l)$ will have a value in the range $[0, \sqrt{3}]$. The number of photons absorbed in the cell i is the fraction $P(\tau_c^i)$ of packet content when entering the cell. In the polychromatic implementation, the same argument applies to the number of photons contained in each single frequency bin. The trajectory of the packet is followed until its photon content is extinguished or, if continuum boundary conditions are not assumed, until it exits the simulation volume.

The time evolution of the gas physical properties (ionization fractions and temperature) is computed solving in each cell the appropriate discretized differential equations each time the cell is crossed by a packet. The reader is referred to Maselli, Ferrara & Ciardi (2003) and Maselli, Ciardi & Kanekar (2009) for more details.

2.2 MCLyα: line radiative transfer

MCLyα is a numerical scheme for Lyα line radiative transfer, whose implementation is based on the basic structure of `CRASH` . MCLyα in fact uses the same MC sampling and ray-tracing techniques and it allows for arbitrary 3D hydrogen plus dust density distributions, as well as for arbitrary ionization, temperature and velocity fields.

2.2.1 Physical processes

To capture the essentials of radiation transfer in the UV including and around the Lyα line this code includes three main physical processes, dust absorption and scattering and the Lyα line transfer.

Lyα line transfer

In the whole section, the description of the Lyα radiative transfer equations are referred to a *static* medium. To adapt them to moving media, the code just converts frequencies to local co-moving frequencies and converts them back to the external frame by a Lorentz transformation, neglecting terms of order $O(v^2/c^2)$.

A Lyα photon corresponds to the transition between the $n = 2$ and $n = 1$ levels of a hydrogen atom. This is the strongest HI transition, with an Einstein coefficient given by $A_{21} = 6.265 \times 10^8$ s^{-1}. The scattering cross-section of a Lyα photon as a function of frequency in the rest frame of the hydrogen atom is:

$$\sigma_\nu = f_{12} \frac{\pi\, e^2}{m_e\, c} \frac{\Gamma/4\,\pi^2}{(\nu - \nu_0)^2 + (\Gamma/4\,\pi)^2}, \tag{2.4}$$

where $f_{12} = 0.4162$ is the Lyα oscillator strength, $\nu_0 = 2.466 \times 10^{15}$ Hz is the line center frequency, and $\Gamma = A_{12}$ is the damping constant which measures the natural line width.

The optical depth $\tau_\nu(s)$ of a photon with frequency ν traveling a path of length s is determined by convolving the above cross-section with the velocity distribution characteristic of the absorbing gas, and is of the form:

$$\tau_\nu(s) = \int_0^s \int_{-\infty}^{\infty} n(V_z)\, \sigma_\nu\, dV_z\, dl, \tag{2.5}$$

where V_z denotes the velocity component along the photon's direction. Thermal motions of hydrogen are described by a Maxwellian distribution of atoms velocities whose velocity

dispersion, $V_{th} = (2\,k_B\,T/m_{\rm H})^{1/2} = 12.85 T_4^{1/2}$ km s^{-1}, corresponds to the Doppler frequency width $\Delta\nu_D = (V_{th}/c)\nu_0$. Here T_4 is the gas temperature in units of 10^4 K.

Let introduce now some useful variables. First the frequency shift in Doppler units

$$x = \frac{\nu - \nu_0}{\Delta\nu_D} = \frac{V}{b}, \tag{2.6}$$

Second the Voigt parameter $a \equiv \frac{\Gamma/4\,\pi}{\Delta\nu_D} = 4.7 \times 10^{-4}\,T_4^{-1/2}$. Adopting this notation, it can be shown that:

$$\tau_x(s) = \sigma_H(x)\,n_H\,s = 1.041 \times 10^{-13}\,{T_4}^{-1/2}\,N_H\,\frac{H(x,a)}{\sqrt{\pi}} \tag{2.7}$$

where n_H is the neutral hydrogen density, and N_H the corresponding column density. The Hjerting function $H(x,a)$ describes the Voigt absorption profile,

$$H(x,a) = \frac{a}{\pi}\int_{-\infty}^{\infty}\frac{e^{-y^2}dy}{(y-x)^2+a^2} \approx \left\{\begin{array}{ll} e^{-x^2} & \text{if } |x| < x_c \\ \frac{a}{\sqrt{\pi}x^2} & \text{if } |x| > x_c \end{array}\right. \tag{2.8}$$

which is often approximated by a central resonant core and power-law "damping wings" for frequencies below/above a certain boundary frequency x_c between core and wings. For a in the range of 10^{-2} to 10^{-6}, x_c varies typically from 2.5 to 4.

To characterize the depth of a static medium the code will use τ_0, the optical depth at line center:

$$\tau_0(s) = 1.041 \times 10^{-13}\,T_4^{-1/2}\,N_H\,\frac{H(0,a)}{\sqrt{\pi}} \tag{2.9}$$

$$\approx 3.31 \times 10^{-14}\,T_4^{-1/2}\,N_H. \tag{2.10}$$

This monochromatic optical depth τ_0 has been used in most recent studies (e.g. Ahn et al- 2001, 2002; Zheng & Miralda-Escudé 2002, Hansen & Oh 2006); however, it differs from the total Lyα optical depth $\tau_0^{\rm Neuf}$ used in the classical work of Neufeld (1990) by $\tau_0^{\rm Neuf} = \tau_0\sqrt{\pi}$.

Once the absorption probability is given and before the Lyα photon is re-emitted, its frequency and angular distribution must be determined. If the atom is not perturbed by collisions during the time a Lyα photon is absorbed and re-emitted, the frequencies before and after scattering are identical in the atom's rest-frame. On the other hand, when the atom undergoes a collision, the electron is reshuffled on another energy level and the frequencies before and after scattering are uncorrelated. Given the typically low densities in astrophysical media, the code assumes coherent scattering.

Concerning the angular redistribution, the code can model the case of isotropic as well as the more realistic dipolar redistribution.

Dust scattering and absorption

During its travel in an astrophysical medium, the Lyα photon will diffuse on H atoms, but it can also interact with dust: it can either be scattered, or absorbed. The dust cross-section σ_d is composed of an absorption cross-section σ_a, and a scattering cross-section σ_s:

$$\sigma_d = \sigma_a + \sigma_s \tag{2.11}$$

where $\sigma_{a,s} = \pi\, d^2\, Q_{a,s}$, with d the typical dust grain size which will affect Lyα photons, and $Q_{a,s}$ the absorption/scattering efficiency. At UV wavelengths the two processes are equally likely, $Q_a \approx Q_s \approx 1$, so the dust albedo $A = Q_s/(Q_a + Q_s)$ is around 0.5: half of the photons interacting with dust will be lost, and half will be re-emitted in the Lyα line.

The code assumes that the dust density n_d is proportional to the neutral H density in each cell

$$n_d = n_H \times \frac{m_{\rm H}}{m_d}\,\frac{M_d}{M_{\rm H}}, \tag{2.12}$$

where m_d is the grain mass and $m_{\rm H}$ the proton mass. The relevant quantity, τ_d given just below, is described by one free parameter, the dust to gas ratio $\frac{M_d}{M_{\rm H}}$ assuming $d = 10^{-6}$ cm and $m_d = 3 \times 10^{-17}$ g. The total (absorption + scattering) dust optical depth seen by a Lyα photon is then:

$$\tau_d = \tau_a + \tau_s = \int_0^s \sigma_d\, n_d(s)\, ds. \tag{2.13}$$

The relation between the dust absorption optical depth at Lyα wavelength $\tau_a = (1 - A)\tau_d$ and the color excess E_{B-V} is given by

$$E_{B-V} = 1.086 \frac{A_V}{A_{1216}\, R}\, \tau_a \approx (0.06 \ldots 0.11)\, \tau_a \tag{2.14}$$

where A_V and A_{1216} is the extinction in the V band and at 1216 Å respectively, R the total-to-selective extinction. The smaller numerical value corresponds to a Calzetti et al.(2000) attenuation law for starbursts, the larger to the Galactic extinction law from Seaton (1979).

2.2.2 Monte Carlo radiation transfer

The code follows the emission and propagation of each single photon emitted by any source, until it escapes the simulation volume or is absorbed by dust. Let us now describe the travel followed by a photon.

Initial emission

The emission of a photon is characterized by an emission frequency and direction. The frequency ν (here in the "external", i.e. observer's frame) samples the source spectrum representing usually Lyα line emission and/or UV continuum photons. For media with constant temperature, ν or more precisely the emission frequency shift from the line center, is conveniently expressed in Dopper units, i.e. $x = (\nu - \nu_0)/\Delta\nu_D$ (cf. Eq. 2.6).

The code assumes that the source emission is isotropic (in the local co-moving frame, if the considered geometry is not static). Thus the emission direction, described by the two angles θ and ϕ, is randomly selected from

$$\theta = cos^{-1}(2\,\xi_1 - 1) \tag{2.15}$$

$$\phi = 2\,\pi\,\xi_2 \tag{2.16}$$

where $\xi_{1,2}$ are random numbers, $0 \leqslant \xi_{1,2} < 1$. The photon travels in this direction until it undergoes an interaction. In moving media, the photon frequency in the external frame is evaluated by a Lorentz transformation.

Location of interaction

The location of interaction is determined as follows. The optical depth, τ_{int}, that the photon will travel is determined by sampling the interaction probability distribution $P(\tau) = 1 - e^{-\tau}$ by setting

$$\tau_{int} = -ln(1 - \xi) \tag{2.17}$$

where ξ is another random number.

The total optical depth, τ, encountered by the photon along its path s is given by the sum:

$$\tau(s) = \tau_x(s) + \tau_d(s), \tag{2.18}$$

where $\tau_x(s)$ and $\tau_d(s)$ are defined respectively in eq. 2.7 and eq. 2.13 This determines the length s corresponding to $\tau(s) = \tau_{int}$. The code calculates the coordinates corresponding

to a travel of length s in the direction (θ, ϕ) starting from the emission point. This is the location of interaction. Now, the code has to compute if the Lyα photon interacts with a dust grain or a hydrogen atom.

Interaction with H or Dust ?

The probability to be scattered by a hydrogen atom is given by:

$$P_{\rm H}(x) = \frac{n_H \sigma_H(x)}{n_H \sigma_{\rm H}(x) + n_d \sigma_d}, \tag{2.19}$$

where $\sigma_{\rm H}(x) = f_{12} \frac{\pi e^2}{m_e c \Delta\nu_D} H(x,a)$ is the hydrogen cross section for a Lyα photon of frequency x. The code generates a random number $0 \leqslant \xi < 1$ and compares it to $P_{\rm H}$: if $\xi < P_{\rm H}$, the photon interacts with H, otherwise it is scattered or absorbed by dust.

Scattering on H atoms

After the interaction with an H atom, the code first converts the frequency in the external (observers) frame, ν_{ext}, to the comoving frequency of the fluid, ν_{int}, with a Lorentz transformation

$$\nu_{int} = \nu_{ext}(1 - \frac{\vec{k_i} \cdot \vec{V}}{c}), \tag{2.20}$$

where $\vec{k_i}$ is the photon direction and $\vec{V}$ the macroscopic/bulk velocity of the H atoms. Due to the thermal motion of H atoms, scattering in the fluid comoving frame is not perfectly coherent. Within the comoving framework and neglecting the recoil effect, partially coherent scattering can be described with a simple relation between the incoming, x_{in}, and the outcoming, x_{out}, frequency (Dijkstra, Haiman & Spaans 2006):

$$x_{out} = x_{in} - \frac{\mathbf{V}_a \cdot \mathbf{k}_{in}}{V_{th}} + \frac{\mathbf{V}_a \cdot \mathbf{k}_{out}}{V_{th}}. \tag{2.21}$$

In the above equation $\mathbf{V}_a$ is the atom velocity, while $\mathbf{k}_{in}$ and $\mathbf{k}_{out}$ are respectively the incoming and outcoming propagation direction. After scattering, the new frequency is again converted back to the external frame.

Dust scattering and absorption

When the photon interacts with dust, the code generates a random number $0 \leqslant \xi < 1$ determining whether it is absorbed or scattered. In practice, if $\xi < A = Q_s/(Q_a + Q_s)$ the photon is scattered by dust and simply reemitted coherently. Otherwise the photon

is absorbed by dust and is considered lost for the present simulation. The dust scattering is assumed isotropic.

2.3 CRASHα: combining continuum and line transfer

In this Section I describe CRASHα, the first numerical scheme which combines the treatment of continuum and line transfer radiation. As mentioned in the introduction, the algorithm has been developed as an extension of CRASH, which provides the treatment of the ionizing radiation as described in the previous Section and references therein. The extension indeed consists in a new algorithm developed to follow the propagation of Lyα photons through a given gas configuration while it is changed by ionizing radiation. In fact, although the continuum photon propagation proceeds undisturbed by the Lyα radiation field, Lyα radiative transfer is strongly affected by the change in the ionization state of the gas.

In order to perform the coupling, it is necessary to introduce the time evolution for Lyα propagation, a feature commonly neglected in line radiative transfer codes like MCLyα. This is a crucial aspect because, due to the resonant scattering nature of Lyα transfer in a neutral medium, Lyα radiation can remain trapped for a substantial fraction of the simulation lifetime before being able to propagate away from its emission site, while the propagation time of the ionization front can be much shorter. Thus, the change in the degree of ionization affects the propagation of the Lyα photons, while the latter induces a back reaction on the gas with a very small effect. Note that, although Lyα photons, via scattering, can transfer some of their energy to the gas and heat it, in typical situations the effect is negligible and thus such heating is not generally included in Lyα radiative transfer codes. However I study the exchange of energy between gas and Lyα photons in the last Chapter.

To correctly model the simultaneous propagation of the two radiations a combined approach is needed. This is a challenging task because of the very different nature of continuum and line transfer, in terms of e.g. their path (straight line versus random walk) and time-scales (see discussion above). The above differences are reflected also in the numerical implementation of line and continuum radiative transfer. For example, while in the case of ionizing radiation the time needed for a photon packet to travel a

given distance does not depend sensibly on the physical properties of the gas but only on the physical distance crossed, the propagation of Lyα photons is very sensitive to the ionization state of the gas and extreme configurations can be faced, in which the Lyα photons scatter for the entire simulation time trapped in few cells without exiting the simulation volume.

As the ionizing radiation scheme has not been modified, it will not be discussed further and in the following I will focus on describing the details of the line transfer part of the algorithm.

The Lyα radiation is discretized in a large number of photon packets whose emission and propagation is dictated by the time-scale attached to the ionizing radiation evolution. In this way the code is able to model the change in the Lyα propagation due to the variations in the gas ionization state. To correctly model the propagation of Lyα photons the code needs to follow every single scattering. As this would require a very large computational time, I use a statistical approach to the Lyα treatment. I have compiled 1085 tables by running MCLyα, in order to describe the physical characteristics of a photon after a scattering depending on the temperature and density of the gas and on the incoming photon frequency (see Appendix A.1). The dust is not considered at the moment of the tables compilation. I will show later a treatment of dust in `CRASH`α . The following part of this Section is dedicated to a description of the various steps of the implementation.

2.3.1 Emission of Lyα photons

Every Lyα emission is characterized by the generation of $N_{\gamma,l}$ Lyα line photon packets emitted at the same time, $t^i_{em,l}$. The parameter $N_{\gamma,l}$ is chosen to optimize the resolution and the code performance. The code allows for two different methods for photon packet emission. In the first method the emission is regularly spaced in time as in the continuum emission. If, as in Section 2.1, I define $N_{em,l}$ as the total number of emissions of line photon packets, in this case:

$$t^i_{em,l} = i \times \frac{t_{sim}}{N_{em,l}}, \tag{2.22}$$

with $i = 0, ..., (N_{em,l} - 1)$.

An alternative criterion for the emission follows the evolution of the ionization structure.

In this case the emission time, $t^i_{em,l}$, is linked to the volume averaged H ionization fraction, $\chi_{\rm HII,em}$, and Lyα photon packets are emitted at the time $t^i_{em,l}$ when:

$$\chi^i_{\rm HII,em} = i \times \Delta\chi_{\rm HII}. \tag{2.23}$$

$\Delta\chi_{\rm HII} = 1/N_{em,l}$ is the chosen HII fraction variation in the gas and i is an integer that covers values between 0 and $N_{em,l} - 1$. While in the first formulation a constant Lyα emission rate is assured, in this case the emission rate is higher when the ionization state of the gas changes faster. In order to reproduce a constant emissivity even in the second formulation, the code assigns a weight to each photon packet emitted at the i-th step: $w^i_{ph} = \left(t^i_{em,l} - t^{i-1}_{em,l}\right)/t_{sim}$. When a Ly$\alpha$ spectrum is built, each photon packet contributes according to its weight. This allows to modulate the emission of Lyα photon packets based on the change of the ionization degree (and thus to better sample the effect of ionization on Lyα scattering) and at the same time to have a constant Lyα photon packet rate.

In the following tests the emission is assumed to be isotropic, but it is always possible to account for an arbitrary angular PDF.

Every emitted Lyα photon packet k ($k \in [1, N_{\gamma,l} \times N_{em,l}]$) is described by its frequency in the comoving frame $x_{in,k}$ (in this case I assume a monochromatic spectrum with $x_{in,k} = 0$, but a different spectrum can be used), position $\mathbf{p}_k$ (which coincides with the source location), direction of propagation $\mathbf{k}_{in,k}$, optical depth at which the scattering takes place $\tau_{scatt,k}$ (as defined in Sec. 2.2) and a characteristic time $t_{ch,k} = t^i_{em,l}$ that is used to evolve the photon packet along the simulation timeline (see next Section). At any step of the simulation the k-th photon packet is always described by the quantities (x_{in}, $\mathbf{p}$, $\mathbf{k}_{in}$, τ_{scatt}, t_{ch}), where the index k has been omitted for clarity. In the following, I will always omit it.

2.3.2 Propagation of Lyα photons

In Section 2.1 I have shown how the physical time of the simulation is driven by the emission of packets of ionizing radiation discretized in time units, dt. Now I want to link the propagation of a Lyα photon packet to this timeline.

Let's assume that an ionizing photon packet has been emitted at $t^j_{em,c}$, that the physical state of the gas has been evolved between $t^j_{em,c}$ and $t^{j+1}_{em,c}$, and that a Lyα photon packet

is emitted at the same time $t^i_{em,l} = t^j_{em,c}$; then its characteristic time is assigned the value $t_{ch} = t^i_{em,l}$. The propagation of the Lyα photon packet along the direction $\mathbf{k}$ is followed between t_{ch} and $t^{j+1}_{em,c}$, and the line optical depth encountered along the path, τ_l, is calculated as described in Section 2.2. In each cell crossed by the photon packet the code checks if a scattering takes place, i.e. if τ_l becomes larger than τ_{scatt}. If there is no scattering, it follows the propagation until $t^{j+1}_{em,c}$ and at this point it stores the photon packet's frequency x_{in}, the updated position $\mathbf{p} = \mathbf{p} + (c\ dt)\mathbf{k}$, and characteristic time $t_{ch} = t^{j+1}_{em,c}$. Propagation direction $\mathbf{k}_{in}$ and optical depth for scattering τ_{scatt} remain unchanged. These information will be used to follow the photon packet evolution in the next time unit. I define this photon packet as "active", in the sense that it is not trapped by scattering inside a cell but will resume its propagation in the next time unit.

Let's consider now the case in which the photon packet scatters during the time unit. Unlike MCLyα, this code does not follow every scattering inside the cell, but determines the properties of the outcoming photon packet by interpolation of pre-compiled tables (see Appendix A.1).

Once the location of the scattering is identified within a cell, around it the code builds a new, smaller cell with length equivalent to the shortest distance between the scattering's location and the boundary of the cell. The physical and dynamic gas conditions are the ones of the original cell. As the tables are built with photons that scatter in the center of a cell, the above procedure removes the dependence on the position of the incoming photon packet. Given the gas temperature, T_{cell}, the line optical depth, τ_{cell}, of the newly built cell, and the frequency, x_{in}, of the incoming photon packet, a linear interpolation of the tables is performed to obtain the distribution of frequencies of the outcoming photon packet, x_{out}, and of the time interval that the photon packet is expected to spend inside the cell due to scattering, t_{scatt}. From these distributions the code extracts the values for x_{out} and t_{scatt} that will be assigned to the photon packet. This approach allows for a tremendous gain in computational speed by adopting a statistical description of the scatterings that occur to the photon packet inside a cell, without following each one individually. The characteristic time is updated as $t_{ch} = t_{ch} + t_{scatt}$. If $t_{ch} > t^{j+1}_{em,c}$ the photon packet is put in a "stand-by" mode and its propagation is resumed (with a new τ_{scatt}) only when the simulation time becomes larger than t_{ch}.

The procedure described above is repeated for *(i)* all the Lyα photon packets emitted

at $t^i_{em,l}$, *(ii)* all the Lyα photon packets "active" at $t^j_{em,c}$ and *(iii)* all the Lyα photon packets that exit the "stand-by" mode in this time unit. Then, a new ionizing photon packet packet is emitted at $t^{j+1}_{em,c}$ and after it has been evolved up to $t^{j+2}_{em,c}$ the Lyα cycle starts again: all the "active" photon packets are evolved from $t^{j+1}_{em,c}$ to $t^{j+2}_{em,c}$; if there are "stand-by" photon packets with $t^{j+1}_{em,c} < t_{ch} < t^{j+2}_{em,c}$ they are turned into "active" photon packets and evolved until $t^{j+2}_{em,c}$; if new Lyα photon packets are emitted in this time unit they as well are evolved until $t^{j+2}_{em,c}$.

If the ionizing radiation crosses a cell in which a Lyα photon packet is trapped by scattering, the change in the physical conditions of the cell should be taken into account, as this affects the characteristics of the outcoming photon packet. To include this effect, the code uses tables which give the time evolution of the frequency distribution of photon packets trapped in a cell as a function of the same input parameters x_{in}, τ_{cell}, T_{cell}. As an example, let's assume that a Lyα photon packet scatters in a cell at $t_{s,0}$ and that the time at which it exits the "stand-by" mode is $t_{ch} = t_{s,2}$. If the ionizing radiation crosses that cell at a time $t_{s,1}$ such that $t_{s,0} < t_{s,1} < t_{s,2}$, the physical conditions in the cell change. To take into account the effect on x_{out} and t_{scatt}, CRASHα proceeds as follows:

- it computes how much time the photon packet spent in the cell, $t_{s,1} - t_{s,0}$;
- it samples the distribution of frequencies at that time, interpolating the tables mentioned above;
- it extracts a new frequency, $x_{in,1}$, and recalculates x_{out} and t_{scatt} using the values $T_{cell}(t_{s,1})$, $\tau_{cell}(t_{s,1})$ modified by the ionizing radiation and $x_{in,1}$.

2.3.3 Spectrum of Lyα photons

When photon packets exit the simulation box, their frequencies are collected to calculate the outcoming time integrated spectrum. As discussed in Section 2.3.1, each photon packet is counted according to its weight. To show the probability distribution of the outcoming Lyα radiation, spectra are normalized to the sum of all weights. The profile of the final spectrum strongly depends on the choice of the integration time. To build a spectrum I define an initial, t^l_{out}, and a final, t^{l+1}_{out}, time. All the photon packets that escape from the box in the interval $]t^l_{out}; t^{l+1}_{out}]$ will contribute to the spectrum of the source. At the next output, all the photon packets collected in the interval $]t^{l+1}_{out}; t^{l+2}_{out}]$ will be used

to build the spectrum. This procedure is followed until the end of the simulation. As in the case of the emission described in Section 2.3.1, the spectra can be produced regularly spaced in time or linked to the evolution of the ionization structure. Thus, the time of the outputs is regulated by equations 2.22 and 2.23, where $t^i_{em,l}$ and $N_{em,l}$ are replaced by t^l_{out} and N_{out}, respectively.

Spectra can also be built by choosing a pre-determined line of sight.

Chapter 3

Tests of the CRASHα Implementation

In this chapter I will present several tests performed for the parallel propagation of ionizing and Lyα radiation, which show how the evolution of the ionization structure alters the Lyα spectra of the outcoming radiation. All the tests have the same initial conditions, unless stated otherwise. I used a simulation box of 30 pc on a side, divided in 128^3 cells. A monochromatic ionizing source, emitting photons with energy equal to 13.6 eV, is located at the center of the box; the ionizing photon rate is $5 \times 10^{49} \mathrm{s}^{-1}$. The ionizing radiation is discretized in $N_p = 10^7$ photon packets. The same source emits also a Lyα monochromatic radiation. As I want to construct spectra at a fixed distance from the source, I distribute the gas (H only, with density $n_{\mathrm{H}} = 1$ cm^{-3}, $N_{\mathrm{HI}} \sim 5 \times 10^{18}$ cm^{-2}, and temperature $T = 10^4$ K) in a sphere of radius $r_{sph} = 15$ pc around the central source. Outside the sphere the density is set to zero, so that no interaction between radiation and gas takes place. The gas is initially neutral. Every simulation is carried out for a physical time of $t_{sim} = 10^5$ yr. In my reference runs I have $N_{out} = 50$ outputs and $N_{em,l} = 100$ emissions of Lyα photon packets, each with $N_{\gamma,l} = 10^4$ photon packets. Both the emissions and the outputs are dictated by the evolution of the ionization field. I will discuss the effect of a different choice for $N_{em,l}$, $N_{\gamma,l}$ and N_{out} at the end of the Section. In the following I present the results of my simulations for different choices of the dynamical state of the gas. The spectra shown are obtained integrating on all directions in order to achieve a better resolution, given the set of chosen parameters.

3.1 Static sphere

In this first test, the gas has no bulk velocity with respect to the central source. The top-left panel in Figure 3.1 shows the spectra emerging from this configuration at times corresponding to volume averaged ionization fractions $\chi_{\rm HII} = 0.3, 0.5, 0.8, 0.9, 0.99$, which could be regarded as spectra of the source observed at different times elapsed since the source switches on.

The spectra shown here and in the rest of the thesis have been built as described in Section 3.3., i.e. collecting the Lyα photon packets escaping the system when $\chi_{\rm HII}$ falls in an interval $\Delta\chi_{\rm HII} = 0.02$ centered on the $\chi_{\rm HII}$ value selected for the output. The curve corresponding to $\chi_{\rm HII} = 0.99$ is instead a collection of the escaping photon packets which starts when $\chi_{\rm HII} = 0.98$ and ends at t_{sim}. For the combination of parameters chosen for the tests, at $\chi_{\rm HII} < 0.3$ the number of escaped Lyα photon packets is not sufficient to build a spectrum and also for $\chi_{\rm HII} = 0.3$ the outcoming spectrum is very noisy. As expected, the spectra exhibit the two symmetric peaks characteristic of this configuration, although a direct, quantitative comparison with previous works (i.e. Dijkstra, Haiman & Spaans 2005) is not possible, as none included the effect of ionizing radiation. As the ionization increases, the peaks move towards $x = 0$ because Lyα photon packets encounter less and less HI atoms along their path. At the same time, the width of the peaks become smaller. In this scenario we do not see a spectrum peaked at $x = 0$ because the gas never gets completely ionized and, for a static configuration, also a little fraction of neutral gas far from the location of emission has a non negligible optical depth for photons in the line center.

3.2 Expanding and collapsing sphere

In a more interesting case I simulate a homogeneous spherical cloud that collapses or expands. In these tests I sample a velocity field, in the gas sphere, described by $V(r) = V_{max} r/r_{sph} + V_0$.

Initially I choose $V_{max} = \pm 200$ km s^{-1} and $V_0 = 0$ km s^{-1}. The resulting spectra extracted at the same ionization fractions as for the static case are shown in Figure 3.1 with a positive and a negative value for V_{max} (top-right and center-left panels respectively). As expected, the plots show specular Lyα spectra, due to the opposite direction of the

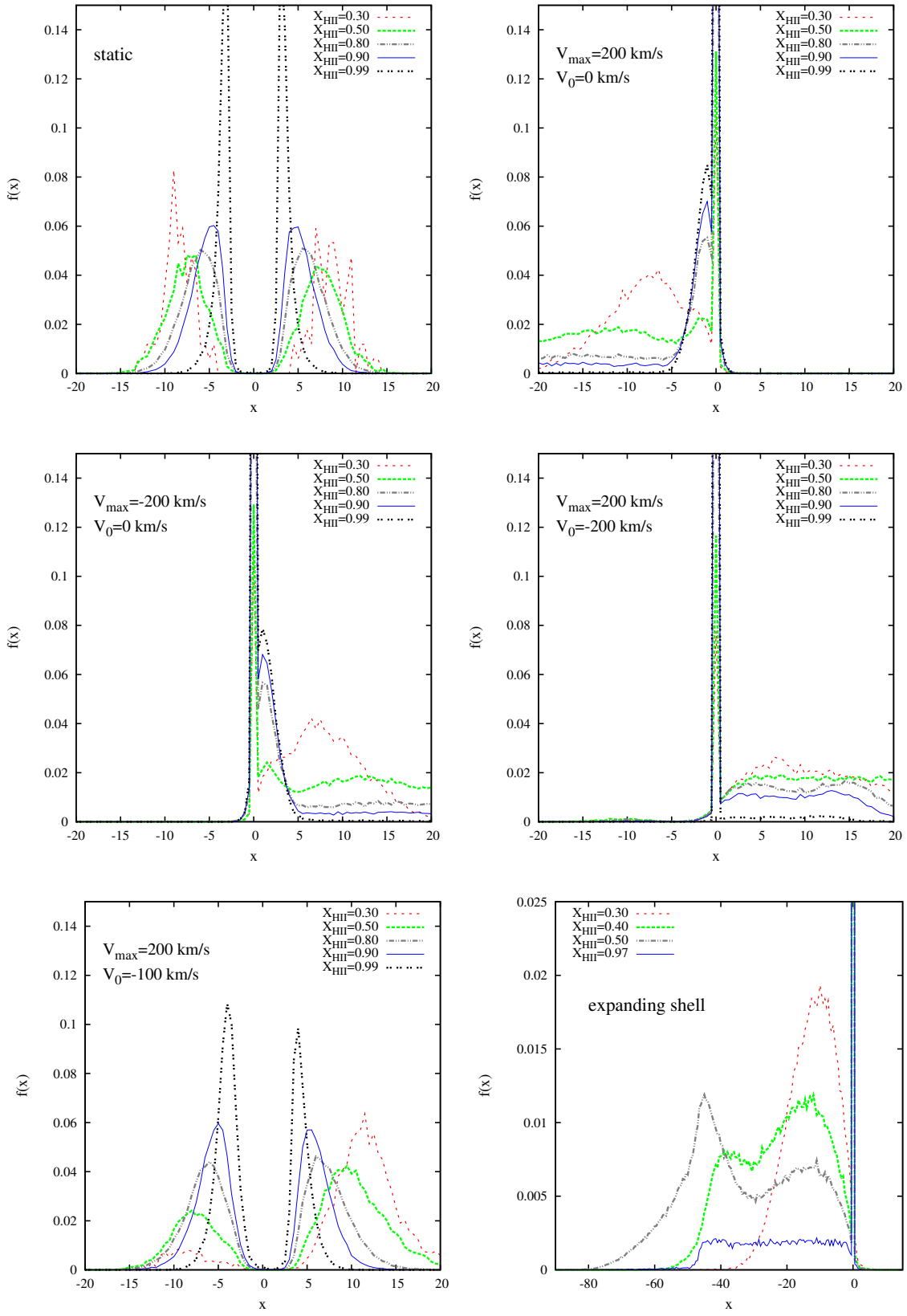

Figure 3.1: Spectra of Lyα outcoming radiation at times corresponding to ionization fractions $\chi_{\rm HII} = 0.3, 0.5, 0.8, 0.9, 0.99$ (with the exception of the bottom-right panel for which $\chi_{\rm HII} = 0.3, 0.4, 0.5, 0.97$). The dynamic condition of the gas is the following: static gas (upper-left panel), homogeneous spherical cloud expanding and collapsing with velocity increasing with distance from the source (upper-right and center-left panels), homogeneous spherical cloud collapsing with velocity decreasing with distance from the source (center-right and bottom-left panels), shell expanding at constant velocity (bottom-right panel).

bulk motion. When the gas is expanding the outcoming radiation is on the red part of the spectrum, while it lays on the blue side when we consider negative values for the velocity. This happens because the photon packets are seen Doppler shifted according to the velocity of the atoms. This means that, if an atom has a positive velocity, in the atom rest frame a blue photon packet becomes a line center photon packet and is easily blocked by the higher optical depth (compared to the optical depth in the wings). Thus, a photon packet can escape only if it is shifted by scattering to the red side of the line. Differently from the static case, here it is possible to have Lyα radiation at the central frequency $x = 0$ also when ionization is not complete. This is a consequence of the fact that, due to the Doppler effect, the line center photon packets are seen in the atom rest frame as red (expanding gas) or blue (collapsing gas) photon packets, i.e. in the wing, and thus encounter a lower optical depth. In addition, the higher is the absolute value of the velocity the bigger is the shift, so when the continuum radiation ionizes the regions closer to the source (which have lower velocity and as a consequence a higher contribution to the opacity), the optical depth at the center decreases significantly because the external neutral layers of gas (with a higher velocity) give only a minor contribution. As a result, as ionization proceeds, we start seeing an increasing emission at the central frequency. More specifically, the spectrum corresponding to $\chi_{\rm HII} = 0.3$ shows radiation at $x = 0$ and a residual in the red (blue) part of the spectrum for positive (negative) velocities. As ionization proceeds, the residuals become less pronounced and move towards the center, while the central radiation becomes stronger. In the last spectrum, when the gas is 99% ionized, there is still a residual because of the remaining neutral hydrogen fraction in the most distant regions of the gas sphere, where the photo-ionization rate is suppressed by geometrical dilution and by the residual inner opacity.

In the third case I consider a gas sphere collapsing with increasing velocity towards the center. The center-right panel of Figure 3.1 shows Lyα profiles generated with a bulk motion characterized by $V_{max} = 200$ km s^{-1} and $V_0 = -200$ km s^{-1}. These spectra are very similar to the ones obtained in the previous case, but as the absolute value of the velocities increases towards the center, the residual blue part of the spectra is more spread. Note that also in this case the residual is reduced as ionization proceeds and the contribution to the opacity from the inner layers of gas is suppressed.

In the last case (Fig. 3.1, bottom-left) I consider a gas which is collapsing near

the source while the outer shells are expanding, with $V_{max} = 200$ km s^{-1} and $V_0 = -100$ km s^{-1}. The first Lyα spectrum (at $\chi_{HII} = 0.3$) is dominated by photon packets in the blue part and just a residual is present on the red side. In fact, blue photon packets have a larger probability to escape because the ionization front has not yet propagated far enough to suppress the contribution to the Lyα gas opacity from the gas collapsing towards the source. As the front proceeds ionizing the neutral hydrogen with negative velocities (spectra at increasing $\chi_{\rm HII}$), the red part of the spectrum becomes stronger while the blue part is suppressed, until, in the configuration with $\chi_{HII} = 0.99$, it is smaller than the red one. As in the other tests, the increment in the ionization degree reduces the number of scatterings, with the consequence of moving the two peaks towards the center, increasing their height and reducing their width.

3.3 Expanding shell

In this Section I examine the case of a Lyα source surrounded by an expanding shell, which has been extensively studied also by other authors (Ahn, Lee & Lee 2004; Hansen & Oh 2006; VSM06). Here, I am interested in the effects introduced on the Lyα spectrum by an ionizing source inducing a time evolution of the neutral gas in the shell. To simulate this configuration I have chosen a homogeneous density $n_{\rm H} = 15$ cm^{-3}, temperature $T = 10^4$ K, and radial velocity $V = 300$ km s^{-1}. All the gas is distributed within a shell of thickness 4 pc located at a distance of 10 pc from the source, while no gas is present outside the shell. The corresponding column density is $N_{\rm HI} \sim 2 \times 10^{20}$ cm^{-2}. To show the Lyα spectrum time evolution, I choose to plot the profiles corresponding to ionization fractions in the shell of $\chi_{\rm HII} = 0.30, 0.40, 0.50, 0.97$ (Fig. 3.1, bottom-right panel). For a better understanding of the spectral features, it is useful to discuss the possible different paths for an outcoming photon packet. Following VSM06 (see their Fig. 12), I divide the outcoming photon packets in three different groups, depending on their scattering history:

- Backscattered photons: photon packets that, after scattering in the shell, travel inward across the empty space before crossing again the shell. As these photon packets undergo multiple scatterings with the gas, they can escape once they are shifted on the red side of the line where the optical depth of the expanding shell is smaller.

- Diffused photons: all the photon packets which are diffused in the shell until they escape without backscattering. I expect these photon packets to contribute to a red bump in the spectra whose shift from the line center and intensity will depend on the neutral gas density and on the shell velocity. Typically the frequency shift will be smaller than for backscattered photons as the number of scatters before escape is on average lower.

- Directly escaped photons: photon packets that have no interaction with the gas and keep their initial frequency; in my case this group of photon packets will produce a peak at $x = 0$.

It is important to underline that every group has a different characteristic time for escaping. In fact, directly escaped photons travel the shortest path. On the other hand, diffused photons scatter in a volume smaller than the backscattered photons and thus escape faster; therefore the red bump associated to the diffused photons will typically appear before the feature produced by the backscattered photons.

Keeping in mind all the possible paths for Lyα photon packets, let us analyze the features in the spectra shown in the Figure 3.1 (bottom-right panel). The first profile ($\chi_{\rm HII} = 0.3$) exhibits a peak on the red side of the central emission, due to the diffused photons, that, as already mentioned, escape faster than backscattered photons and can already be seen in the initial stages of the shell ionization. Directly escaped photons are present as well and their abundance increases with time. In the profile corresponding to an ionization degree of $\chi_{\rm HII} = 0.4$ we can clearly see that a secondary bump is forming at lower frequencies. At this stage of the evolution, the backscattering photons are starting to escape from the shell with a frequency that is more shifted respect to the other photon packets, as explained above. When the ionization degree is $\chi_{\rm HII} = 0.5$, the backscattering bump is visible and dominant on the red peak due to diffused photons. In the profile corresponding to $\chi_{\rm HII} = 0.97$ the ionization front has suppressed most of the neutral gas and only a negligible fraction of Lyα radiation interacts with the residual gas in the shell; the result is a small fraction of photon packets shifted on the spectrum's red side.

3.4 Effect of ionizing radiation

In the previous tests I have discussed how my time dependent treatment of the Lyα radiation allows to correctly establish the appearance at different times of spectral features which are usually integrated in the emergent spectra predicted with time independent formulations. Here I investigate further on the importance of the joint propagation of Lyα and continuum radiation, by comparing results from two different approaches to simulate the Lyα spectra. The first one, widely used in the literature, performs a Lyα radiative transfer on a gas configuration given as initial condition, which can be e.g. a constant density field or a snapshot of a numerical simulation. In this case, the gas configuration is kept constant throughout the entire Lyα radiative transfer and the Lyα spectra are built once all the Lyα photon packets have escaped the simulation volume. The other approach is the one described in this thesis, i.e. starting from an initial gas configuration, the parallel propagation of continuum and line photon packets is followed and the Lyα spectra can be built at different times taking into full account the changes in the Lyα propagation due to the variations in the neutral gas distribution.

To show the impact of the two different approaches on the outcoming Lyα spectra, I consider the same configuration described in Section 3.3, i.e. an initial neutral expanding shell which is ionized by a central source emitting also Lyα photon packets. I compare the spectra obtained with CRASHα at the times when the gas configuration is characterized by a mean ionization fraction inside the shell of $\chi_{\rm HII} = 0.32$ and 0.66, to those obtained running MCLyα on the same gas configurations. While with MCLyα the spectra are built by integrating over the Lyα photon packets once they have all escaped the fixed HI distribution, the CRASHα algorithm allows to account for the impact on the emergent spectra of the ionization history which led to those configurations. The results are shown in Figure 3.2.

A substantial difference is clearly visible in the spectra corresponding to $\chi_{\rm HII} = 0.32$. The Lyα spectrum simulated by MCLyα is characterized by two bumps associated with the diffused and backscattered photons. A very different profile is obtained with CRASHα, where no backscattered photon has escaped at this time and only the single red peak corresponding to the diffused photons is present. As already underlined in Section 3.3 the absence of backscattered photons is due to their larger escaping time. The profiles

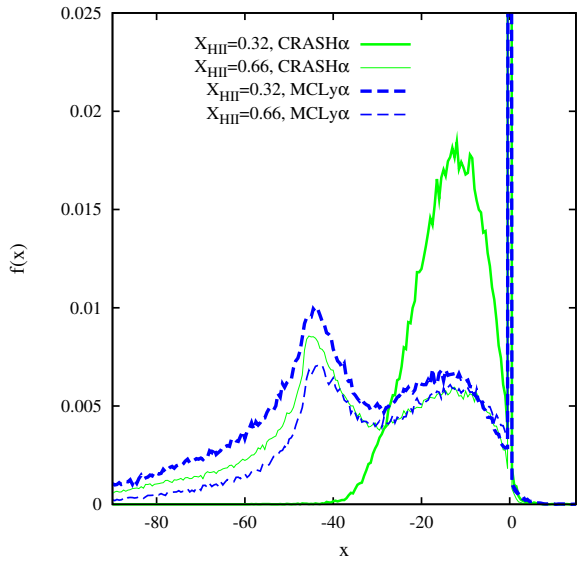

Figure 3.2: Comparison of Lyα spectrum obtained with MCLyα and CRASHα applied to the same gas distribution of an expanding shell. For the application of MCLyα a fixed gas configuration is used, while in my approach all the evolutionary stages are taken into account (see text for details).

corresponding to $\chi_{\rm HII} = 0.66$ are much more similar, because at this stage a significant fraction of the backscattered photons had enough time to escape the shell. Nevertheless, there is still a difference in the amplitude of the peak at $x = 0$ and of the bumps from the backscattered photons, which are also slightly more shifted. This difference is due to the memory of Lyα photon packets emitted in the previous stages of the source activity, when $\chi_{\rm HII} < 0.6$. In the MCLyα treatment all the emitted Lyα photon packets see the same mean shell opacity and the probability to have a direct escape is significantly higher then in the CRASHα run, in which the Lyα photon packets see on average a larger shell opacity. As a consequence, the fraction of photon packets with $x = 0$ in CRASHα is smaller and, at the same time, the photon packets that have remained trapped for a longer time exhibit a larger amplitude of the spectra and a larger shift to the red side of the central frequency. The time elapsed between the two spectra considered above is only about 100 yr. The time interval in which deviations from the "instantaneous picture" are significant is thus too small to allow observations to capture these stages. However, the example is useful to illustrate the relevant features and advantages of our approach. Furthermore the deviations found could affect the gas state, e.g. its spin temperature, independently from their observational detectability in the spectra.

A similar test has been performed to infer the observability of the deviations in the

spectra on larger scales. In this case I use a simulation box of 200 kpc on a side and a photo-ionization rate of the central source $\dot{N}_\gamma = 10^{54}\mathrm{s}^{-1}$. In this test the gas is distributed in a sphere of radius $r_{sph} = 70$ kpc, with density $n_\mathrm{H} = 0.01$ cm^{-3} (corresponding to $N_\mathrm{HI} \sim 2 \times 10^{21}$ cm^{-2}), while I keep the temperature $T = 10^4$ K; I also assume a velocity field corresponding to a Hubble expansion with H =790 km s^{-1} Mpc^{-1}. The simulation is carried out for a physical time of $t_{sim} = 10^8$ yr. In this case (Fig. 3.3) the first spectrum is captured at the time $t = 4.0 \times 10^6$ yr (corresponding to a mean ionization fraction of $\chi_\mathrm{HII} = 0.24$) and the second at the time $t = 8.3 \times 10^6$ yr ($\chi_\mathrm{HII} = 0.40$). While the MCLyα profile in the left panel of Figure 3.3, is characterized by a large red bump and a small blue one, with the `CRASH`α approach I find a lower fraction of photon packets escaping with blue frequencies and a larger red bump which is slightly shifted on redder frequencies. This effect results from keeping memory of the ionization history, since I take into account that before reaching the observed gas configuration most of the Lyα photon packets have been trapped on the boundary of the growing ionized region. The integrated optical depth along the full path traveled before escaping is therefore larger respect to the one computed in the MCLyα approach. This effect is also visible in the right panel of Figure 3.3, where a larger red shift is present. In this case a larger fraction of trapped photon packets are now free to escape and the shift is more evident.

The major result of these tests is that the emerging spectra keep memory of the ionization history which generates a given observed configuration and, to properly account for this effect, the self-consistent joint evolution of line and ionizing continuum radiation followed by my scheme is necessary. The extent of the difference between the two methods depends on the particular case considered, but it can be substantial and can thus affect the physical interpretation of the problems at hand.

In addition, the time evolution that builds up the Lyα radiation field can be important when calculating the impact of such radiation on gas properties like the spin temperature, which is relevant for the prediction of the observability of 21 cm emission from neutral hydrogen at high redshift.

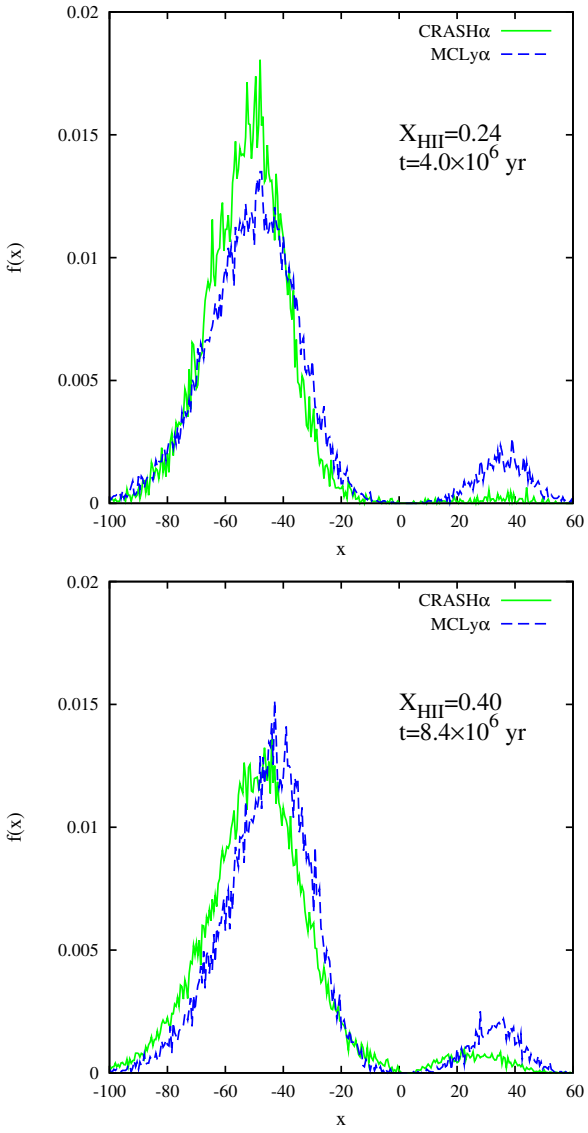

Figure 3.3: Comparison of Lyα spectrum obtained with MCLyα and `CRASH`α applied to the same gas distribution of an expanding sphere. The left (right) panel shows Lyα profiles at $t = 4.0 \times 10^6$ yr ($t = 8.4 \times 10^6$ yr). See text for more details.

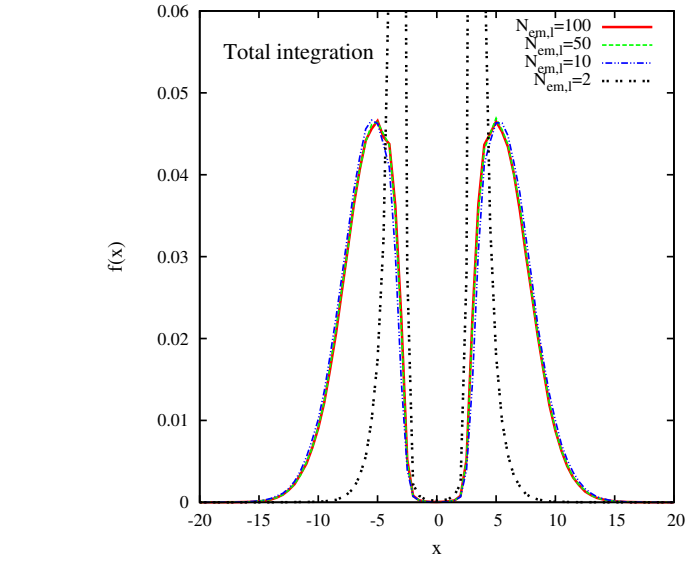
Total integration
N_em,I=100
N_em,I=50
N_em,I=10
N_em,I=2
f(x)
x

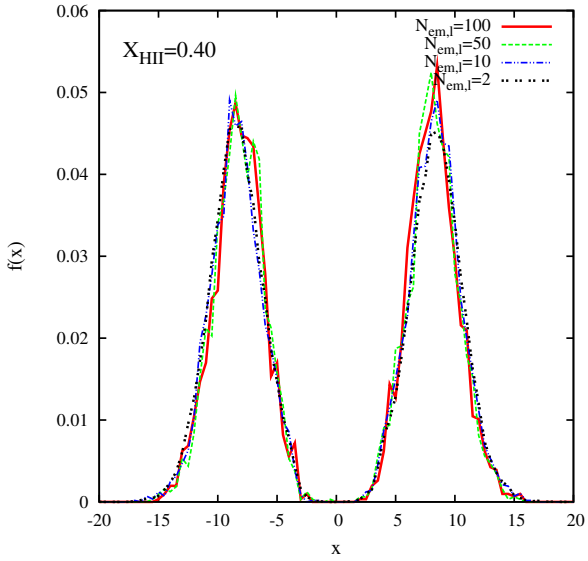
X_HII=0.40
N_em,I=100
N_em,I=50
N_em,I=10
N_em,I=2
f(x)
x

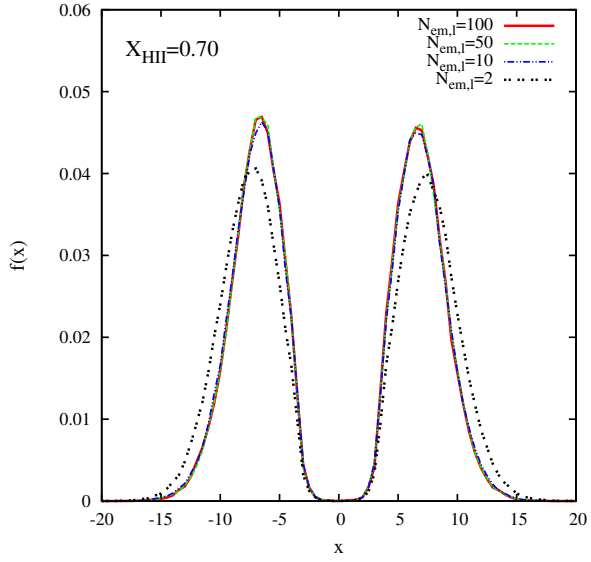
X_HII=0.70
N_em,I=100
N_em,I=50
N_em,I=10
N_em,I=2
f(x)
x

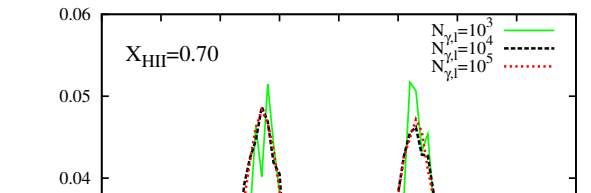
X_HII=0.70
N_γ,I=10^3
N_γ,I=10^4
N_γ,I=10^5

3.5 Dependence on input parameters

In this Section I investigate the dependence of the final spectra on the parameters $N_{em,l}$, $N_{\gamma,l}$ and N_{out} defined in Sections 2.3.1 and 2.3.3. The convergence tests presented are performed by adopting the same conditions of the static case (see Sec.3.1).

First I compare spectra built by integrating over the full simulation time, i.e. I set $N_{out} = 1$. I have done several runs varying the number of Lyα emissions ($N_{em,l} = 2, 10, 50, 100$) and setting $N_{\gamma,l} = 10^4$. Lyα photon packets are emitted according to equation 2.23, i.e. at regular ionization intervals. For $N_{em,l} = 2$, the two emissions are performed at the beginning and once the ionization degree has become stationary. The results are shown in the top-left panel of Figure 3.4. From an inspection of the Figure it is clear that 2 emissions are not accurate enough to properly describe the emergent Lyα spectrum. This is a consequence of the method described in Section 3.1 for weighting the contribution to the spectrum from photon packets emitted at different steps. In fact, as the time between the two emissions is large, the weight assigned to the photon packets of the second (and last) emission is so large that the contribution from the photon packets of the first emission is negligible. Moreover, at the time of the second emission ionization is almost complete and as a consequence the spectrum has two thin peaks very close to the central frequency and shows no large frequency shift due to scattering in a gas with larger opacity. So, in this case the outcoming spectrum is the result of Lyα transfer in an almost ionized sphere and the stages through which the gas reached such configuration are completely neglected. As the number of emissions is increased, the accuracy improves and convergence is reached when $N_{em,l} > 50$.

I have then checked convergence of instantaneous (vs integrated) spectra, setting $N_{out} = 10$ and performing again four runs with different numbers of Lyα emissions ($N_{em,l} = 2, 10, 50$ and 100) and $N_{\gamma,l} = 10^4$. Figure 3.4 displays two sets of spectra, each corresponding to a fixed $\chi_{\rm HII}$ value: 0.4 (top-right panel) and 0.7 (bottom-left panel). Effectively, the spectrum corresponding to $N_{em,l} = 2$ is built only with photon packets from the first emission, as the second is performed when $\chi_{\rm HII} > 0.7$. At $\chi_{\rm HII} = 0.4$ the spectra are all very similar because the gas opacity is sufficiently high to trap Lyα photon packets and those emitted close to the time when the spectrum is built are still scattering in the gas. On the contrary, as ionization proceeds, photon packets emitted at later

times encounter less neutral hydrogen and escape more easily, and their contribution to the outcoming spectrum increases. As a consequence, the case with $N_{em,l} = 2$, when Lyα photon packets have been emitted only at the beginning of the simulation, displays a broader and more shifted profile.

Finally, I use different values of $N_{\gamma,l} = 10^3, 10^4, 10^5$, with $N_{em,l} = 100$ and $N_{out} = 50$, to determine the smallest number of Lyα photon packets needed in each emission in order to achieve convergence. In the bottom-right plot I show Lyα profiles corresponding to an ionization fraction of $\chi_{\rm HII} = 0.7$. As expected, the increasing number of Lyα photon packets in every emission produces a smoother profile. I find that, for the configuration considered, the emissions characterized by 10^3 photon packets are not accurate enough, and at least 10^4 photon packets per emission are needed.

Chapter 4

New features and realistic test application

In this chapter I discuss some important new features implemented in the code and additional tests performed on a simulated galaxy at redshift $z \sim 10$. The main goal of this chapter is to show the ability of the code to determine the variations of the Lyα radiation field while the gas in which it propagates is affected by the ionizing radiation emitted by the stars within the galaxy. The Lyα radiation is generated by both stars and recombining ionized gas.

The chapter is structured as follows. Section 4.1 is dedicated to a brief description of the simulation which has been used for the tests. In Section **??** I discuss the new features of `CRASH`α . The tests on the simulated galaxy and the analysis are in Section 4.3.

4.1 Simulation

As mentioned in the Introduction, I perform the tests on a simulated galaxy at z=10. For this purpose I use the outputs from the simulations described in Scannapieco et al. (2008). These are a set of hydrodynamic simulations designed to study the formation of galaxies using different formation histories. The simulations follow the evolution of matter from $z = 127$ to $z = 0$ in a ΛCDM Universe with the following cosmological parameters: $\Omega_\Lambda = 0.75$, $\Omega_\mathrm{m} = 0.25$, $\Omega_\mathrm{b} = 0.04$, $\sigma_8 = 0.9$ and $H_0 = 73$ km s^{-1} Mpc^{-1}, where the symbols have their usual meaning. In this work I use the simulated galaxy labelled as Aq-C-5. At $z = 0$ the galaxy's virial radius is ~ 237 kpc and the mass contained within it is $\sim 1.6 \cdot 10^{12}$ M$_\odot$. I refer the reader to the original paper for more details.

For my purposes, I use a snapshot of the galaxy at $z \sim 10$. The physical characteristics

of the snapshot need to be gridded before being used as input by CRASHα. In fact, since the code is designed within the context of a uniform Cartesian grid, the gas represented by SPH particles will first have to be distributed into cells to retrieve the properties of the field. More in particular, I need the gas total number density, velocity and temperature, the position of the stellar sources and their luminosity. Here I use a $N_c^3 = 128^3$ grid, which corresponds to a resolution of 0.5 physical kpc. I properly distribute the properties from the particles into cells by using the smoothing kernel associated with the SPH particles. Scannapieco et al. (2008), in their simulation, define a gas particle as eligible for star formation, if this is denser than the critical value $7 \cdot 10^{-26}$ g cm^{-3} and if it lies in a convergent flow. Under these conditions, they generate a new star particle using a stochastic approach on the eligible particles. The star particles have a Salpeter initial mass function (IMF) with lower and upper mass cut-off of 0.1 and 40 M$_\odot$ (see Scannapieco et al. 2005, for details on the implementation of star formation).

The gridding process reduces the original SPH simulation resolution so that it may be that several sources fall in a same cell. After (before) gridding, I have 2829 (11586) sources. To each source I assign a spectrum synthesized with STARBURST99[1]. In particular I used an instantaneous star formation with a single Salpeter-type IMF. The metallicity parameter was set to the minimum value available 0.001, which is the closest to the average metallicity of the galaxy (the actual value is ~ 0.0013). The amplitude of the spectrum assigned to each source is then normalized with the source's luminosity.

In Figure 4.1 I show two slices of ~ 10 comoving kpc of thickness, cut through the simulation box. The plots refer to the density field in the x-y and y-z planes. The stellar sources are illustrated as white dots and, as expected, are concentrated in the highest density regions.

To be able to treat the propagation of the Lyα radiation emitted by the sources more accurately than in the test cases discussed in the previous chapter 2, I have implemented in CRASHα new features, which I am going to describe in the following sections.

Please note that the Lyα radiation field is discretized in a number of Lyα photon packets. This is a statistical description in which the properties associated to the ensamble Lyα photon packets emitted (e.g. frequency, position and direction) reproduce the physical properties of the Lyα radiation.

[1] http://www.stsci.edu/science/starburst99

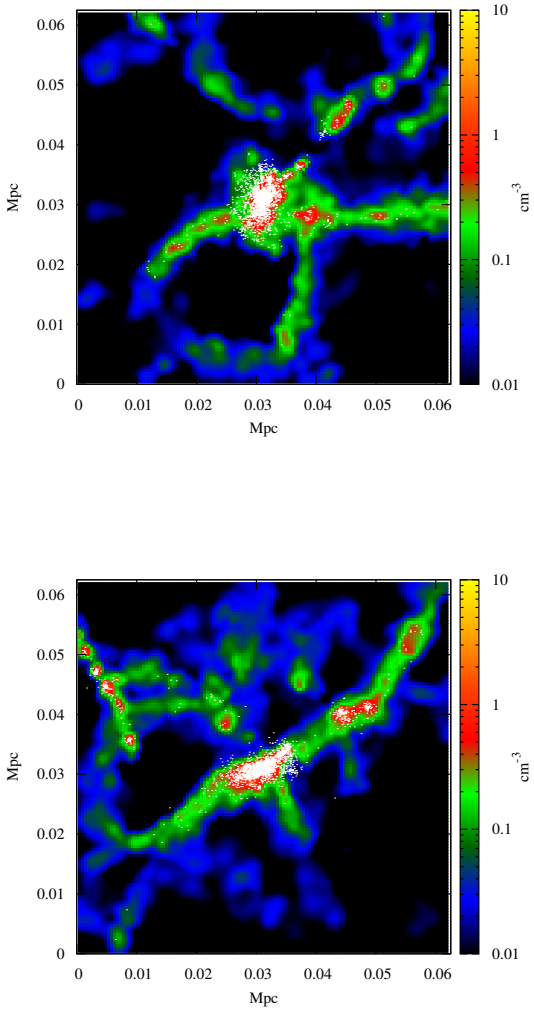

Figure 4.1: Number density maps of the galaxy at $z \sim 10$ (see text for details). The slices are ~ 10 comoving kpc of thickness. The plots refer to the x-y (left panel) and y-z (right) planes. The stellar sources are illustrated as white dots.

4.2 Emission of Lyα photons

Typically, the sources within a simulation box span a wide range of luminosities. In such a case emitting the same number of Lyα photon packets for each source will not efficiently sample the overall radiation field in the simulation box. This would in fact result in a coarse sampling of the energy emitted by the most luminous sources, which dominate the radiation field, while unnecessarily oversampling the less relevant contribution from the faintest sources.

To overcome this problem, I introduce the use of a characteristic Lyα luminosity per unit photon packet, $\mathcal{L}_{Lya}$, defined as

$$\mathcal{L}_{Lya} = \frac{\sum_i L_i}{n_s \cdot \bar{N}_{Lya}} = \frac{\bar{L}}{\bar{N}_{Lya}}, \tag{4.1}$$

where L_i is the luminosity of the i-th source, n_s is the total number of sources, $\bar{L} = \sum_i L_i/n_s$ is the mean luminosity and $\bar{N}_{Lya}$ is the number of Lyα photon packets emitted by a source with the mean luminosity. I then determine the number of Lyα photon packets emitted by the i-th source as:

$$N_{Lya,i} = L_i/\mathcal{L}_{Lya}. \tag{4.2}$$

In other words, once the mean luminosity $\bar{L}$ and the number of photon packets $\bar{N}_{Lya}$ emitted by a source with such luminosity have been defined, each source will emit a number of photon packets proportional to its luminosity, as calculated in eq. 4.2, and the energy carried by each photon packet is constant independently from the source from which the packet was emitted (but see below). This assures that the most luminous sources emit more photon packets than the fainter ones, and thus a better sampling of the emission from the most relevant sources and, at the same time, a lower computational cost for the treatment of the smaller sources.

In order to avoid undersampling for any of the sources considered, I further impose that each source emits a minimum number of photon packets, i.e. $N_{Lya,i} = min\{N_{Lya,i}, N_{min}\}$ where N_{min} is a parameter whose value is assigned according to the type of problem at hand and the required resolution. The number of photon packets emitted by a source determines the sampling resolution of that sources.

Each photon packet emitted by the i-th source has a corresponding energy:

$$\mathcal{E}_{ph,i} = \frac{\Delta t \cdot L_i}{N_{Lya,i}} = \Delta t \cdot \mathcal{L}_{Lya}, \tag{4.3}$$

where Δt is the time elapsed between two emissions of Lyα photon packets. It should be noted that the second equality is strictly valid only for those sources for which $N_{Lya,i} > N_{min}$ and that for these sources $\mathcal{E}_{ph,i}$ is a constant value, while for sources with $N_{Lya,i} = N_{min}$ it varies with the source's luminosity.

4.2.1 Diffuse Lyα photons

The recombination of an ionized H atom is followed by the emission of a photon whose energy is the sum of the electron kinetic energy and the binding energy of the level at which the electron recombines. If the electron recombines directly to the ground level, the photon will be emitted in the neutral hydrogen ionizing continuum. Recombination to higher levels will instead lead to the emission of a continuum photon with energy $h\nu < 13.6$ eV, followed by a cascade of line photons produced in the de-excitation process. In the `CRASH` implementation, the effect of the diffuse ionizing radiation emitted by the recombining gas is self-consistently taken into account as described in details in Maselli, Ferrara & Ciardi (2003). Briefly, in analogy with the direct one, the diffuse radiation field is discretized into photon packets. The allocates a 3D array, N_{rec}, composed of N_c^3 elements (one for each cell of the cartesian grid), which keeps track of the number of recombination events occurring in the corresponding cell. If in the cell with coordinates (x, y, z), $N_{rec}(x, y, z)$ is larger than a given threshold, a packet containing $N_{rec}(x, y, z)$ photons is emitted from the cell and $N_{rec}(x, y, z)$ is set to zero. The fraction of photons going into ionizing radiation is calculated based on the probability of recombination at the ground level and its frequency is estimated based on eq. 4.4 below. As the diffuse radiation is isotropic, the packet propagation direction is randomly selected. If recombinations occur to the ground state and Local Thermodynamic Equilibrium (LTE) is assumed, the emissivity of the diffuse radiation, $\eta(\nu)$, results in the following frequency dependence (Mihalas 1978; Osterbrok 1989):

$$\eta(\nu) \propto \sigma(\nu) e^{-(h\nu - h\nu_{th})/k_B T} \qquad \nu \geqslant \nu_{th}, \tag{4.4}$$

known as Milne spectrum. Here, $\sigma(\nu)$ and $h\nu_{th}$ are the photoionization cross-section and the ionization potential of neutral hydrogen, respectively; k_B is the Boltzmann constant

and T is the kinetic temperature of the recombining electrons. It is assumed that all photons of a packet recombine to the same atomic level. If recombinations do not occur to the ground level, the probability of recombinations at different levels must be evaluated and if recombination occurs to the ground level I sample the spectrum in eq. 4.4 (appropriately normalized).

As it is computationally unfeasible to calculate this re-emitted radiation at each timestep of the simulation for each cell, the condition for re-emission is evaluated at fixed time intervals.

In the standard CRASH implementation, only recombinations at the ground level (i.e. the photons re-emitted in the ionizing continuum) are considered. In CRASHα I add a new implementation which takes care also of the production of Lyα photons. In an optically thick case, when most of recombinations are expected to happen, about 65% of recombinations lead to the emission of a Lyα photon (Cantalupo et al. 2005, Tasitsiomi 2006). As the fraction of recombinations is a weak function of the gas temperature (e.g. Osterbrock 1989), in CRASHα the above value is assumed as a constant value.

Analogously to the CRASH implementation, in CRASHα when $N_{rec}(x, y, z)$ is larger than the given threshold, together with the emission of continuum photons as described above, The code emits $N_{rec}(x, y, z) \times 0.65$ Lyα photons. In order to have Lyα photon packets with an energy similar to the one of the packets emitted directly from point sources, the code distributes such number of Lyα photons in $N_{rec,Lya}(x, y, z)$ packets and emits each of them in a random propagation direction. The value of $N_{rec,Lya}(x, y, z)$ is given by:

$$N_{rec,Lya}(x, y, z) = N_{rec}(x, y, z) \cdot 0.65 \frac{\varepsilon_{ly\alpha}}{\Delta t \cdot \mathcal{L}_{Lya}}, \tag{4.5}$$

where $\varepsilon_{ly\alpha}$ is the energy corresponding to a Lyα photon, Δt and $\mathcal{L}_{Lya}$ have been defined in eqs. 4.3 and 4.1,respectively. These Lyα photon packets have a corresponding energy as described in eq. 4.3.

4.2.2 Treatment of dust

As the presence of dust in the gas can deeply affect the emerging Lyα spectrum, I have extended the CRASHα implementation to account for the role played by dust in shaping the characteristics of the Lyα radiation. This is done following the prescription described in Verhamme et al. (2006). When a Lyα photon interacts with a grain of dust it can be

either scattered or absorbed. Although for certain particular gas/dust configurations the presence of dust can amplify the intensity of the emergent Lyα radiation (e.g. Neufeld 1991; Tasitsiomi 2005), in an environment where Lyα photons undergo a large number of scatterings, absorption is typically more prominent. This can be easily understood from the following simple argument. Assuming that the probability for a photon to be scattered by a dust grain is the same as the probability to be absorbed, after 20 photon-dust interactions, statistically, only one photon in 10^6 is not absorbed. Under these assumptions, I consider the effects of dust scattering negligible, but I still process the absorption in order to describe the damping effects on the final spectrum. In the following I describe in more details the implementation of dust.

I define the dust cross section, σ_d, as:

$$\sigma_d = \pi d^2; \tag{4.6}$$

where d is the typical dust grain size. Assuming that the dust grain number density, n_d, is proportional to the neutral hydrogen number density[2], n_H, I can write:

$$n_d = f_{H-d} \left(n_H \cdot \frac{m_H}{m_d} \right), \tag{4.7}$$

where m_H and m_d are the mass of an H atom and of a dust grain, respectively, while f_{H-d} is a parameter introduced to quantify the proportionality. Throughout this chapter I assume the following values for the dust implementation: $d = 10^{-6}$ cm, $m_H/m_d = 5 \cdot 10^{-8}$ and $f_{H-d} = 5 \cdot 10^{-3}$ (Verhamme et al., 2006). The above parameters are degenerate for the estimate of the optical depth. For convenience I introduce the parameter $\alpha_{dust} = \left(d^2 \cdot f_{H-d}\right)/m_d$, which encapsulates the degenerate dependence on the various parameters above, given specific dust characteristics. The dust optical depth, for a travelling photon packet k, can then be expressed as:

$$\tau_{dust}^k = \alpha_{dust} \pi m_H \sum_j n_{j,H} l_j, \tag{4.8}$$

where $n_{j,H}$ and $l_j = t_{scatt}/c$ are the H number density and the path travelled by the photon packet in cell j, respectively, while c is the speed of light and t_{scatt} is the time interval that the photon packet is expected to spend inside the cell due to scattering (see the appendix A.1 for details on the calculation of t_{scatt}). The sum is performed over all

[2] A more realistic assumption would be to assume that the dust follows the distribution of metals. As metals are not relevant to my discussion in any other respect, I neglect their presence and follow the prescription described in the text.

the cells encountered by the photon packet and τ^k_{dust} is updated on the fly any time a cell is crossed. When the photon packet escapes from the simulation box, τ^k_{dust} is stored together with its other properties (the last crossed cell, the photon packet frequency, the cell's temperature, the photon packet escaping direction, the simulation time, the photon packet corresponding energy and the emission source; see chapter 2 for details). Its value is then used to calculate the energy associated with the photon packets escaped from the box as $\mathcal{E}_{ph,i} \cdot e^{-\tau^k_{dust}}$, where $\mathcal{E}_{ph,i}$ is given in eq. 4.3. From the above expression it is clear how the value of α_{dust}, which defines the model adopted for the dust, determines the outcoming spectrum's intensity. As the depletion of energy due to the presence of dust is calculated as a post-process at the end of the simulation, it can also be renormalized for different values of α_{dust}, i.e. for different dust models. A correct evaluation of τ^k_{dust} ensures a precise determination of the spectral features as determined by the presence of dust. In fact, the energy associated with each photon packet is depleted by a different amount, depending on the density encountered along the path and the distance travelled by the packet.

It should be noticed that dust affects also the propagation of the ionizing radiation by absorbing the UV photons. If absorption by dust is significant, the evolution in the ionization field is slower and, as a consequence, the Lyα radiation is confined in a smaller region. In this thesis I neglect the effect of dust on the ionization field and defer its proper treatment to a future work.

4.3 Tests

In this section I present some results obtained from the application of CRASHα to the simulation described in Section 4.1. For the tests described in this chapter (unless otherwise stated), I adopt the following parameters (for a detailed description of the parameters refer to chapter 3). The simulation's duration is $t_{sim} = 10^7$ yrs, which is divided into 10 time intervals of 10^6 yrs each. The number of Lyα photon packets emitted at the same time is 10^5 and for this simulation the code scheduled $N_{em,l} = 100$ emissions. The number of ionizing photon packets emitted per each source is 10^6.

The main goal of this chapter is to show the ability of the code to determine the variations of the Lyα radiation field while the ionizing radiation emitted by stars is shaping

the neutral gas distribution in a realistic configuration. Indeed, these tests should not be regarded as predictions for observations, but rather as an additional analysis of the CRASHα features. In particular I will show that CRASHα , in its current version, allows to:

- study the evolution of the Lyα flux along different directions. As CRASHα allows to take into account anisotropies in the neutral gas, velocity and ionization field, the strength of the radiation emerging from different directions results to be anisotropic and can be accurately determined. This could be accounted for also in chapter 3, but it becomes more relevant when anisotropies are present;

- follow the evolution of the flux at frequencies bluer and redder than the Lyα frequency. The velocity field associated with the neutral gas together with the residual neutral gas distribution are the main causes for the frequency shit experienced by Lyα photons through the Doppler effect. For this reason, a self-consistent treatment of the evolution of the ionization front, which changes the properties of the medium crossed by the Lyα photons, is important because it is also reflected in the relative strength of the blue and red photons. As above, this could be accounted for also in chapter 3, but it becomes more evident when anisotropies are introduced;

- estimate the impact of diffuse Lyα radiation, thanks to the accurate treatement of its emission/progation mechanisms given in CRASHα ; this is a very important feature as, in typical astrophysical conditions, the Lyα spectrum emerging from a given gas configuration is dominated by the diffused radiation;

- evaluate the impact of the dust on the spectral features and intensity of the radiation. Dust, as well as neutral gas, shapes the Lyα spectrum, both in its features and intensity.

In the tests that I have performed for this study, the information about the photons escaped from the simulation box is stored and subsequently analyzed in order to obtain the results in terms of escaping spectra.

In Figure 4.2 the spectrum of Lyα photons emitted by the sources and escaping from the simulation box is shown at two different simulation times, 10^6 yrs and 10^7 yrs, corresponding to a volume averaged ionization fraction of 20% and 95% respectively.

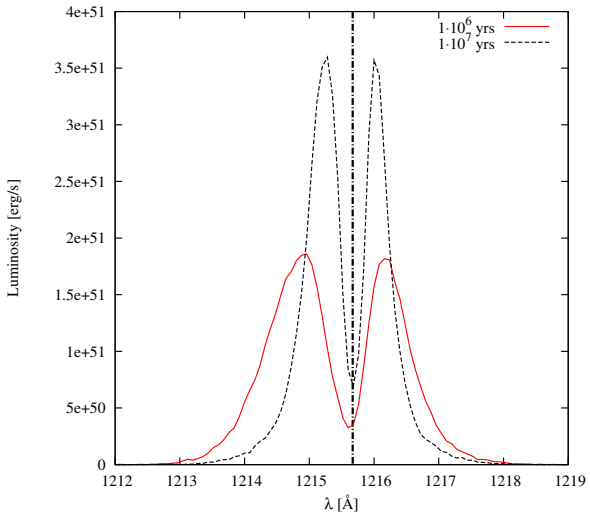

Figure 4.2: Spectrum of the Lyα photons emitted by the sources and escaping from the simulation box at different times. These spectra are obtained integrating the photons escaping in every direction. The wavelength are expressed in the frame of the simulation box. The vertical dashed-dotted line indicates the Lyα wavelength.

These spectra are obtained integrating the photons escaping in every direction. Both spectra exhibit the characteristic feature with two peaks. The irregularities seen in the peaks are associated with the complexity of the neutral gas distribution. Nevertheless, as I am integrating on all directions, the irregularities are less pronounced in comparison with a spectrum obtained integrating only along a preferential direction (see below and Fig. 4.3). As ionization proceeds the intensity of the Lyα radiation increases because of the lower opacity encountered by the photons. The peaks become thinner and less irregular as an effect of the ionization, which makes the neutral gas distribution less complex. The relative strength and width of the peaks depends on the complex velocity field resulting from the simulation. In the first profile, I find the blue peak wider than the red one. This can be explained with a scenario in which the optical depth of the gas collapsing towards the center of the galaxy, where most of the sources are forming, is higher. This is a reasonable situation since collapse is predicted to occur along the filaments of higher density gas. In this case, as the photons are seen Doppler shifted according to the velocity of the atoms, a red photon becomes a line center frequency photon and is easily blocked by the higher optical depth and removed. A blue photon instead has a higher probability of escaping from a collapsing region (Dijkstra et al. 2006, Verhamme et al. 2006). Thus, the higher density infalling gas yields to a wider blue peak because of the higher optical

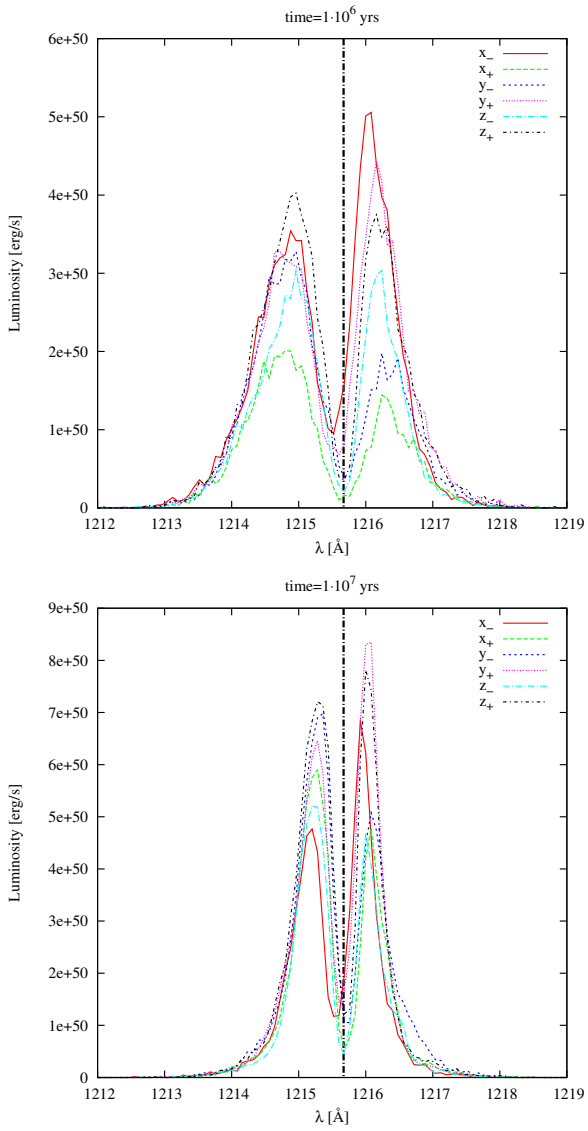

Figure 4.3: Spectra of the Lyα photons emitted by the sources and escaping from the six faces of the simulation box at times 10^6(left) and 10^7(right) yrs. The wavelengths are expressed in the frame of the simulation box. The vertical dashed-dotted line indicates the Lyα wavelength.

depth and the subsequent larger number of scatterings that photons need to undergo before escaping. As the ionization proceeds, the peaks present similar widths and get more symmetric. In fact the sources of ionization are in the highest density regions and the nearby gas is the first to be ionized erasing the differences between the peaks.

In Figure 4.3 I show the spectrum of the radiation escaping from different directions, i.e. the six faces of the simulation box, at two different simulation times. The spectra differ from each other because each of them collects photons which escape the system via different path histories in a dishomogeneous medium. The fact that I detect differences

in the spectra emerging from the various faces reflects the complex structures of the gas density and velocity distributions. It is important to underline that thanks to the joint propagation of the Lyα and continuum radiation, I am able to determine how the variation in the spectral features of the radiation coming out from each face depends on the ionization stage. In fact with different values of the mean ionization fraction I clearly see e.g. how the relative strength of the peaks in one face evolves; this is particularly evident in the z_+ face, in which the blue peak initially dominates over the red peak, while the situation is inverted at the end of the simulation. This can be explained since, as the ionization front goes on, the inner layers of gas, closer to the sources, are ionized and become invisible to the Lyα photons. These photons will instead interact with the gas layers which are further away, beyond the ionization front. If the density and velocity distribution of these outer layers of gas is different from that of the inner layers, the outcoming Lyα spectrum will be different as well, and it will continuously change in time with the ionization front propagation. Similarly, the relative intensity of the radiation escaping from different faces depends on the time at which the object is observed (see for example the radiation escaping from the x_- face is higher than that escaping from the y_- face at earlier times, while at later times the situation is inverted). It is possible to analyze these features only with a parallel propagation of both continuum and line photons. In fact, if the Lyα radiation were treated as a post-process only the final configuration would be considered, missing the temporal evolution, which can be important. As an example, looking at the radiation escaping from the z_+ face at the end of the simulation, one would expect a prominent escape of photons with a wavelength longer than the Lyα . At earlier times though the blue peak was larger. Thus a correct evaluation of the overall escaping photons depends on the detailed temporal evolution of the radiation, which can be evaluated only with a self-consistent treatment of the Lyα and continuum photon radiative transfer.

In Figure 4.4 I present a series of maps showing the distribution of the Lyα photons. In the top-left panel of Figure 4.4 the distribution of the Lyα photons escaping from the top face along the z direction (indicated with z_+ in Fig. 4.3) at a time $5 \cdot 10^6$ yrs is shown. The top-right panel shows the distribution of neutral gas number density, integrated over the last 10 cells from the same face as above. The choice of the last 10 cells is just indicative and representative of the last part of path crossed by the radiation before escaping the

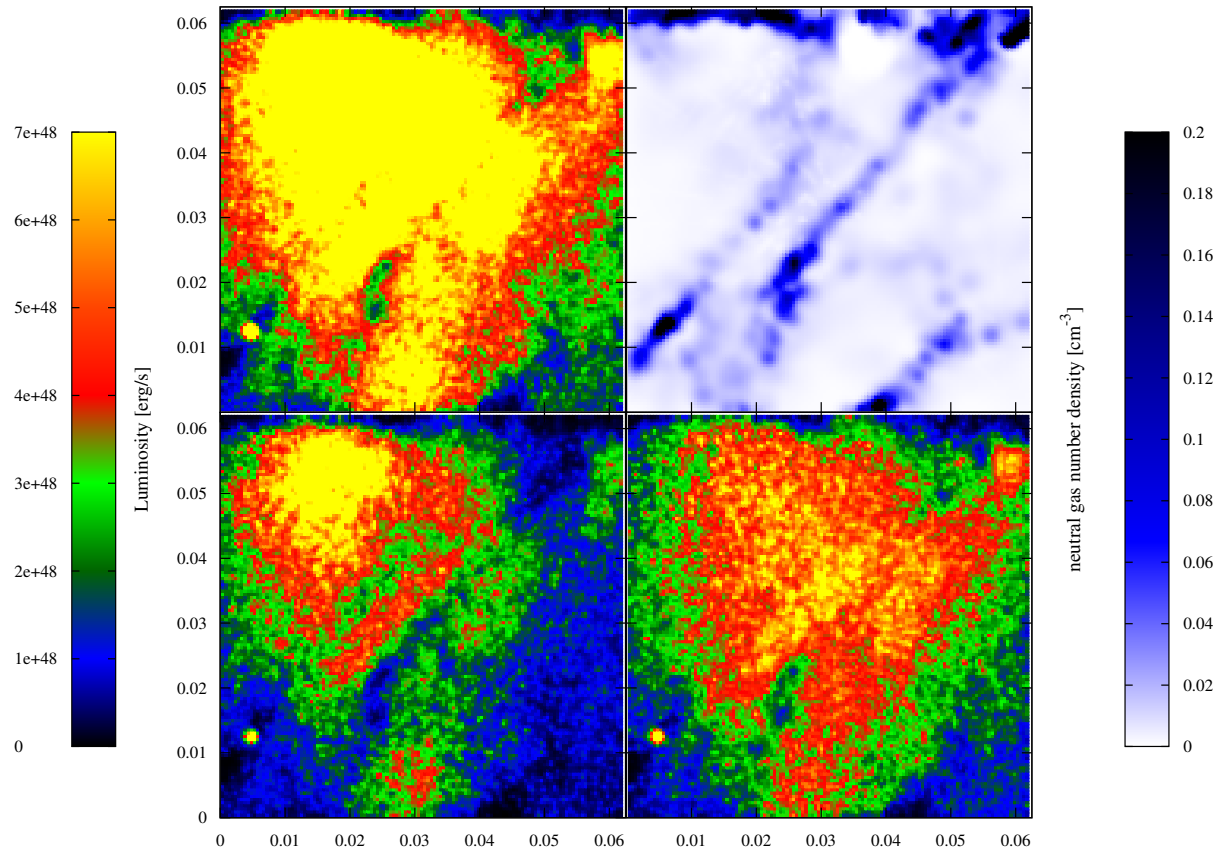

Figure 4.4: **Top-left panel:** distribution of the Lyα photons emerging from the top face along the z direction. **Top-right panel:** neutral gas number density integrated over the last 10 cells from the top face along the z direction. **Bottom-left panel:** distribution of the Lyα photons emerging from the top face along the z direction with a wavelength larger than the Lyα. **Bottom-right panel:** distribution of the Lyα photons emerging from the top face along the z direction with a wavelength smaller than the Lyα. All the panels refer to the time $5 \cdot 10^6$ yrs.

box. The aim of the comparison between the two maps is to show that the stream of the escaping Lyα photons is strongly correlated to the physical state of the gas and its distribution. In fact, the photons preferentially exit the face of the simulation box from highly ionized regions, where scattering events have a low probability. I note that since the propagation of the Lyα radiation is so strongly correlated to a rapidly evolving medium, the ability to follow the Lyα radiation jointly with the ionization evolution is a valuable feature.

In the bottom panels the distribution of the Lyα photons emerging from the same face with a wavelength smaller (right panel) and larger (left panel) than the Lyα is shown. Comparing the panels, it appears that the distribution of the outcoming radiation is very different and that the photon trajectory to escape the box is related to the photon frequency. This could be explained within a scenario in which the blue and red photons are generated or have travelled through regions dynamically different.

It is important to underline once more that the code is able to predict differences in the Lyα flux depending on the gas dynamics and its ionization state, which can be continuously evolving, but can be followed on the fly by `CRASH`α. In fact, the time evolution of the ionization structure determines the paths along which the radiation will preferentially travel before escaping, having consequently an important impact on the properties of the emerging spectra.

4.3.1 Effect of dust

The effect of dust on the spectrum is shown in Figure 4.5, where the emerging spectra, integrated over all the simulation time, for the cases with and without dust are shown. The major effects of dust on the emerging spectrum are *(i)* the average suppression in intensity, and *(ii)* the reshaping of the emergent profile where flux at the external frequencies is suppressed. This is in agreement with the expectations: photons with a higher frequency shift with respect to the line center undergo a larger number of scattering, which implies that they spend more time in the medium or they scatter into regions with high optical depth; their probability to be absorbed by dust grains is then higher. While the amount of luminosity decrement depends on the parameter α_{dust} and is then related to the dust model adopted, the spectral shape is independent from the latter. Indeed, in the scheme, once α_{dust} is fixed, the suppression due to dust absorption for two different Lyα photon

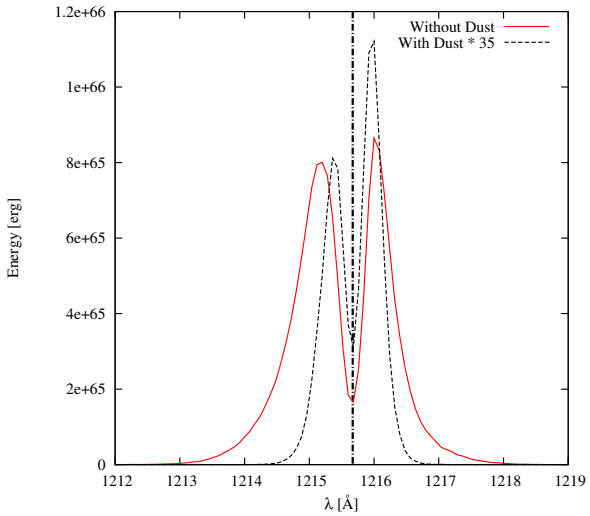

Figure 4.5: Spectrum of the Lyα photons emitted by the sources and escaping from the simulation box and integrated over all the simulation time (10^7 yrs). The dashed (solid) line shows a case with (without) dust. The spectrum with dust is amplified by a factor of 35. The wavelengths are expressed in the frame of the simulation box. The vertical dashed-dotted line indicates the Lyα wavelength.

packets depends on their path lengths and on the amount of hydrogen they cross, which are both independent from α_{dust}. The two photon packets will contribute to the final spectrum according to their absorption and the final spectral shape is linked to the ratio of their residual energy. When the α_{dust} changes this ratio is unmodified.

It is interesting here to underline that the difference in the amplitude of the peaks found for the case with and without dust, has the same origin of the wider peak shown in Figure 4.2: as discussed previously, the wider blue side of the emergent spectrum is associated with infalling high density gas; the same gas is here responsible for the larger suppression from dust.

4.3.2 Effect of diffuse radiation

The effect of diffused radiation is shown in Figure 4.6. Here I compare the spectrum of Lyα primary radiation generated by the stellar sources with the secondary radiation emitted by recombining gas. The latter is produced as described in Sec. 4.2.1 as a consequence of gas photoionized by the ionizing continuum component of the stellar radiation and recombining. The spectra are taken when the simulation time is $5 \cdot 10^6$ yrs, intermediate between those shown in previous plots. The primary radiation spectrum has been multiplied by a factor of 145 for better visibility. As it is well known, the

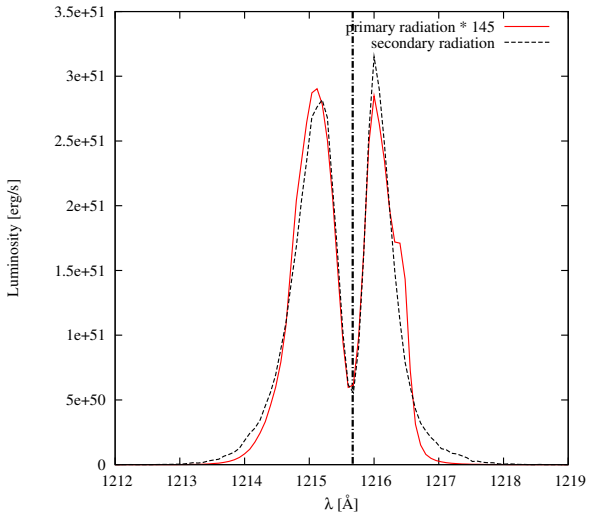

Figure 4.6: Spectrum of Lyα photons generated by the stars (solid line) and those due to diffuse radiation (dashed line). The spectra are escaping from the simulation box at a time $5 \cdot 10^6$ yrs. The spectrum from the stars is amplified by a factor of 145. The wavelengths are expressed in the frame of the simulation box. The vertical dashed-dotted line indicates the Lyα wavelength.

results show clearly that the Lyα luminosity is dominated by photons generated from recombinations and the processed Lyα radiation emitted by the stars has just a marginal effect on the final spectrum. The slight difference in the shape of the external frequencies, i.e. of the wings, can be explained considering the bias in the typical path to escape the simulation box undergone by the two sets of radiation. The photons generated by the stars are typically emitted in highly ionized regions, while the diffused photons are preferentially emitted in overdense regions, where the recombination rate is higher, there is more neutral gas and the path to escape is then characterized by a higher optical depth. The primary spectrum is more irregular because the stars are in much smaller number compared to the ubiquitous production sites of diffused radiation. Furthermore the stars have a wide range in luminosity. Both these factors make the stellar spectrum dominated by isolated objects and by the typical path followed by their photons in order to escape the box. For the diffuse case, the spectrum is smoother due both to the more homogeneous distribution of the emission sites and, as a consequence, to the weaker dependence on the path followed by the photons and the details of the gas distribution. In other words the number of emission sites for the diffused radiation is much larger then the number of stellar sources and they are spread throughout the box, while the stars are typically highly clustered (see Fig. 4.1). As a consequence, the ensemble of secondary photon paths

covers the box more uniformly than in the case of the primary photons; this implies that the dishomogeneities in the neutral gas distribution seen by the secondary photons are washed out more efficiently. In this case there is an evident discontinuity in the red part of the primary radiation spectrum. The analysis of the spectra produced by the single sources indicates that the discontinuity is due to the photons generated by a large stellar source. These photons escape from their local region with a frequency shifted in the red part of the spectrum generating the discontinuity in the primary radiation spectrum.

4.3.3 Effect of ionizing radiation

An important feature of CRASHα is the ability to follow the ionizing front evolution and the Lyα propagation at the same time. In this way, the code is able to simulate a Lyα photon travelling through a continuously evolving medium photoionized by the ionizing continuum component of the stellar radiation in a completely self-consistent way. In order to show the effect of the ionizing radiation on Lyα spectra, I present several tests using the simulated data described in Sec. 4.1.

These tests start with the emission of the ionizing stellar and diffuse radiation until a given time, t_{ion}; then I compare the evolution of two different scenarios. In the first case, at time t_{ion} the code stops the emission of ionizing and diffuse radiation and it emits the Lyα component of the stellar radiation. In the other case the ionizing component is not stopped and the two types of radiation are followed together. In both cases the Lyα radiation is emitted in a single burst at simulation time t_{ion}. I expect to observe two different features in the outcoming Lyα spectra. The first one is a difference in the escaping time and the second one is a difference in the direction of escaping. In particular with the ionizing radiation still propagating I should see a larger amount of Lyα photons escaping with respect to the case in which there is no ionizing radiation. Furthermore when I introduce the ionizing photons in the box, the configuration of the neutral medium is changed and this reflects on the Lyα photons path. We could see this effect as a change in the mean intensity of the escaping flux.

In Figure 4.7 I show the emerging spectra for the two cases above at different stages of the system evolution. Here I show the results of a test using $t_{ion} = 10^6$ yrs. To build the spectra I use the photons escaped from all directions and selected by time. In the left panel the distribution of the photons escaped between the simulation time $t_s = 10^6$

yrs and $t_s = 2 \cdot 10^6$ yrs is shown and in the right panel the same distribution between the simulation time $t_s = 2 \cdot 10^6$ yrs and $t_s = 3 \cdot 10^6$ yrs. The solid lines refer to the case with the simultaneous propagation of continuum and line photons, while the dashed lines refer to the case in which the propagation of the Lyα radiation is followed as a post-process. In the left panel, less photons escape in the post-processing case than in the case in which ionization is included. At a later time though (right panel), the situation is reversed. Moreover, the distribution of photons in the post-processing case is wider. This effect is in agreement with the scenario where the photons are travelling in an unchanged medium and they have to cross a larger fraction of neutral gas respect to the case with ionizing radiation; this difference in the medium condition appears in the spectra as a delay in the escape and a shift in the frequency towards the external spectral region. Another effect, which is due to the presence of ionizing radiation, is the change of the Lyα photon paths. We find differences in the intensity of the radiation escaping from each of the box faces comparing the two cases, arising from differences in the ionization structures. The amount of these diffences is up to 5% of the intensity which exits along each face. To confirm this conclusion, I have performed several runs without ionization and I have estimated that the mean deviation in the intensity escaping along the faces is 10 times smaller. The presence of the ionizing radiation makes some "preferencial paths" for escaping the medium more probable respect to others. This effect is more pronounced when the ionizing radiation is not homogeneous and some regions are ionized faster then others.

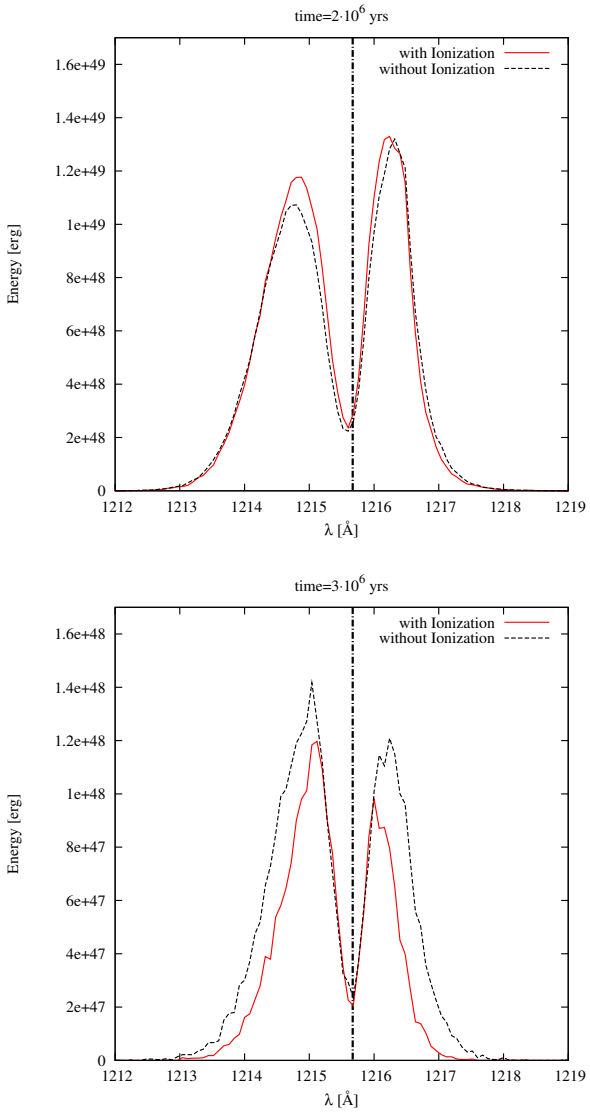

Figure 4.7: In the left panel I compare the spectral distribution of the Lyα photons escaped between time $t_s = 10^6$ and $t_s = 2 \cdot 10^6$. While the right panel shows the distribution of the photons escaped between $t_s = 2 \cdot 10^6$ and $t_s = 3 \cdot 10^6$. The solid lines indicate the case in which the ionization component propagates together with the Lyα photons, while the dashed lines show the case without ionization (see text for details).

Chapter 5

Lyα heating

There has been a great progress over the past several years in our understanding of galaxy evolution and formation. The observational frontier is now shifting to the formation of the first objects, protogalaxies and primordial AGN, which is generally expected to occur some time in the redshift interval $z \sim 6-15$ or so. As the first sources of UV radiation turn on, they reionize the universe, ending the "dark ages" which start at the recombination epoch ($z \sim 1100$). In this cosmic era the universe undergoes a phase transition from being neutral to being mostly ionized (see Fig. 5.1).

Detection of the reionization epoch would thus be a major cosmological milestone. There are a few observational methods for studying reionization: Quasars and the Gunn-Peterson trough, CMB anisotropy and polarization, and 21-cm line from neutral hydrogen (e.g. Gunn and Peterson 1965, Djorgovski et al. 2001, Kaplinghat et al. 2003, Barkana and Loeb 2005). This 21-cm line in particular is of great interest in cosmology because it allows to probe the "dark ages" from recombination to reionization. Including the redshift, this line will be observed at frequencies from 200 MHz to about 9 MHz on Earth. It potentially has two applications. First, a mapping of redshifted 21 centimeter radiation could in principle provide a very precise picture of the matter power spectrum in the period after recombination. Second, it can provide a picture of how the universe was reionized, as neutral hydrogen which has been ionized by radiation from stars or quasars will appear as holes in the 21 centimeter background.

At redshifts $z > 100$, the residual ionization left over from the epoch of recombination (Peebles 1968) keeps the gas kinetic temperature at the CMB temperature, owing to the heating produced by electron scattering of the CMB. Below this redshift the heating source becomes small and the gas temperature drops below the CMB. If the spin temperature

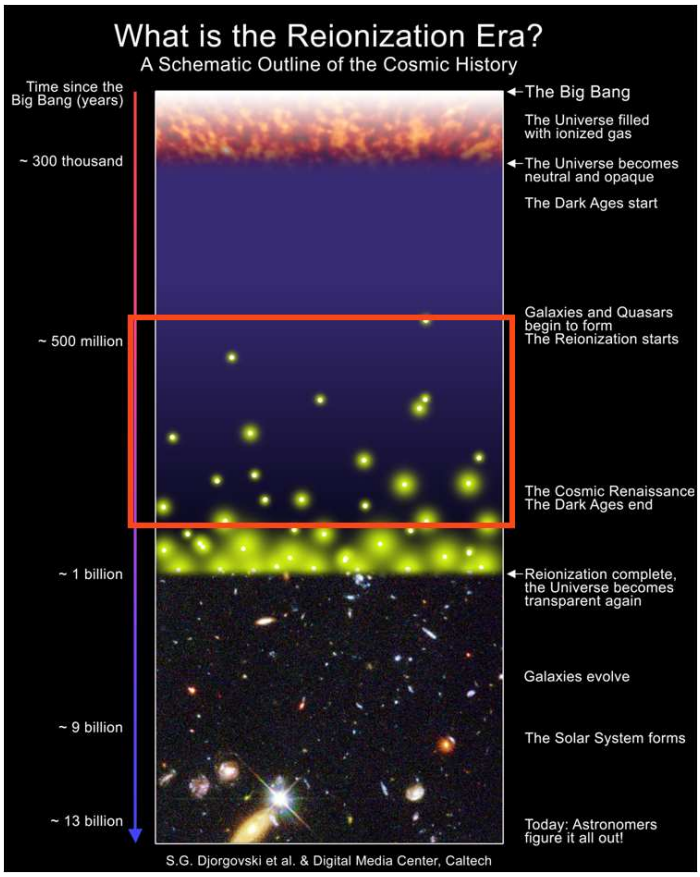

Figure 5.1: Schematic timeline of the universe, depicting reionization's place in cosmic history (red squared).

can be coupled to the kinetic temperature at this stage, the atomic medium would be observed in absorption.

The coupling of the spin and kinetic temperatures can be achieved by collisions with H atoms, electrons and protons, or by scattering of Lyα photons. The coupling due to atomic collisions is small except at very high redshift, where observations of the redshifted 21cm radiation becomes more difficult, or for unrealistically high values of Ω_b (Scott & Rees 1990). A stronger coupling can be induced by Lyα photons, which should be produced as soon as the first stars are formed. The Lyα photons couple the spin and kinetic temperatures by being repeatedly scattered in the gas. The resonance scattering of a photon consists of a transition from $n = 1$ to $n = 2$, followed by the opposite downward transition. This scattering process can change the population of the hyperfine structure levels (Wouthuysen 1952; Field 1958). The probability for a transition back to the ground or excited hyperfine structure states depends on the slope of the radiation spectrum near

the Lyα line center, or the "color temperature". When the radiation spectrum reaches a steady state, this color temperature near the Lyα line center is equal to the gas kinetic temperature, so the Lyα scatterings introduce a thermal coupling between the spin and kinetic temperature. The result of these couplings is that the spin temperature is given by (Field 1958, 1959)

$$T_S = \frac{T_{CMB} + y_\alpha T_k + y_c T_k}{1 + y_\alpha + y_c} \ , \tag{5.1}$$

where

$$y_\alpha \equiv \frac{P_{10} T_*}{A_{10} T_k}; \qquad y_c \equiv \frac{C_{10} T_*}{A_{10} T_k} \ . \tag{5.2}$$

Here, T_k is the kinetic temperature, $T_* = 0.0682$K is the hyperfine energy splitting, $A_{10} = 2.87 \times 10^{-15}\,\mathrm{s}^{-1}$ is the spontaneous emission coefficient of the 21cm line, and $C_{10} = \kappa_{10} n_H$ is the collisional de-excitation rate of the excited hyperfine level. The value of κ_{10} ranges from 2×10^{-14} to $2.5 \times 10^{-10} cm^3\,\mathrm{s}^{-1}$ for T in the range $1 - 1000$ K and was tabulated in Kuhlen, Madau & Montgomery (2006; see also the original papers by Smith 1966; Allison & Dalgarno 1969; Liszt 2001; Zygelman 2005).

The indirect de-excitation rate P_{10} of the hyperfine structure levels is related to the total Lyα scattering rate P_α by $P_{10} = 4P_\alpha/27$ (Field 1958), which is given by $P_\alpha = \int d\nu c\, n_\nu\, \sigma(\nu)$, where n_ν is the number density of photons per unit frequency, and $\sigma(\nu)$ is the cross section for Lyα scattering (Madau, Meiksin, & Rees 1997).
In addition, Lyα photons could be able to heat the IGM temperature above the CMB temperature and render the 21 cm line visible in emission. The advantage of Lya photons over other heating sources, as e.g. x-rays (unless the spectrum is very hard), is that the Lya photons can travel cosmological distances and quickly build up a more homogeneous background.

In this work, I present a code which allows to study the scattering and heating rate due to Lyα photons in the intergalactic medium.

5.1 The Lyα photon scattering and IGM temperature

During the epoch of reionization, UV photons between the Lyα and Ly-limit frequencies are produced in abundance. The scattering of these photons with atoms induce an energy exchange which provides a mechanism for raising or lowering the gas temperature far from any radiation source.

Several authors previously considered this process. Indeed the impact of Lyα photon scattering on the IGM temperature has been investigated in pioneering studies by e.g. Madau, Meiksin & Rees (1997), Chen & Miralda-Escudé (2004), Chuzhoy & Shapiro (2007) and Ciardi & Salvaterra (2007).

Madau et al. (1997) present a new heating mechanism, arising from atomic recoil in response to the scattering of resonant photons. They demonstrate that because of resonant scattering heating, Lyα coupling makes the detection of the IGM in absorption against the CMB quite unlikely, since the same Lyα photons that pump the hyperfine levels heat the atoms as well. This is not entirely surprising, as the energetic demand for raising the kinetic temperature above that of the CMB is relatively small ($\sim 10^{-7} eV/cm^3$ at $z \sim 7$), hence even a relatively inefficient heating mechanism like Lyα resonant scattering may become important. They find that the heating requirements are quite generally met in a variety of scenarios in which radiation sources turn on at high redshift. They show that, in models based on QSO photoionization, and well before the H II region network has fully percolated, the (mostly) neutral IGM between the H II bubbles will be photoelectrically heated to temperatures above a few hundred degrees by soft X-ray photons from the QSOs. In Cold Dark Matter (CDM) models a similar mechanism may efficiently warm the IGM at $z \leqslant 7$, since galactic mass halos with virial temperatures $\sim 10^6$K are significant sources of thermal bremsstrahlung radiation. Alternatively, if protogalaxies at these early epochs are forming stars at a rate which is only $\sim 10\%$ of the global present-day star formation rate, heating by background Lyα "continuum" photons could drive the kinetic temperature of the still neutral material well above the radiation temperature of the microwave background. As a consequence, they conclude that most of the neutral IGM will be available for detection at 21-cm only in emission. So they found accordingly that, if Lyα scattering controls the HI hyperfine level population, as required to produce a 21-cm background distinct from the CMB, recoil heating sufficed to raise T_{IGM} above T_{CMB} and to move the 21-cm background into emission.

Later, Chen & Miralda-Escudé (2004) have calculated the Lyα photon scattering and heating rates in the atomic intergalactic medium, including both redshifted continuum photons emitted between Lyα and Lyβ, and injected photons produced by recombinations or excitations by Lyβ and higher Lyman series photons. They show that the inclusion

of atomic thermal motion (neglected by Madau et al. 1997) in the analysis reduces the heating rate by at least three orders of magnitude. The heating rate of the gas due to the scattering of these Lyα photons is very small and essentially negligible. In the absence of other heating sources, the gas would continue to cool down almost adiabatically while the spin temperature would rapidly drop to nearly the kinetic temperature given a reasonable emission of photons during the reionization epoch. Furthermore, they showed that while photons emitted between Lyα and Lyβ frequencies (called by them "continuum photons") heat the gas when redshifted into Lyα resonance, those injected directly into Lyα by the cascade from higher resonances (called "injected photons") cool the gas. With increasing gas temperature, the efficiency of "continuum photons" as heaters declines, while that of "injected photons" as coolers rises. Therefore, if, as these authors claimed, the numbers of these two types of photons were similar, then the cooling would prevail at temperatures above 10 K. If so, the 21-cm background produced by Lyα pumping would have been in absorption, unless some other mechanism such as photoelectric heating by a strong X-ray background, can raise the IGM temperature above T_{CMB} without fully ionizing it.

However, two important physical mechanisms were missing in previous calculations. The first is the forbidden transition from the 2s to 1s level in hydrogen. This significantly reduces the number of injected photons, raising the transition temperature to about 100 K. The second is the impact of deuterium. Despite its very low abundance, deuterium makes an important contribution to the gas heating by its interaction with Lyα photons. At high radiation intensities, the D Lyα resonance becomes more important for heating the gas than H Lyα . In addition, scatterings by D atoms reduce the number of injected photons for hydrogen, thus decreasing the cooling rate. Chuzhoy & Shapiro (2007) calculate the effect of resonant scattering on H and D atoms, respectively, discussing the impact of this scattering on the thermal evolution, 21-cm signal and reionization history of the IGM. They have shown that, during the reionization epoch, resonance photons can heat the neutral IGM to about 100 K, but not much higher.

Finally, Ciardi & Salvaterra (2007) have calculated the evolution of the IGM temperature, T_{IGM}, induced by Lyα photon heating, assuming that: the gas is in a neutral state, and an escape fraction of ionizing photons of 10%. They find that the Lyα photons produced by the stellar populations considered are able to heat the IGM at $z \sim 25$, although never above ~ 100 K. Lyα heating can affect the subsequent formation

of small mass objects by producing an entropy floor that may limit the amount of gas able to collapse and reduce the gas clumping. They also find that the gas fraction in halos of mass below $\sim 5 \times 10^6$ $M_\odot$ is less than 50% compared to a case without Lyα heating. Finally, Lyα photons heat the IGM temperature above the CMB temperature and render the 21 cm line from neutral hydrogen visible in emission at $z \sim 15$.

5.2 Lyα heating implementation

The relevance of Lyα heating is clear from the discussion in the previous section. I have thus included this feature in the code. In this section I describe the implementation of the computation of the gas temperature variation due to the scattering of Lyα photons.

After an interaction between a photon packet and the gas, the code provides, among others, the frequency variation of the photon. The change in frequency involves an exchange in energy between photon packet and gas. The code uses this exchange to compute the new temperature to assign to the gas cell from where the photon packet has just escaped. When the escaped photon packet frequency is lower than the incoming frequency, the gas gains energy and it will have a higher temperature. On the contrary, when the photon packet escapes bluer than when it got in, the gas will cool because it gives energy to the photon packet to increase its frequency. In this implementation instantaneous termalization of the gas is assumed. In other words, once a given amount of energy is injected in the gas, this reaches a local termic equilibrium on a very short timescale. This happens if there are enough collisions. Using this assumption I define the temperature variation ΔT, for a monoatomic gas, as:

$$\Delta T = \frac{2}{3} \cdot \frac{N_{ph}\ h\ \Delta\nu}{k\ N_{part}}; \tag{5.3}$$

where N_{ph} is the number of Lyα photons in the photon packet, h is the Planck constant, $\Delta\nu$ is the change in frequency, k is the Boltzmann constant and N_{part} is the number of particles in the cell.

Another important assumption concerns how the code treats the Lyα scattering. In fact `CRASH`α is unable to follow every single scatter between gas and photon packets but it uses tables to estimate the total effect of a large amount of scattering in the same cell (as described in previous chapter 2). For the same reason the code can not follow the energy exchange in every single scattering but it uses the difference in frequency given by

the interpolation on the tables in order to change the value of the gas temperature with the total energy exchange. The variation in the temperature cell it calculated after the photon packet escapes the cell. So during the time the photon packet spends scattering inside the cell the temperature does not change. If a photon packet enters a cell in which another photon packet is already scattering, it does not feel the effect of the first photon packet on the gas temperature because the temperature will be modified only when the photon packet will exit the cell. As an example, let's assume that two Lyα photon packets enter in the same cell at t_0 and that the gas temperature in the cell is $T_{cell}(t_0)$. The first photon packet exits the cell at t_1 changing the temperature in $T_{cell}(t_1) = T_{cell}(t_0) + \Delta T_1$. When the second photon packet escapes at t_2, it will change directly $T_{cell}(t_1)$ in $T_{cell}(t_2) = T_{cell}(t_1) + \Delta T_2$. This happens also if the second energy exchange is computed considering $T_{cell}(t_0)$ as gas temperature of the cell where the photon packet was scattering.

Now, let's see the case in which the Lyα photon packet is scattering in the cell and an ionizing packet crosses that cell. This case is already describe in chapter 2. In short, let's consider a Lyα photon packet, with frequency ν_0, which enters a cell a t_0 with gas temperature $T_{cell}(t_0)$. Then, the Lyα photon packet is stopped, at time t_1, and a new frequency will be assigned to it, ν_1. The gas temperature changes to $T_{cell}(t_1) = T_{cell}(t_0) + \Delta T_{ion}$, due to the effect of the continuum radiation on the gas, ΔT_{ion}. Finally, the Lyα photon packet will resume its scattering in the cell where the gas has a new neutral fraction and temperature $T_{cell}(t_1)$. It will scatter until it escapes the cell at t_2 with frequency ν_2. In this case there are two different energy exchanges between Lyα photon packet and gas computed at t_1 and t_2. In the first exchange, the temperature variation, ΔT_1, is computed using eq. 5.3, where $\Delta\nu = \nu_1 - \nu_0$. Considering also Ly$\alpha$ contribution the gas tempeturare at t_1 is $T_{cell}(t_1) = T_{cell}(t_0) + \Delta T_{ion} + \Delta T_1$. After the gas temperature change, the photon packet scattering re-start in the cell and the code computes the last energy exchange at t_2 using eq. 5.3. The temperature variation, ΔT_2, is computed using the difference in the photon packet frequency $\Delta\nu = \nu_2 - \nu_1$. At time t_2, the gas temperature is $T_{cell}(t_2) = T_{cell}(t_1) + \Delta T_2$.

5.3 Tests

In this section I will describe the tests performed on the new features implemented in the code. The goal of these tests is to understand if the code is able to simulate the Lyα heating with enough accuracy and to study the variation in the temperature when the main physical parameters of the simulation are modified.
For these tests I use a reference case, with a fixed set of parameters, and changing one of them in each test I study how the different parameters affect the variation in the temperature.
In the reference case I use a single central source surrounded by completely neutral and uniform gas. The central source has a Lyα luminosity of $L_{ref} = 3{\cdot}10^{49} ph/s$ and no ionizing photons are emitted for these tests; moreover the gas number density is $n_{ref} = 10^{-2} cm^{-3}$ and the initial temperature is $T_{ref} = 10^2 K$. The box size is $l_{ref} = 0.5 Mpc/h$, gridded with 128^3 cells. The simulation is run for a time $t_{sim} = 5 \cdot 10^7 yrs$. In every test there are $N_{em,l} = 100$ Lyα emissions and in each one the energy is divided in 10^4 photon packets. In the reference case the photon packets are generated at the center of the line.

The first test concerns the analysis of the expected variation when the gas has different states of motion.
Since the cross section of Lyα scattering is symmetrical with respect to the center of the line, when the photons scatter with the H atoms with no peculiar motion, they are equally distributed on the red and blue part of the spectrum. This effect has been already discussed in chapter 3 and the spectrum of escaped photons, for this case, shows two symmetrical peaks around the center of the line. When a center line photon is shifted to a higher frequency part of the spectrum it gains energy, cooling the gas. If the photon is shifted toward frequencies smaller than the center of the line, it gives part of its energy to the gas, which will be heated by this photon-gas interaction. Considering these general statements and the final spectrum with two symmetric peaks for a static gas, I expect that the net variation of temperature would be null when there is no peculiar gas motion. In fact the photons which escaping have formed the blue peak, took some energy from the gas, but since the peaks are symmetrical, an equal amount of energy is given back to the gas by the photons in the red peak. Looking at the single cell I expect that some cells will

be randomly cooled and some will be heated. The temperature variation in the single cell will be determined by the local flux of incoming and outcoming photons. Since all the cells are in the same conditions, their cooling or heating must be a random effect with no clear correlation or structure. In fact, if a region shows a clear heating, this means that there is a systematic way to produce more red photons in that specific region, breaking the symmetry of the cross-section. I will show cases where the red photons are favored compared to the blue photons, and the other way round, but with a static and uniform gas there is no physical reason to favor one of the two types of photons.

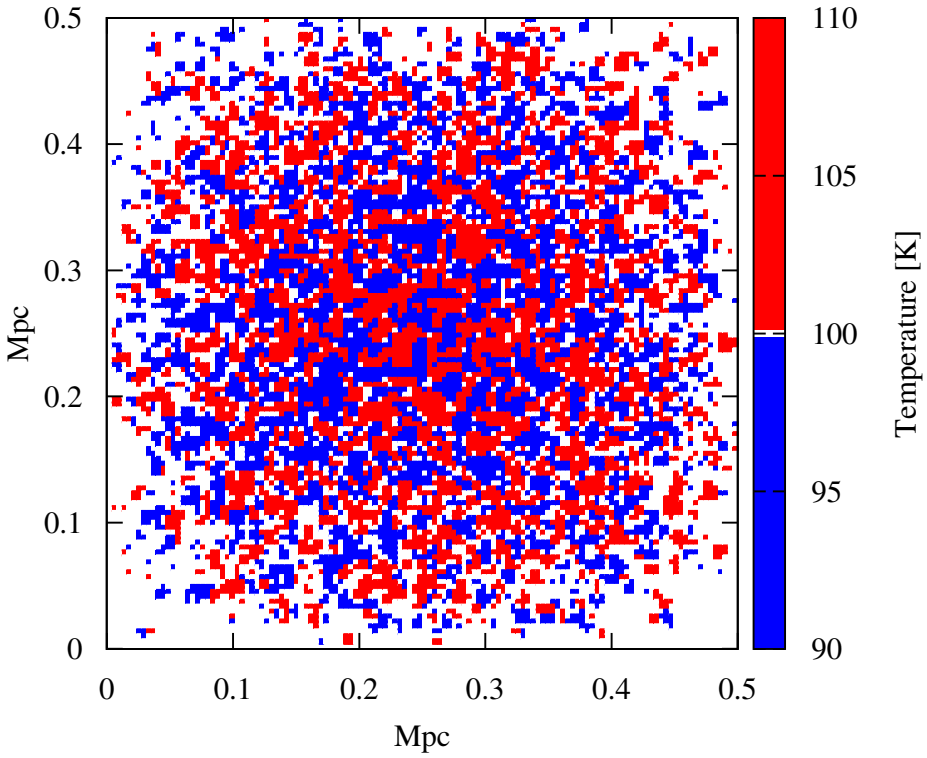

Figure 5.2: Central cut through the simulation box at a time $t_{sim} = 5 \cdot 10^7 yrs$. The blue cells are those with a temperature $T < T_{ref} = 10^2 K$, while the red ones have $T > T_{ref} = 10^2 K$.

In Figure 5.2 a central cut through the simulation box is shown. The blue cells are those which have cooled because more blue photons than red ones have emerged from them, while the red cells are those which have become warmer. As expected, the cell

distribution shows no strong degree of randomness, and no clear sign of structure in the temperature field is present.

Since the cells are at different distances from the central source they are not irradiated by the same flux. In terms of temperature variation, this means that we expect higher absolute values in the temperature variation for the cells which are nearer to the source, while the cells in the peripheral regions should have smaller fluctuations in their temperature.

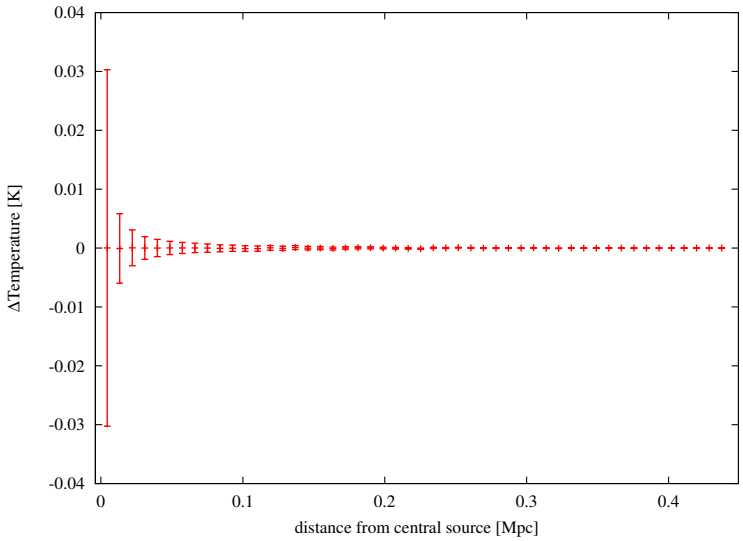

Figure 5.3: Variation of the average temperature in the cells of the test shown in Figure 5.2 versus the distance from the source.

Figure 5.3 shows the variation of the average temperature in the cells against the distance from the source. The error bars are computed with standard deviation on every energy exchange happened in the cells and normalized to the number of cells at the same distance. This plot shows that the net temperature variation, in the static case, is zero and the amplitude of the fluctuation depends strongly by the incoming flux in the cell.

In chapter 3 I showed how the emerging spectrum is affected when the gas has a peculiar velocity field. In particular I considered two cases, one with expanding gas and another with collapsing gas. The spectra in these cases are composed by all blue photons (collapsing gas) or red photons (expanding gas). The reason behind this behavior is the Doppler shift, which makes photons in the wings of the line appear to be photons in the core of the line in the H atom rest frame. In this way the symmetry between red and blue photons is broken and one kind can be scattered more than the other. I expect to

have cooled gas when the emerging spectrum is dominated by blue photons (collapsing gas) and heated gas when in the spectrum there are more red photons (expanding gas).

In Figure 5.4 the central cut through the simulation box is shown for two different test

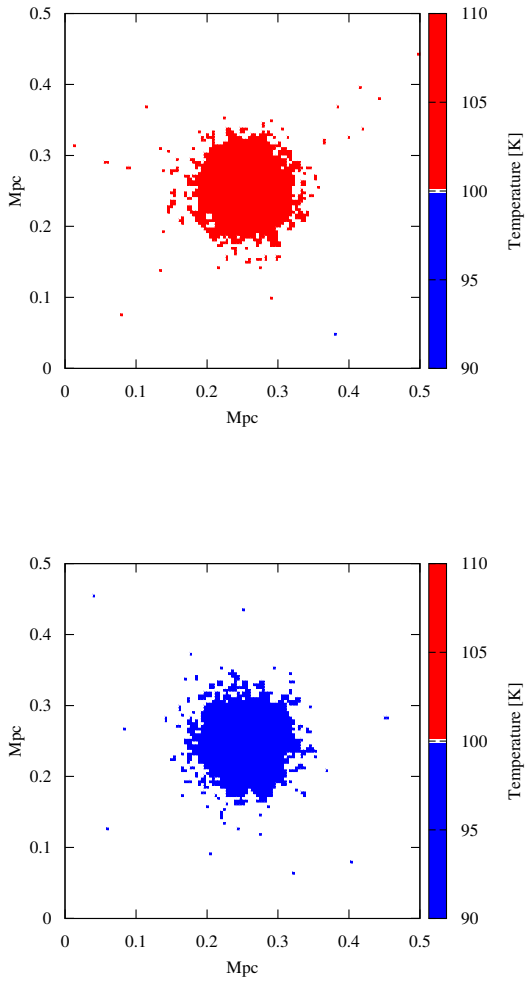

Figure 5.4: Central cut through the simulation box at a time $t_{sim} = 5 \cdot 10^7 yrs$. The blue cells are those with a temperature $T < T_{ref} = 10^2 K$, while the red ones have $T > T_{ref} = 10^2 K$. The panels indicate a case of an expanding (top panel) and a collapsing (bottom panel) gas.

cases. In the top panel I plot the results for the case of an expanding gas, while in the bottom panel the gas is collapsing (the detail of these simulations are shown in the section 5.3.1). As in the previous figure, the red cells are those which have been heated by the scattering with the photons, while the blue ones are those that have been cooled. The temperature variation shows no sign of randomness and a clear structure of heated gas

(top) or cooled gas (bottom), as expected.

In the next set of tests I explore how the temperature variation is affected by changing the most relevant physical parameters. For each simulation of each test case I will show a set of spectra taken at time $t = t_{sim}$. These are the spectra of the radiation emerging from spherical surfaces around the central source with diameter equal to 7.5% of the box linear dimension (red solid line), 15% (green dashed line), 30% (blue 2dot-dashed line) and 75% (pink dotted line). The cyan dot-dashed line shows the spectrum of all the photons escaped from the simulation box. A comparison between the spectra will be an useful tool to analyse the exchange of energy during the photon-gas interaction. To build the spectra, the code keeps track of the photons exiting the spherical surfaces. Since Lyα photons do not travel along a straight line, a lot of photons will likely cross the same surface many times. When this happens, the correct amount of energy is added or substracted from the corresponding spectrum.
Furthermore, for each test I will also show a comparison of the temperature variation.

5.3.1 Gas motion

As a first test, I run some simulations using gas with different spherical velocity fields:

- Linear expansion: $\vec{v}(\vec{r}) = \frac{v_0 \cdot \vec{r}}{r_0}$,
- Constant expansion: $\vec{v}(\vec{r}) = \frac{v_0 \cdot \vec{r}}{|\vec{r}|}$,
- Linear collapse: $\vec{v}(\vec{r}) = \frac{-v_0 \cdot \vec{r}}{r_0}$,
- Constant collapse: $\vec{v}(\vec{r}) = \frac{-v_0 \cdot \vec{r}}{|\vec{r}|}$;

where $v_0 = 300 km/s$ and r_0 is half box size.

Figure 5.5 shows the spectra and the temperature variation for these four cases. The collapse and the expansion case show specular spectra, in fact there is a strong degree of symmetry around the center of the line. The emerging photons in the collapsing case are blue, so the gas should be cooled by the interaction with the radiation. Instead, in the case of expanding gas, the escaping photons' wavelengths are larger than the line center wavelength and the gas has to be heated. The panel with the temperature variation shows that the gas is heated in the expanding case, while there is a cooling when the gas

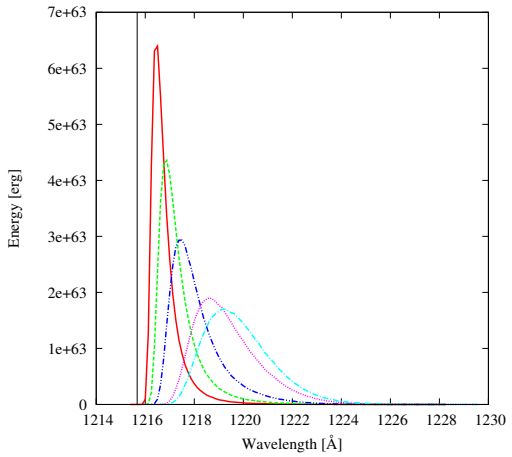

(a) Linear expansion

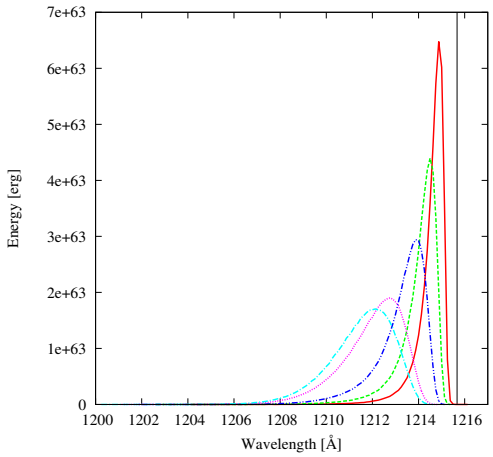

(b) Linear collapse

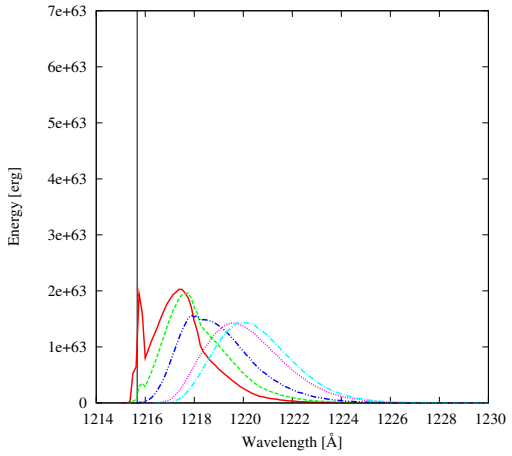

(c) Constant expansion

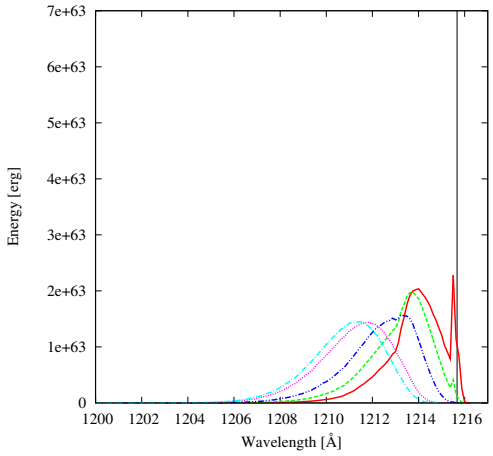

(d) Constant collapse

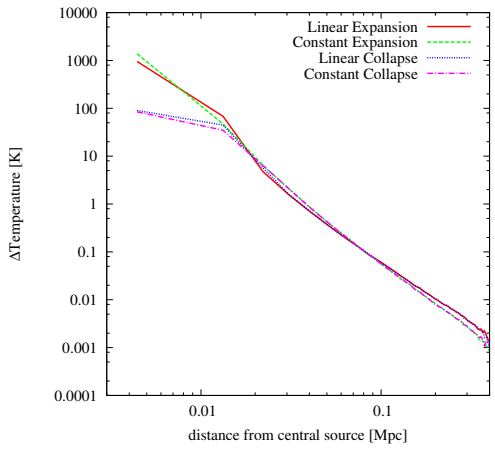

Figure 5.5: Spectra obtained for the test cases, at time $t = t_{sim}$, with a gas which is expanding with a linear (top left panel) and constant (middle left panel) velocity, and with a gas which is collapsing with a linear (top right panel) and constant (middle right panel) velocity. The lines refer to the spectrum emerging from a spherical surface around the central source with diameter equal to 7.5% of the box linear dimension (red solid line), 15% (green dashed line), 30% (blue 2dot-dashed line) and 75% (pink dotted line). The cyan dot-dashed line shows the spectrum of all the photons escaped from the simulation box (see text for details). The bottom plot shows the temperature variation versus the distance from the central source in number of cells. The variation in the case of collapsing gas is shown as an absolute value.

collapses. It should be noted that in this plot the temperature variation for the collapsing case is shown as an absolute value.

Following the code implementation, there is a threshold for the maximum gas cooling; the reason behind this threshold is to have no negative temperature or singularity in other gas properties. The effect of this maximum cooling is well visible in the plot. In the case of collapse, the cooling is saturated to the level of T_{ref}, while in the expanding case the heating is larger than the cooling for the region near the central source. Where the effect of the threshold is less importart, the case of collapse and expansion behave very similarly. For this reason I will analyze just the expansion, keeping the same statements valid for the collapse but considering cooling instead of heating. The cases of linear and constant expansion show very different spectra and a description of these spectra is discussed in chapter 3. For the analysis of the temperature variation it is important to underline the following spectral characteristics. The spectra in the linear expansion case have no photons in the line center. This means that all the photons scatter in the inner regions and they are quickly shifted to different frequencies. Moreover the height of the peak decreases, while the profile becomes wider. In the case of constant expansion there are photons that are still in the line center in the first spectrum considered, but, in the same spectrum, the scattered photons have frequency higher than in the corresponding spectrum of the linear case. Finally the width of the profiles do not change much and the last two spectra are very similar, with only a small shift in frequency.

With this consideration we can understand better the features in the plot of the temperature variation. This set of spectra is useful because, by construction, the temperature variation in the gas delimited by two consecutive spherical surfaces is given by the difference of energy between the spectra emerging from the same surfaces. So the difference between the integrated spectra is used to visualize the expected temperature variation.

It is necessary to underline that in the case with constant velocity, the absolute value of the gas peculiar velocity is higher than in the linear case in the inner region. This allows to have a larger exchange of energy when the photons scatter; on the other hand in the first spectrum of the constant case not all the photons are being scattered like in the linear case. This is a consequence of the Doppler shift due to the higher gas peculiar velocity. In the gas frame most of the photons are seen in the wing of the line and just

a small fraction of photons will be scattered. The above effects are competing and it is typically not possible to say a priori which one dominates. At medium distances all the photons are scattered in the case of constant expansion and the energy of the spectra in this case is larger than in the linear case. In fact, we can see that between $0.02Mpc$ and $0.08Mpc$ the constant case shows a larger temperature variation. Finally, I want to underline that, while in the constant velocity case the emerging spectra eventually keep a constant shape which is only shifted away from the line center by the scatterings, in the linear case also the spectral profile keeps changing and getting wider. So, while in the former case, further from the source, all the photons gain a roughly constant amount of energy, in the latter case the photons with lower frequency have increased their energy by a larger factor. For this reason, the linear case temperature variation is higher than the constant case beyond $0.08Mpc$.

5.3.2 Effect of source's luminosity

In the following tests I use the velocity field of the linear expansion case as reference case. In the next test the luminosity of the central source is modified in order to evaluate the effect on the temperature variation. In particular I run two new simulations where the reference source luminosity is multiplied by a factor of 10, $L_1 = L_{ref} * 10$ (first case), or it is divided by 10, $L_2 = L_{ref}/10$ (second case).

Figure 5.6 shows the spectra for the new simulations and the reference case. In the bottom-right panel, the plot shows how the temperature is affected by the change in luminosity. The spectra are very similar. In fact, the spectra of the new cases are equal to the reference spectra re-scaled by the factor described in the definition of luminosity. The same effect can be seen in the temperature variation plot; the heating in the case with the luminosity L_1 is 10 times larger than the heating in the reference case. In the same way the heating in the case with the luminosity L_2 is 10 times smaller than the heating in the reference case. The plot shows also how in the three cases the temperature variation depends on the source distance in the same way. This test allows to see how the temperature variation depends linearly on the luminosity of the central source.

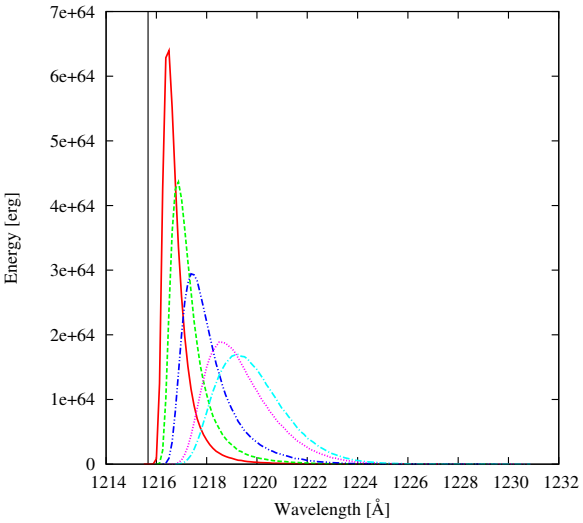

(a) $L_{ref} * 10$

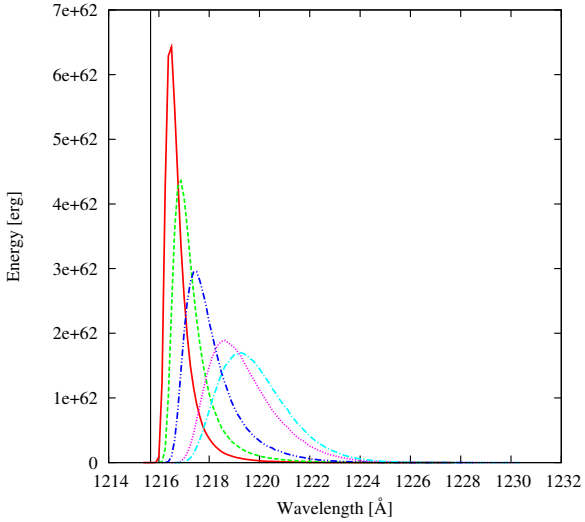

(b) $L_{ref}/10$

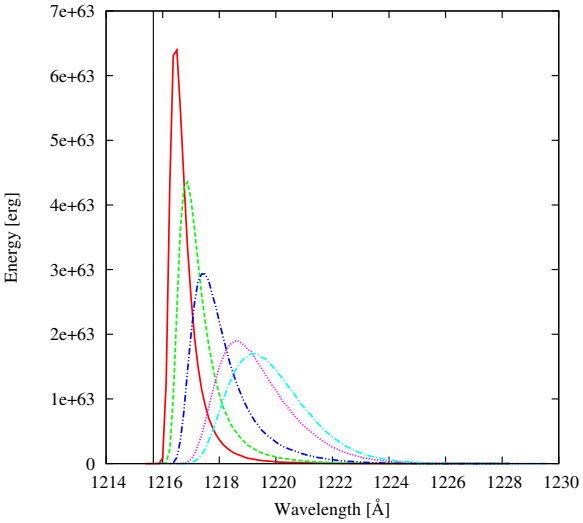

(c) L_{ref}

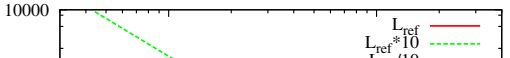

5.3.3 Effect of gas density

The next set of tests is useful to see how the temperature changes using a different gas density. In particular I use two different gas densities to be compared with the reference case. In the first one the density is $n_1 = n_{ref} * 10$ and in the second one the density is $n_2 = n_{ref}/10$.

The results of these tests are shown in Figure 5.7. As in the previous plot, the spectra for the new simulations and for the reference case are compared. Increasing the density makes the gas more optically thick to the Lyα photons. In this way the photons suffer a larger number of scatterings before being able to escape. The effect on the spectra is that the photons have wavelengths with bigger shift respect to the reference case; while with a lower density, the photons find less gas along their travel and because of the fewer scatterings the spectra show a smaller shift in wavelength. Though with bigger shift there is more exchange of energy between radiation and gas, in the case with higher density, the temperature variation (bottom-right) seems to be smaller than in the reference case. This can be explained considering that higher density implies that the energy given by the radiation to the gas, must be shared between a larger number of H atoms than in the reference case. This second effect is dominant compared to the bigger exchange of energy and the final result is that the exchanged energy per single H atom becomes smaller with increasing density. As further prove of this trend, the case with density n_2 shows a larger temperature variation in spite of the smaller shifts in its spectra. In this case the energy is shared between a smaller number of atoms and the effect of heating is larger.

A last consideration arises looking at the last two spectra in the different cases: when I assume higher density, the two last spectra profiles are very similar in shape and the last appears just as a translation of the other; in the reference case the shape is still changing and there is a small translation; while in the case with density n_2 the translation is minimal but the profiles are still different in shape as in the first spectra. The change in shape makes a bigger contribution in term of energy respect to the profile translation; in fact in the plot of the temperature variation the difference, between the case with low density and the reference case, is bigger in the farthest regions from the source respect to the inner region. This can be explained better comparing the case with density n_1 and the reference case, where the increased difference is the consequence of the modification

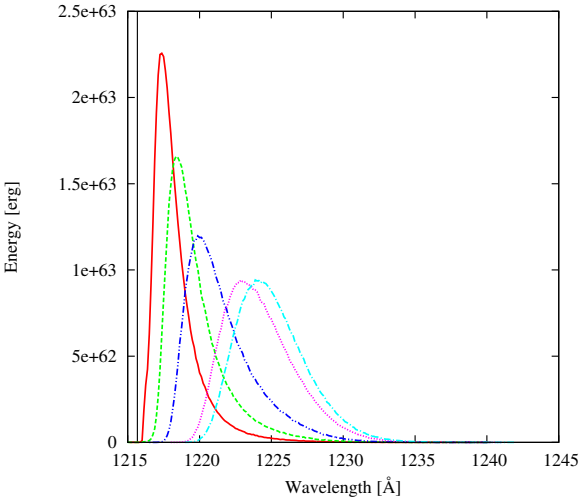

(a) $n_{ref} * 10$

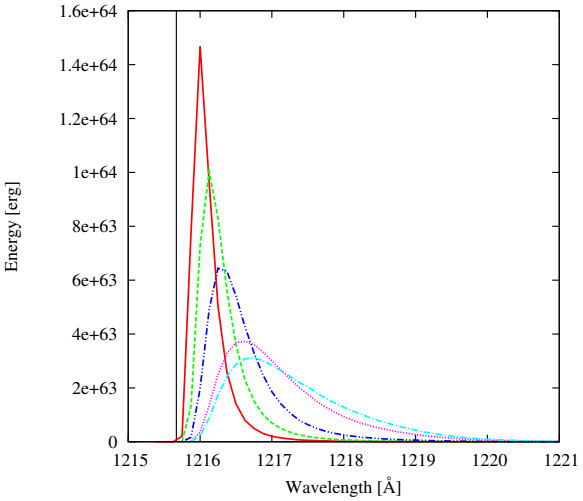

(b) $n_{ref}/10$

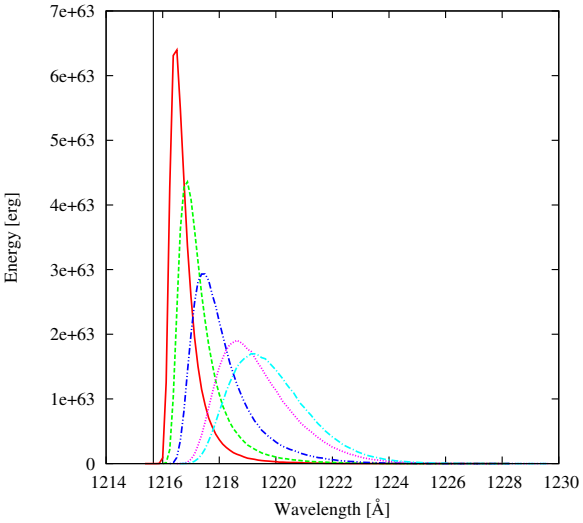

(c) n_{ref}

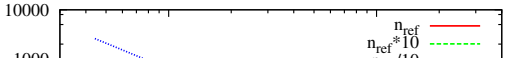

of the last spectra. In the case with low density, this transition is relatively stronger than in the other cases and the temperature variation decreases slowly with distance. In this low density case the photons suffer a smaller number of scatter, so when they are near to the border of the box they are nearer the line center. On the contrary, in the case with high density, the photons are strongly scattered at the beginning of their travel and so they are pushed quickly into the wing of the line.

5.3.4 Effect of gas velocity

In a previous test I explained how the motion of gas modifies the interaction with the Lyα radiation and temperature variation. In this test I want to show the role of the amplitude of that motion in changing the gas temperature.

I still use the expansion case as reference and I assume $v_1 = v_0 * 10$ and $v_2 = v_0/10$ as amplitudes of the velocity fields for the new cases. In Figure 5.8 I show the set of spectra for the new simulations and for the reference case; the last panel is the plot of the temperature variation. Since in all cases there is a motion of expansion, the photons are all in the red part of the spectrum and it is expected to see the gas heated by the energy loss from the radiation. The difference in the spectra is twofold. The first one is that the range of wavelengths reached after the scattering is much larger with a higher value of the velocity. The other difference is in the shape of the spectra's profiles. With velocity v_1, the spectra always peak at the same wavelength, while in the reference case the peak's wavelength moves toward the line's wing. With a lower velocity instead, the shape of the spectra becomes more complex. The photons in the first spectra suffer a lot of scatters, but the velocity is low in the inner regions and the photons remain near the line center. Once the photons reach regions with higher velocity, the spectra change their form drastically; the photons are now all in the red part of the spectrum and they cover a larger range of wavelength. These changes in the spectra induce a lot of fluctuations in the temperature variation. In the case of higher velocities, most of the photons are not shifted after the initial change of frequency; in fact most of them stay around the peak in the profile and only a part of them suffers new scatterings which move them towards outer spectral regions. The heating of the gas is only due to this fraction of photons. The temperature variation for the case with velocity v_2 decreases more regularly and is not

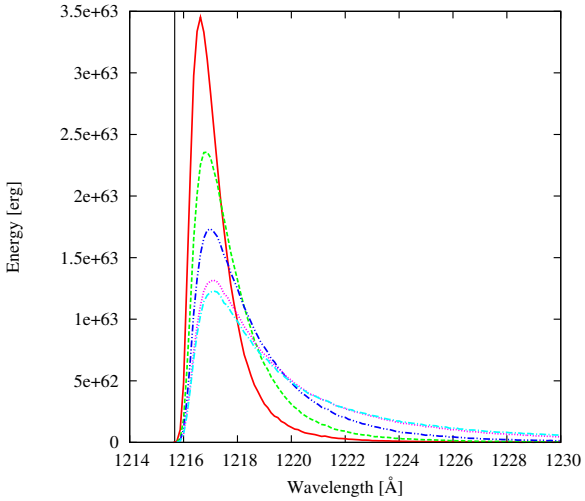

(a) $v_0 * 10$

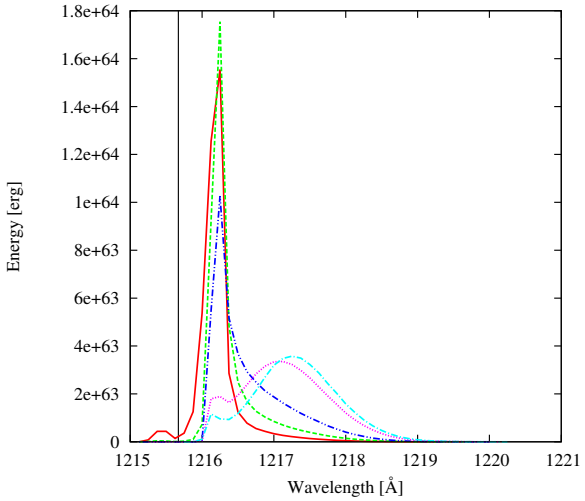

(b) $v_0/10$

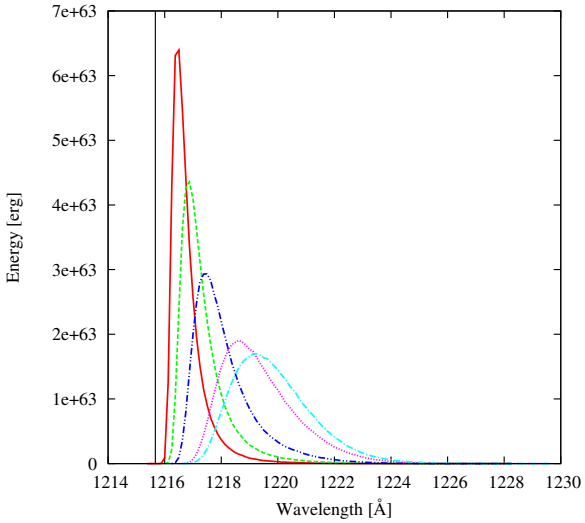

(c) v_0

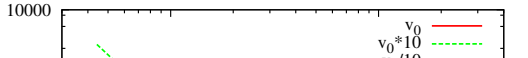

very different from the reference case.

5.3.5 Effect of gas initial temperature

In another test I change the value of the initial gas temperature. In particular I use the values $T_1 = T_{ref} * 10$ and $T_2 = T_{ref}/10$. In Figure 5.9 there are all the set of new spectra and the plot showing the temperature variation. This test is similar, in some way, to the density test. In fact when I use a lower temperature the gas becomes more optically thick to the Lyα photons and when the temperature is higher the gas is more optically thin. In these tests is difficult to get a lot of information from the set of spectra because they seem all very similar, although there are differences between the corresponding profiles. It is possible to analyze the plot of temperature variation keeping in mind the similarity with the density test. In particular when the temperature is higher (gas more optically thin), there is an initial lower heating, but then the temperature variation decreases slowly. When the temperature is lower (gas more optically thick) the photons have been more shifted giving an initial higher heating, but as the distance grows there are less photons available for scattering since they are more shifted; the final effect is a faster decrease of the temperature variation.

5.3.6 Effect of Lyα initial spectrum

In the last test I change the initial Lyα spectrum. In all the previous tests the photons are being injected in the gas at the center of line. For this test I use a flat initial spectrum with a wavelength range of about 52 Angströms around the line center. Figure 5.10 shows the spectra and the temperature variation. As the source luminosity is the same of the reference case, a large fraction of photons is far from the line center with a small probability to be scattered, while in the reference case all the photons are in the line center with a high probability to be scattered. The plot of temperature variation shows this difference; the initial heating in the inner region is much bigger for the reference case, since all the photons exchange energy with the gas. Another difference is that in the reference case the photons that scatter with the gas are all red photons. In the flat spectrum case the photons that scatter are both red and blue photons. Furthermore, the larger the distance

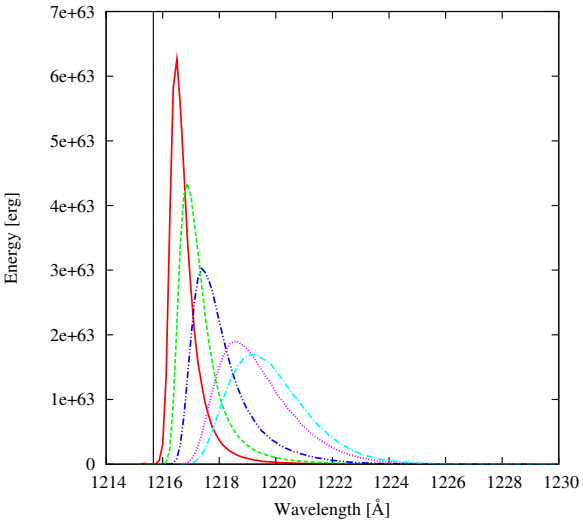

(a) $T_{ref} * 10$

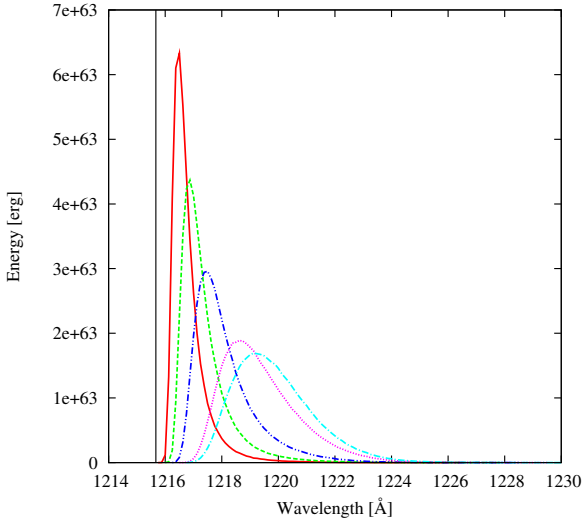

(b) $T_{ref}/10$

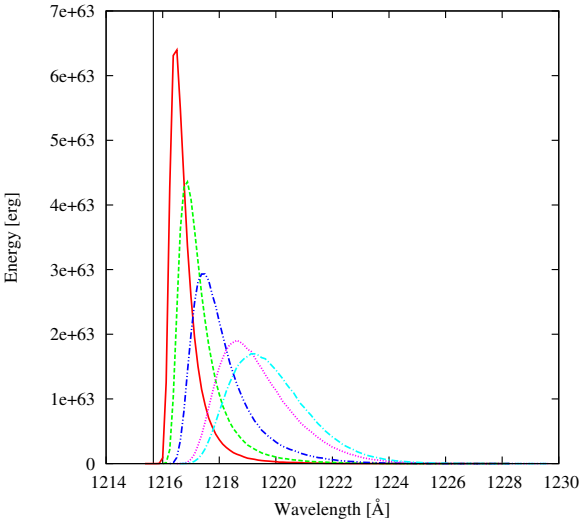

(c) T_{ref}

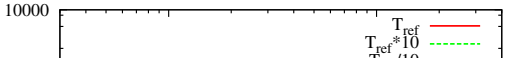

is from the source, the higher is the gas velocity and the larger fraction of blue photons scatter with the gas. In the reference case the peak of the spectra profile shifts toward external spectral regions, but at the same time the amplitude of the peak decreases. In the new case, the peak shift is still visible, but the amplitude grows as more photons begin their scattering. There is a big amount of energy exchanged in these scatterings, since the blue photons become red photons, and the bluer the photons scattered are, the more energy is released into the gas. In the end, the fraction of scattering photons grows with the distance and the energy exchange is bigger. This makes the temperature variation to decrease much slower then the reference case. In fact there is a factor of 100 between the two temperature variations in the inner regions, but at the box boundary the temperature variation for the reference case is just 2 times the flat spectrum temperature variation.

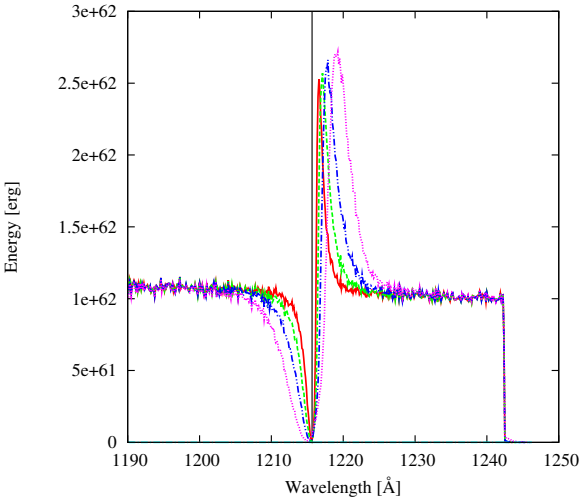

(a) flat

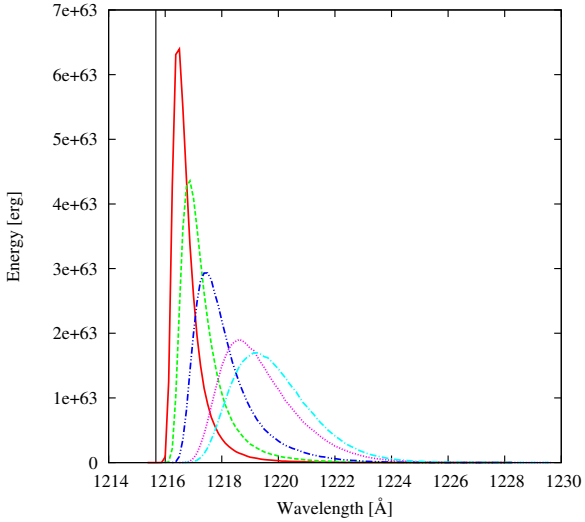

(b) mono

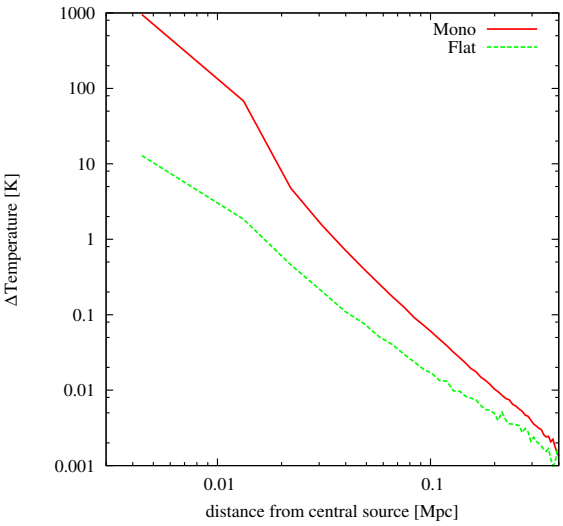

Figure 5.10: Spectra, at time $t = t_{sim}$, with different initial Lyα spectrum. The top left panel show results with flat Lyα spectrum and top right panel with monochromatic Lyα spectrum. The bottom panel shows the temperature variation versus the distance from the central source in the two cases. The lines have

Chapter 6

Conclusions

In the last decades, an increasing interest has been devoted to the use of the Lyα line in astrophysical and cosmological contest. Lyα line has been extensively used as indicator of redshift, as a measurement of the star formation activity of galaxies and as a probe of their internal structure. Due to the resonant nature of the Lyα line propagation, a self-consistent and detailed treatment of the line radiation transfer is required in order to model properly how Lyα radiation affects the IGM, as well as to understand how different physical processes shape the spectral features of LAEs.

In my PhD project I present an analysis and the implementation of a new radiative transfer scheme which, for the first time in the literature, follows simultaneously the propagation of Lyα and ionizing radiation self-consistently. This allows to investigate the effects of evolving ionization configurations on the propagation of Lyα radiation and on the shaping of the line emerging from single objects.

In Chapter 2, I present `CRASH`α , the first radiative transfer code for cosmological application that follows the parallel propagation of Lyα and ionizing photons. `CRASH`α is a version of the continuum radiative transfer code `CRASH` with a new algorithm to follow the propagation of Lyα photons through a gas configuration whose ionization structure is evolving. The implementation introduces the time evolution for Lyα photons (a feature commonly neglected in line radiative transfer codes) and, to reduce the computational time needed to follow each scattering, adopts a statistical approach to the Lyα treatment by making extensive use of pre-compiled tables. These tables describe the physical characteristics of a photon escaping from a gas cell where it was trapped by scattering as a function of the gas temperature/density and of the incoming photon frequency. With this statistical approach I experience a drastic increase of the computational speed and, at

the same time, an excellent agreement with the full Lyα radiative transfer computations of the code MCLyα. In Chapter 3, I find that the emerging spectra keep memory of the ionization history which generates a given ionization configuration of the gas and, to properly account for this effect, a self-consistent joint evolution of line and ionizing continuum radiation as implemented in `CRASH`α is necessary. A comparison between the results from my code and from Lyα scattering alone on a fixed HI density field shows that the extent of the difference between the emerging spectra depends on the particular configuration considered, but it can be substantial and can thus affect the physical interpretation of the problem at hand. These differences should furthermore be taken into account when computing the impact of the Lyα radiation on e.g. the observability of the 21 cm line from neutral hydrogen at epochs preceeding complete reionization.

In Chapter 4, I have discussed the new features added to the code to allow for its application to general configurations, more realistic with respect to those described in the previous chapters. For this new test, I have used the outputs from the hydrodynamic simulations described in Scannapieco et al. (2008); in particular a snapshot of the galaxy at $z \simeq 10$. Thanks to the joint propagation of the line and ionizing continuum radiation, I was able to determine how the Lyα radiation emerging from each face of the box, depends on the ionization stage and on its previous evolution. The major effects of dust on the emerging spectrum are *(i)* the average suppression in intensity, and *(ii)* the reshaping of the emergent profile where flux at the external frequencies is suppressed. I found that the Lyα luminosity is dominated by photons generated from recombinations and the processed Lyα radiation emitted by the stars has just a marginal effect on the final spectrum.
I have underlined that the emergency of Lyα photons is strongly correlated to the physical state of the gas and its distribution, and given the complexity of typical galaxy surroundings, a proper modeling requires full 3D radiative transfer calculation for both the ionizing and the Lyα line radiation. In fact, the photons preferentially exit the face of the simulation box from highly ionized regions, where scattering has the least probability of happening.

The scattering of Lyα photons with atoms induce an energy exchange which provides a mechanism for raising or lowering the gas temperature from any radiation source. I present the implementation of the Lyα heating in the code the chapter 2 . This is an important issue since Lyα photons could be able to heat the IGM temperature above

the CMB temperature and render the 21 cm line visible in emission. I test this new feature analyzing the temperature variation in different physical conditions. In particular I discuss the effect of: *(i)* the gas motion, *(ii)* the Lyα luminosity of the central source, *(iii)* the gas density, *(iv)* the initial gas temperature and *(v)* the initial Lyα spectrum. I find that all these physical parameters are important to estimate the gas temperature variation caused by the scattering of Lyα photons.

Appendix A

Numerical Appendix

A.1 Tables for Lyα scattering

Following the single scatterings of each Lyα photon packet can be extremely expensive; in order to avoid it I have built tables by using a statistical approach that allows to retrieve the frequency of the outcoming photon packet, x_{out}, and the time interval for which the photon packet is trapped in the gas by the scatterings, t_{scatt}, given the frequency of the incoming photon packet, x_{in}, the gas temperature, T_{cell}, and optical depth, τ_{cell}, of the cell where the scattering takes place. I adopt the opacity at line center to characterize the optical depth of the gas in a cell. Notice that the frequencies are always meant in the comoving frame.

The tables are compiled in the following way. Given a value for the input parameters (T_{cell}, τ_{cell} and x_{in}), I run the MCLyα code several times (the results converge when 10000 Lyα photon packets are emitted) to obtain values for x_{out} and t_{scatt} which are then binned in distribution functions. The x_{out} distribution is binned using regular intervals of 0.5. For t_{scatt} I adopt equally spaced logarithmic bins of 0.014. It is important to note that the value of t_{scatt}, which depends on the distance traveled by the photon packet, is linked to the size of the cell. Thus, the tables are compiled for a reference cell size, $d_{c,ref}$, but anytime they are accessed by `CRASH`α, the value of t_{scatt} obtained needs to be linearly rescaled for the actual cell dimension, d_c. The ranges that the tables cover are:

- Temperature: $10\ \mathrm{K} \leqslant T \leqslant 10^5\ \mathrm{K}$
- Optical depth: $1 \leqslant \tau \leqslant 10^6$
- Frequency: $-100 \leqslant x \leqslant 100$

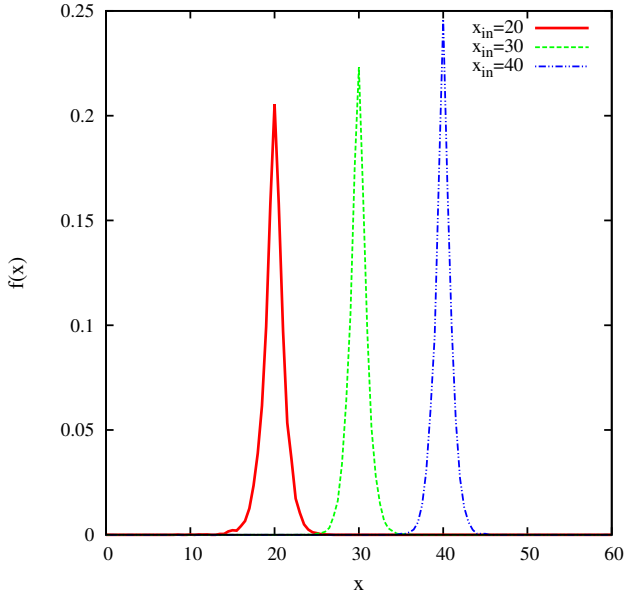

Figure A.1: Distribution of photon packets outcoming frequencies generated by multiple scatterings inside a cubic cell with $T_{cell} = 10^4$ K and $\tau_{cell} = 10^6$ for an incoming photon packet frequency of $x_{in} = 20$ (solid line), 30 (dashed line) and 40 (dashed-dotted line).

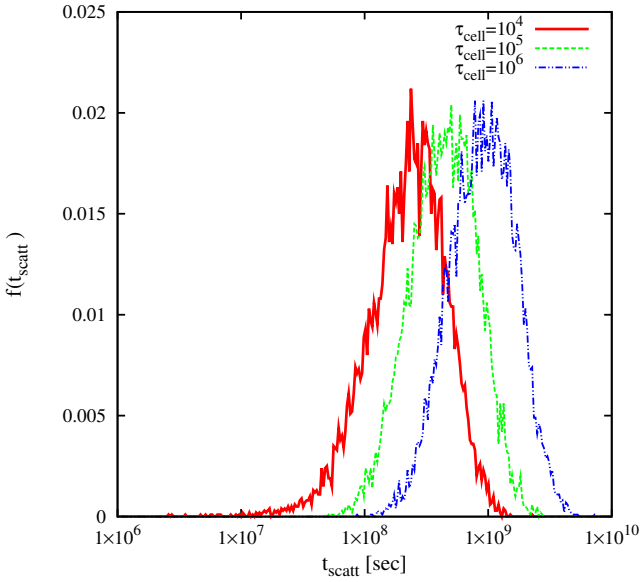

Figure A.2: Distribution of the time that a photon packet with $x_{in} = 0$ spends in a cubic cell with $T_{cell} = 10$ K and an optical depth $\tau_{cell} = 10^4$ (solid line), 10^5 (dashed line) and 10^6 (dashed-dotted line).

An example of x_{out} and t_{scatt} distributions is given in Figures A.1 and A.2. Figure A.1 shows the distribution of x_{out} for $T_{cell} = 10^4$ K, $\tau_{cell} = 10^6$ and different values of x_{in} (x_{in} =20, 30 and 40). Figure A.2 shows how the t_{scatt} distribution changes for different values of the optical depth, $\tau_{cell} = 10^4, 10^5, 10^6$; here I fixed $T_{cell} = 10$ K and $x_{in} = 0$.

The above tables are accessed by CRASHα in the following way. If T_{cell}, τ_{cell} and x_{in} are within the range covered by the tables, the distributions for t_{scatt} and x_{out} are calculated by a linear interpolation and then the value used in CRASHα for t_{scatt} and x_{out} is obtained by MC sampling the interpolated distributions. The interpolation scheme for t_{scatt} is as follows. As a first step, the values of temperature T_1 and T_2 closest to T_{cell} for which $T_1 \leqslant T_{cell} < T_2$ are found. The same is done for the optical depths τ_1 and τ_2, and the frequencies x_1 and x_2. The weights to be assigned to each value are derived by linear interpolation. As an example I can consider a simple 1D case, with linear interpolation only on temperatures. In this case, $t_{scatt} = w_{T_1} t_{scatt}(T_1) + w_{T_2} t_{scatt}(T_2)$, where the weights are $w_{T_1} = (T_2 - T_{cell})/\Delta T$ and $w_{T_2} = (T_{cell} - T_1)/\Delta T$, with $\Delta T = T_2 - T_1$. The same procedure, extrapolated in 3D, produces a distribution of t_{scatt} that will be randomly sampled in CRASHα . The interpolation for x_{out} follows the same steps, after a shift in the frequency space has been performed to assure that the correct distribution is obtained and no spurious peak forms. To understand how the x_{out} interpolation works an easy example can be useful. Let us assume that the purpose is to reproduce the dashed profile centered in $x = 30$ (Fig. A.1) starting from the two profiles at $x = 20$ and 40. If the interpolation were performed bin by bin without any previous shift (e.g. the bin [19.5-20[of the solid curve with the bin [39.5-40[of the dashed-dotted curve, and similarly for all the bins), the result would be two smaller peaks centered at $x = 20$ and 40, rather than one centered at $x = 30$. To perform a correct interpolation I need to center the solid and dashed-dotted profiles on $x = 30$ and then interpolate.

To check the validity of my approach, I have compared the results from the full radiative transfer treatment (using MCLyα) with a case in which the tables were used. In Figure A.3 the distribution in frequency of 10000 Lyα photon packets escaping from a gas with temperature $T = 8000$ K, optical depth $\tau = 10^6$ and frequency $x = 0$ is shown. The dotted (solid) line in the upper panel indicates the results for the approximate (full radiative transfer) treatment using tables built with 10000 photon packets. In the bottom panel the difference between the two distributions is plotted, showing an excellent agreement,

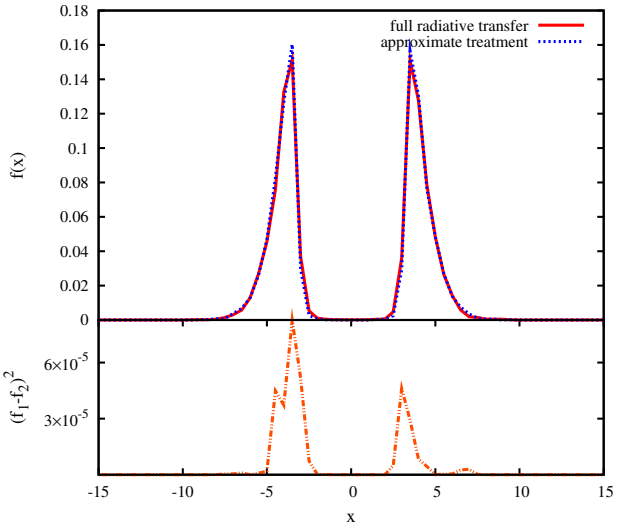

Figure A.3: The upper panel shows the predicted Lyα frequency distribution for monochromatic line radiation escaping from a gas with temperature $T = 8000$ K and optical depth $\tau = 10^6$. The dotted (solid) line indicates the results for the approximate (full radiative transfer) treatment using tables build with 10000 photon packets. The difference between the two distributions is shown in the bottom panel.

which is found also for different initial conditions. I perform the same check with a more complex gas distribution using the expanding shell described in Section 3.3. As the final spectrum is expected to have a wider frequency distribution, this test is performed to check the accuracy of the x_{out} interpolation at larger frequency shifts. The results are shown in Figure A.4; for both profiles I have used 400000 photon packets. Also in this case an excellent agreement is found.

I perform a final test in which I follow the evolution of an ionization field, tracing each Lyα scattering and then I compare the results with the `CRASH`α approach. The initial conditions are the same described in Section 3.1 but with a lower gas density, $n_{\rm H} = 0.01$ cm^{-3}, to ensure that the former computation is not prohibitively expensive. Figure A.5 shows the spectra of escaped photon packets when the averaged ionization degree is $\sim 50\%$. Since the profiles are very similar, I conclude that my approach is able to reproduce with a high accuracy both the frequency distribution and the time evolution of Lyα photon packets. In addition, the use of the tables allows an enormous gain in computational speed.

As the changes in the gas properties during a simulation can be drastic, sometimes the values τ_{cell} and x_{in} can fall outside the range covered by the tables (I do not expect

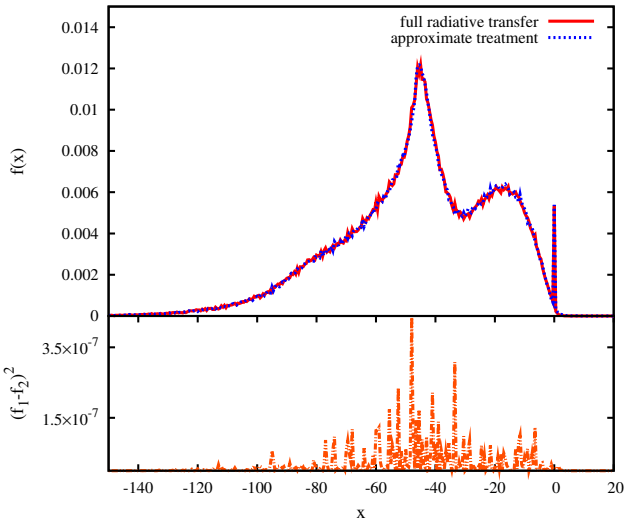

Figure A.4: As Fig. A.3 but for a gas configuration resembling a shell with temperature $T = 10^4$ K and column density $N_{\rm HI} = 2 \times 10^{20}$ cm^{-2} expanding with an uniform radial velocity $V = 300$ km s^{-1}. The dotted (solid) line in the upper panel indicate the results for the approximate (full radiative transfer) treatment using tables build with 400000 photon packets. The difference between the two distributions is shown in the bottom panel.

T_{cell} to fall outside the range). In these cases I perform an extrapolation of the existing tables. More in particular, for $\|x_{in}\| > 100$ I use the same distributions derived for $\|x_{in}\| = 100$. This is a good approximation as at these frequencies the cross section is small and Lyα scattering rare. The extrapolation for the optical depth works differently. If $\tau_{cell} < 1$ no interaction takes place and the photon packet propagates freely. If $\tau_{cell} > 10^6$ I divide the cell into 2^{3n} sub-cells (where n is the number of divisions performed) until each sub-cell has an optical depth $< 10^6$. At this point, every sub-cell is treated as a single cell.

It is worthwhile noticing that using two separate extractions for x_{out} and t_{scatt}, imply that the frequency and time distribution are independent. This is not always true. Since in most cases of interest the approximation introduced induces only a very weak effect on the results, I typically assume that this correlation can be neglected. Nevertheless, as `CRASH`α is designed to work under conditions as general as possible, I have also implemented the possibility to use correlated 2D tables, that perform a single extraction of x_{out} and t_{scatt}. I repeat the last test using both approaches and I show the results in Figure A.6. It is clear that the correlation has indeed a minor effect.

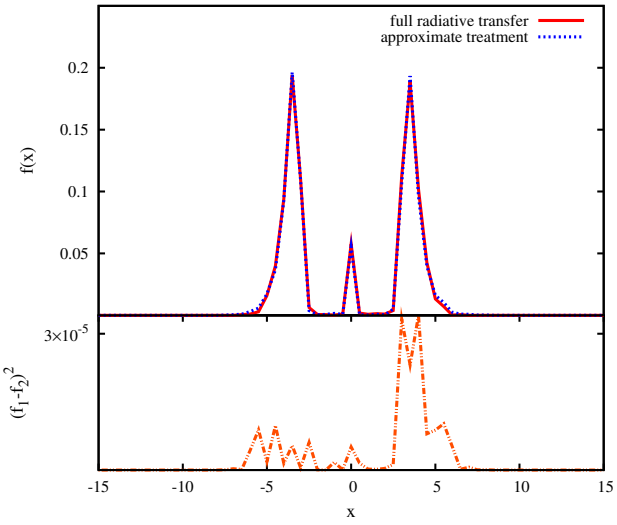

Figure A.5: Comparison of Lyα spectra obtained with a full Lyα treatment, following each scattering, and with `CRASH`α approach. The profiles refer to a static sphere with temperature $T = 10000$ K, gas density $n_{\rm H} = 0.01$ cm^{-3} and radius $r_{sph} = 15$ pc, when the averaged ionization degree is about 50%. The difference between the two distributions is shown in the bottom panel.

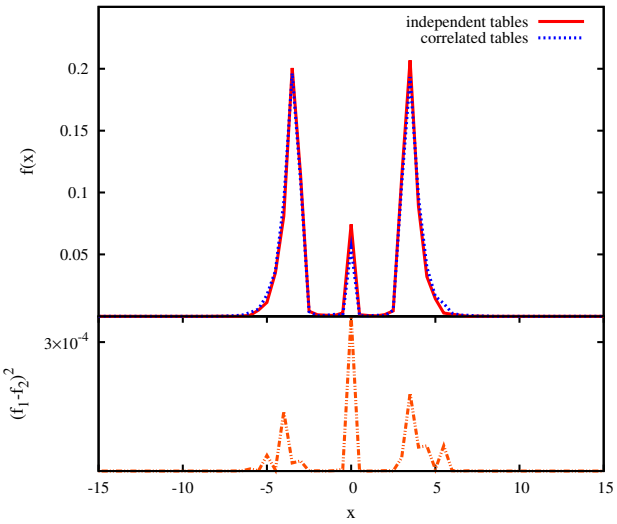

Figure A.6: Comparison of Lyα spectra obtained extracting x_{out} and t_{scatt} using uncorrelated 1D tables, or correlated 2D ones. The profiles refer to a static sphere with temperature $T = 10000$ K, gas density $n_{\rm H} = 0.01$ cm^{-3} and radius $r_{sph} = 15$ pc, when the averaged ionization degree is about 50%. The difference between the two distributions is shown in the bottom panel.

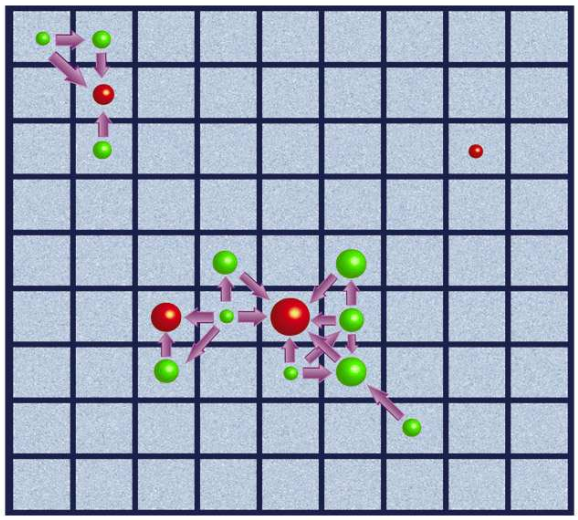

Figure A.7: Illustration of the clustering algorithm. The Figure shows how the tree looks like after it is built by the code. Sources in red (green) are (are not) local maxima. Larger sizes indicate larger luminosities. See text for details.

A.2 Sources distribution

The presence of a large number of sources with different luminosity (in the case presented here I have $\sim$ 3000 sources spanning a range of $\sim 2 \cdot 10^5 - 2 \cdot 10^8 M_\odot$) can sensitively decrease the code's speed. The code in fact becomes inefficient when most of the total luminosity is released by a minority of sources, but the same resolution is still applied to all the sources. In this case the code spends a lot of time computing a small effect on the gas due to the faintest sources. In the following, I describe the method adopted to alleviate this problem, based on the resampling of the luminosity field and the redistribution of the emissivity to local maxima. With this approach I expect a drastic reduction of the sources' number with a small effect on the gas conditions.

A.2.1 Algorithm

To redistribute the luminosity I identify local maxima and which maxima each source should be assigned to. To this aim, a tree of sources is built before the simulation starts, in which the relation between each source and all its neighbours is defined. The algorithm is described in the following steps:

1. Sorting the sources: the sources are sorted according to their luminosity.

2. Building the tree: starting from the faintest source, the code checks if more luminous sources are present in contiguous cells. In this case the code stores a link to those sources. The same procedure is applied to the second least luminous source and then for all the sources up to the most luminous one, until the full tree is built and the code can follow a path from each source to its local maximum. Following this procedure, the number of sources is reduced by keeping only the local maxima. A graphic rappresentation of the tree is given in Figure A.7.

3. Distributing the luminosity: the luminosity of the faintest source is now redistributed in equal amounts between all the neighbouring sources identified by the links stored in the previous step. This routine is repeated for all the sources following the pre-sorted order of luminosity.

4. Reducing the number of sources: once the luminosity field has been redistributed among its local maxima, the sources which are not local maxima (i.e. those that do not have any link to more luminous sources) are deleted from the list. At the end of this algorithm we are left with a new array of sources (the previous local maxima), which preserves the global luminosity.

An effect similar to redistributing the luminosity to local maxima can be obtained cutting all the sources below a given threshold. The differences with this approach are: *(i)* the small isolated sources would be neglected (these are the typical sources which can arise in peripheral regions with low density) and *(ii)* a lot of the sources would be placed in neighbouring cells in high density regions without improving significantly the quality of luminosity sampling; in fact as I will show in the next section the effects of luminosity redistribution are minimal.

A.2.2 Tests

The main consequences expected from the clustering of the sources described above are *(i)* a reduction of N_p (if the number of photon packets emitted per source is kept constant, the total number of packets is smaller because after clustering I have fewer sources) and *(ii)* the same amount of energy after clustering is emitted by a single source at a given location rather than being distributed among nearby sources. While the first effect results only in a reduction of resolution, which, if needed, can be balanced by an increase in the number

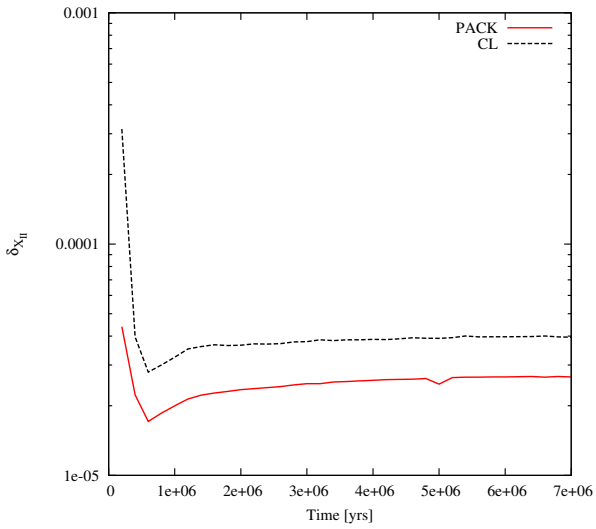

Figure A.8: Evolution of the median value of the ionization fraction's variation, $\delta_{\chi_{\rm HII}}$, for CL (dashed line) and PACK (solid) simulations. See text for details.

of packets emitted by each source, the second could affect the results of the simulation since it concentrates artificially all the luminosity in a single location.

To test the above effects I ran three simulations with continuum radiation only. I use the same physical conditions described in Section 4.1 but I choose to use only the 300 more luminous sources in order to obtain faster results. I have verified that this choice does not impact the final outcome of the tests and can be understood because the most luminous sources are more clustered and thus the procedure described above has a higher impact on these sources rather than on the isolated, smaller ones. In the reference simulation (REF) I use 10^7 packets per source and no source clustering is applied. In the second simulation (CL) I use the same amount of packets per source, but I apply the source clustering. The resulting number of sources is 54. Finally, I compare the two simulations with a third one (PACK) in which there is no source clustering, but the number of packets emitted per source is decreased in order to have the same total packets emitted by the CL simulation, $N_p = 1.8 \cdot 10^6$. This case is useful to understand the effect of decreasing N_p without modifying the distribution of the sources.

To compare the results from the different simulations, I define the variation of ionization fraction in each cell as:

$$\delta_{\chi_{\rm HII}} = \frac{|\chi_{\rm HII,REF} - \chi_{\rm HII,TEST}|}{\chi_{\rm HII,REF}}, \tag{A.1}$$

where $\chi_{\rm HII}$ is the ionization fraction of each cell at each snapshot and TEST=CL, PACK. I

use the median value of this quantity to characterize the differences between the reference simulation and the other two test cases. The evolution of such value is shown in Figure A.8 for the CL (dashed line) and PACK (solid) case. In both cases the value of the variation is extremely small and the ionization fraction is then statistically well reproduced. At the beginning of the simulations though, I observe a larger discrepancy due to the low statistics. In fact, as the simulation proceeds and a larger number of cells is affected by the radiation, the sample of cells used for the determination of the median value gets more representative. In the PACK case, which simulates a loss in resolution due to a lower number of N_p, the variation is due to a worse sampling of the luminosity field and lies in the range $2 - 3 \cdot 10^{-5}$. The CL case shows a variation between $3 - 4 \cdot 10^{-5}$ and in this case the discrepancy is due to both the smaller value of N_p and the redistribution of the sources location. In summary, I can say that *(i)* the major discrepancy is introduced by a decrease in the number of emitted photon packets, but overall *(ii)* the sum of the two effects is statistically negligible. In this respect, the best way to proceed is to allow for source clustering and choose a value of N_p which guarantees a satisfactory level of resolution.

In Figure A.9 I show four panels that describe the gas properties projected over the z axis of the simulation box. In the top-left panel I plot the initial number density of the neutral gas. After $5{\cdot}10^6$ yrs the neutral gas is shaped by the interaction with the radiation, as can be seen in the top-right panel, where the projected distribution for the reference case is shown. As expected, the ionizing photons have propagated preferentially along trajectories with low density gas, while they are blocked by the high density filaments.

To underline the differences between the test cases and REF, I also plot the iso-contours of the differences at the same time between the neutral gas number density distribution in PACK and REF (bottom-left panel) and in CL and REF (bottom-right panel). In both cases the structure of the iso-contours is very similar, suggesting that there are no major differences in the morphology of the neutral gas distribution and, in particular, that the clustering procedure adopted in the CL simulation does not yield any systematic variation in the neutral fraction. The differences on the small scales are generated by different emission conditions in the simulations, but since the discrepancy value is small they are negligible for my purposes.

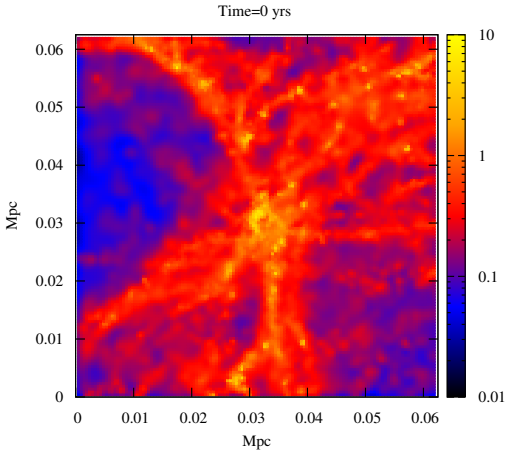
Time=0 yrs
Mpc
Mpc
0
0.01
0.02
0.03
0.04
0.05
0.06
10
1
0.1
0.01

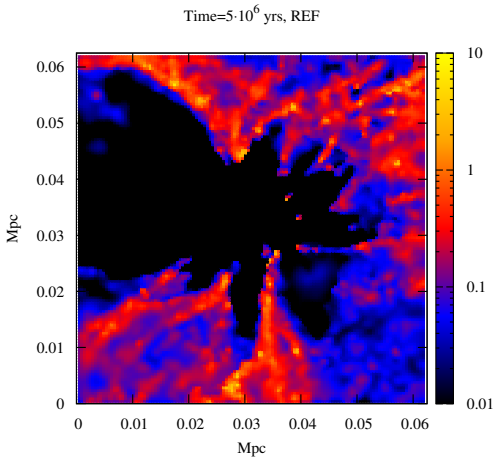
Time=5·10^6 yrs, REF
Mpc
Mpc
0
0.01
0.02
0.03
0.04
0.05
0.06
10
1
0.1
0.01

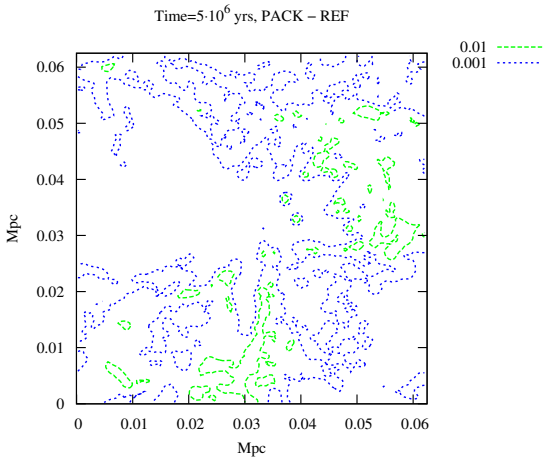
Time=5·10^6 yrs, PACK – REF
Mpc
Mpc
0
0.01
0.02
0.03
0.04
0.05
0.06
0.01
0.001

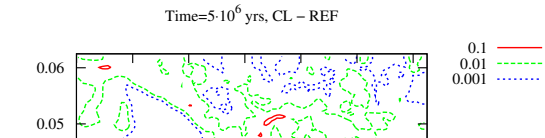
Time=5·10^6 yrs, CL – REF
0.06
0.05
0.1
0.01
0.001

Bibliography

[] Adams, T. F., 1972, ApJ, 174, 439

[] Ahn, S.H., 2004, ApJ, 601, L25

[] Ahn, S.H., Lee, H.W., Lee, H.M., 2000, JKAS, 33, 29

[] Ahn, S.H., Lee, H.W., Lee, H.M., 2001, ApJ, 554, 604

[] Allison, A. C., & Dalgarno, A. 1969, ApJ, 158, 423

[] Avery, L. W. & House, L. L., 1968, ApJ, 152, 493

[] Barkana, R. & Loeb, A., 2005, ApJ, 626, 1

[] Barkana, R., & Loeb, A. 2005, ApJ, 624, L65

[] Bunker, A.J., et al., 2003, MNRAS, 342, L47

[] Bunker, A. J., Stanway, E. R., Ellis, R. S., & McMahon, R. G. 2004, MNRAS, 355, 374

[] Cantalupo, S., et al., 2005, ApJ, 628, 61

[] Charlot, S., & Fall, S. M. 1993, ApJ, 415, 580

[] Chary, R.-R., Stern, D., & Eisenhardt, P. 2005, ApJ, 635, L5

[] Chen, X. & Miralda-Escudé, J., 2006, astro-ph/0605439

[] Chen, X., & Miralda-Escudé, J. 2004, ApJ, 602, 1

[] Chuzhoy, L. & Zheng, Z. 2007, astro-ph/0706.0895

[] Chuzhoy, L., & Shapiro, P. R. 2007, ApJ, 655, 843

[] Ciardi, B. & Madau P. 2003, ApJ, 596, 1

[] Ciardi, B. & Salvaterra, R., 2007, MNRAS, 381, 1137

[] Ciardi, B., & Salvaterra, R. 2007, MNRAS, 381, 1137

[] Ciardi, B., et al., 2001, MNRAS, 324, 381

[] Dawson, S., Rhoads, J. E., Malhotra, S., Stern, D., Wang, J., Dey, A., Spinrad, H., & Jannuzi, B. T. 2007, ApJ, 671, 1227

[] Dawson, S., Spinrad, H., Stern, D., Dey, A., van Breugel, W., de Vries, W., & Reuland, M. 2002, ApJ, 570, 92

[] Dawson, S., et al., 2007, astro-ph7/0707.4182

[] Dijkstra, M., Haiman, Z. & Spaans, M., 2006, ApJ, 649, 14

[] Djorgovski, S., & Thompson, D. J. 1992, The Stellar Populations of Galaxies, 149, 337

[] Djorgovski, S. G., Castro, S., Stern, D., & Mahabal, A. A. 2001, ApJ, 560, L5

[] Fan, X., Strauss, M. A., Becker, R. H.; White, R. L., Gunn,J. E., Knapp, G. R., Richards, G. T., Schneider, D. P., Brinkmann, J. & Fukugita, M., 2006, ApJ, 132, 117

[] Field, G.B., 1958, Proc. I.R.E., 46, 240

[] Field, G.B., 1959, ApJ, 129, 536

[] Field, G. B. 1959, ApJ, 129, 551

[] Finkelstein, S. L., Rhoads, J. E., Malhotra, S., Pirzkal, N., & Wang, J. 2007, ApJ, 660, 1023

[] Finkelstein, S. L. 2008, Ph.D. Thesis,

[] Gawiser, E., et al. 2006, ApJ, 642, L13

[] Gawiser, E., et al. 2006, ApJ, 642, L13

[] Gawiser, E., et al. 2007, ApJ, 671, 278

[] Giavalisco, M., Steidel, C. C., Adelberger, K. L., Dickinson, M. E., Pettini, M., & Kellogg, M. 1998, ApJ, 503, 543

[] Giavalisco, M. 2002, ARA&A, 40, 579

[] Gould, A. & Weinberg, D. H., 1996, ApJ, 468, 462

[] Gronwall, C., et al. 2007, ApJ, 667, 79

[] Gunn, J.E., & Peterson, B. A. 1965, ApJ, 142, 1633

[] Hansen, M., Oh, S.P., 2006, MNRAS, 367, 979

[] Harrington, J.P., 1973, MNRAS, 162,43

[] Hartmann, L. W., Huchra, J. P., Geller, M. J., O'Brien, P., & Wilson, R. 1988, ApJ, 326, 101

[] Hou, J. L., Boissier, S., & Prantzos, N. 2001, A&A, 370, 23

[] Hu, E., et al., 1998, ApJ, 502, L99

[] Hu, E., et al., 2002, ApJ, 568, 75

[] Hu, E., et al., 2004, AJ, 127, 3137

[] Hu, E. M., Cowie, L. L.,McMahon, R. G., Capak, P., Iwamuro, F., Kneib, J.-P., Maihara, T., & Motohara, K. 2002, ApJ, 568, L75

[] Hu, E. M., Songaila, A., Cowie, L. L., & Stockton, A. 1991, ApJ, 368, 28

[] Hu, E. M., & Cowie, L. L. 1987, ApJ, 317, L7

[] Huege, T., & Falcke, H. 2004, The Role of VLBI in Astrophysics, Astrometry and Geodesy, 13

[] Iye, M., et al., 2006, Nature, 443, 186

[] Kaplinghat, M., Chu, M., Haiman, Z., Holder, G. P., Knox, L., & Skordis, C. 2003, ApJ, 583, 24

[] Kashikawa, M., et al., 2006, ApJ, 648, 7

[] Katz, N., Weinberg, D. H.Hernquist, L., & Miralda-Escude, J. 1996, ApJ, 457, L57

[] Kobayashi, M. A. R., Kamara, H. 2004, ApJ, 600, 564

[] Kodaira, K., et al., 2003, PASJ, 55, 17

[] Kovač, K., Somerville, R. S., Rhoads, J. E., Malhotra, S., & Wang, J. 2007, ApJ, 668, 15

[] Kuhlen, M., Madau, P., & Montgomery, R. 2006, ApJ, 637, L1

[] Kunth, D., Mas-Hesse, J. M., Terlevich, E., Terlevich, R., Lequeux, J., & Fall, S. M. 1998, A&A, 334, 11

[] Kunth, D., et al., 1994, A&A, 282, 709

[] Lai, K., Huang, J.-S., Fazio, G., Cowie, L. L., Hu, E. M., & Kakazu, Y. 2007, Deepest Astronomical Surveys, 380, 83

[] Lai, K., et al. 2008, ApJ, 674, 70

[] Liszt, H. 2001, A&A, 371, 698

[] Loeb, A., Rybicki, G.B., 1999, ApJ, 524, 527

[] Madau, P., Ferguson, H. C., Dickinson, M. E., Giavalisco, M., Steidel, C. C., & Fruchter, A. 1996, MNRAS, 283, 1388

[] Madau, P., Meiksin, A., & Rees, M. J. 1997, ApJ, 475, 429

[] Mas-Hesse, J. M., Kunth, D., Tenorio-Tagle, G., Leitherer, C., Terlevich, R. J., & Terlevich, E. 2003, ApJ, 598, 858

[] Maselli, A. & Ferrara A., 2005, MNRAS, 364, 1429

[] Maselli, A., Ciardi B., & Kanekar, A., 2008, in preparation

[] Maselli, A., Ferrara, A. & Ciardi, B., 2003, MNRAS, 345, 379

[] McCarthy, P. J. 1993, ARA&A, 31, 639

[] Meier, D. L., & Terlevich, R. 1981, ApJ, 246, L109

[] Meier, D. L. 1976, ApJ, 207, 343

[] Murayama, T., et al., 2007, ApJS, 172, 523

[] Nagamine, K., Springel, V., & Hernquist, L. 2004, MNRAS, 348, 435

[] Neufeld, D.A., 1990, ApJ, 350, 216

[] Neufeld, D. A. 1990, ApJ, 350, 216

[] Nilsson, K. K., et al. 2007, A&A, 471, 71

[] Osterbrock, D. E., 1962, ApJ, 135, 195

[] Ouchi, M., & SXDS 2007, Bulletin of the American Astronomical Society, 38, 226

[] Ouchi, M., et al. 2004,ApJ, 611, 660

[] Ouchi, M., et al. 2004,ApJ, 611, 685

[] Ouchi, M., et al. 2008, ApJS, 176, 301

[] Ouchi, M., et al. 2008, ApJS, 176, 301

[] Papovich, C., Dickinson, M., & Ferguson, H. C. 2001, ApJ, 559, 620

[] Partridge, R. B., Peebles, J. E. 1967, ApJ, 147, 868

[] Partridge, R. B., & Peebles, P. J. E. 1967, ApJ, 148, 377

[] Peebles, P. J. E. 1968, ApJ, 153, 1

[] Pei, Y. C., Fall, S. M., & Hauser, M. G. 1999, ApJ, 522, 604

[] Pelló, R., et al., 2006, RMxAC, 29, 132

[] Pettini, M., Shapley, A. E., Steidel, C. C., Cuby, J.-G., Dickinson, M., Moorwood, A. F. M., Adelberger, K. L., & Giavalisco, M. 2001, ApJ, 554, 981

[] Pettini, M., Smith, L. J., Hunstead, R. W., & King, D. L. 1994, ApJ, 426, 79

[] Pettini, M., & Pagel, B. E. J. 2004, MNRAS, 348, L59

[] Pirzkal, N., Malhotra, S., Rhoads, J. E., & Xu, C. 2006, Bulletin of the American Astronomical Society, 38, 1145

[] Pirzkal, N., Malhotra, S., Rhoads, J. E., & Xu, C. 2007, ApJ, 667, 49

[] Prochaska, J. X., Gawiser, E., Wolfe, A. M., Castro, S., & Djorgovski, S. G. 2003, ApJ, 595, L9

[] Péroux, C., Dessauges-Zavadsky, M., D'Odorico, S., Kim, T.-S., & McMahon, R. G. 2003, MNRAS, 345, 480

[] Reddy, N. A., Steidel, C. C., Pettini, M., Adelberger, K. L., Shapley, A. E., Erb, D. K., & Dickinson, M. 2008, ApJS, 175, 48

[] Rhoads, J. E. & Malhotra, S., 2001, ApJ, 563, 5

[] Rhoads, J. E., et al., 2003, AJ, 125, 1006

[] Schaerer, D., & Pelló, R. 2005, MNRAS, 362, 1054

[] Schmidt, M. 1965, ApJ, 141, 1295

[] Scott, D., & Rees, M. J. 1990, MNRAS, 247, 510

[] Semelin, B., Combes, F. & Baek, S., 2007, A&A, 474, 365

[] Shapley, A. E., Steidel, C. C., Adelberger, K. L., Dickinson, M., Giavalisco, M., & Pettini, M. 2001, ApJ, 562, 95

[] Shapley, A. E., Steidel, C. C., Pettini, M., & Adelberger, K. L. 2003, ApJ, 588, 65

[] Smith, F. J. 1966, P&SS, 14, 929

[] Stanway, E. R., Bunker, A. J., McMahon, R. G., Ellis, R. S., Treu, T., & McCarthy, P. J. 2004, ApJ, 607, 704

[] Stark, D. P., et al., 2007, ApJ, 663, 10

[] Steidel, C. C., Adelberger, K. L., Dickinson, M., Giavalisco, M., Pettini, M., & Kellogg, M. 1998, ApJ, 492, 428

[] Steidel, C. C., Adelberger, K. L., Giavalisco, M., Dickinson, M., & Pettini, M. 1999, ApJ, 519, 1

[] Steidel, C. C., Adelberger, K. L., Shapley, A. E., Pettini, M., Dickinson, M., & Giavalisco, M. 2000, ApJ, 532, 170

[] Steidel, C. C., Adelberger, K. L., Shapley, A. E., Pettini, M., Dickinson, M., & Giavalisco, M. 2003, ApJ, 592, 728

[] Steidel, C. C., Giavalisco, M., Dickinson, M., & Adelberger, K. L. 1996, AJ, 112, 352

[] Steidel, C. C., Giavalisco, M., Pettini, M., Dickinson, M., & Adelberger, K. L. 1996, ApJ, 462, L17

[] Stern, D., et al., 2005, ApJ, 619, 12

[] Taniguchi, Y., et al., 2005, PASJ, 57, 165

[] Tasitsiomi, A., 2006, ApJ, 645, 792

[] Tenorio-Tagle, G., Silich, S. A., Kunth, D., Terlevich, E., & Terlevich, R. 1999, MNRAS, 309, 332

[] Tinsley, B. M. 1972, A&A, 20, 383

[] Valls-Gabaud, D. 1993, ApJ, 419, 7

[] Venemans, B. P., McMahon, R. G., Parry, I. R., King, D. J., Bland-Hawthorn, J., & Horton, A. J. 2009, Science with the VLT in the ELT Era, 187

[] Venemans, B. P., et al. 2005, A&A, 431, 793

[] Verhamme, A., Schaerer, D. & Maselli A., 2006, A&A, 460, 397 (VSM06)

[] Verma, A., Lehnert, M. D., Förster Schreiber, N. M., Bremer, M. N., & Douglas, L. 2007, MNRAS, 377, 1024

[] Villar-Martín, M., Tadhunter, C., Morganti, R., & Holt, J. 2005, MNRAS, 359, L5

[] Wadadekar, Y., Casertano, S., & de Mello, D. 2006, AJ, 132, 1023

[] Wolfe, A. M., Turnshek, D. A., Smith, H. E., & Cohen, R. D. 1986, ApJS, 61, 249

[] Wouthuysen, S. A., 1952, AJ, 57, 31

[] Wouthuysen, S. A. 1952, AJ, 57, 31

[] Zygelman, B. 2005, ApJ, 622, 1356